Universität Hamburg
Department Physik

Femtosecond Resolved Diagnostics for Electron Beam and XUV Seed Temporal Overlap at sFLASH

Dissertation

zur Erlangung des Doktorgrades
des Fachbereichs Physik
der Universität Hamburg

vorgelegt von

Roxana Tarkeshian
aus Tehran

Hamburg
2012

Gutachter der Dissertation	Prof. Dr. Jörg Rossbach Prof. Dr. Markus Drescher
Gutachter der Disputation	Prof. Dr. Jörg Rossbach Prof. Dr. Eckhard Elsen
Datum der Disputation	24.02.2012
Vorsitzender des Prüfungsausschusses	Dr. Georg Steinbrück
Vorsitzender des Promotionsausschusses	Prof. Dr. Peter Hauschildt
Leiterin des Fakultät Physik:	Prof. Dr. Daniela Pfannkuche
Dekan der MIN-Fakultät:	Prof. Dr. Heinrich Graener

Abstract

sFLASH is a seeded experiment at the Free-Electron Laser FLASH in Hamburg. It uses a 38 nm High-Harmonic-Generation (HHG) scheme to seed the FEL-process in a 10 m long variable-gap undulator. The temporal overlap between the electron and HHG pulses is critical to the seeding process. The use of a 3^{rd} harmonic accelerating module provides a high current electron beam with $\sim (400\,\mathrm{fs})_{\mathrm{FWHM}}$ bunch duration. The duration of the HHG laser pulse is $\leq (30\,\mathrm{fs})_{\mathrm{FWHM}}$. The desired overlap is achieved in two steps. Firstly, the HHG drive laser is brought to temporal overlap with the incoherent spontaneous radiation from an upstream undulator with picosecond resolution. The temporal overlap is periodically monitored using a streak camera installed in the linear accelerator tunnel. Next, the coherent radiation from an undulator is used to determine the exact overlap of the electron beam in a modulator-radiator set-up with sub-picosecond resolution. The physical and technical principles of the setup providing the temporal overlap are described. Results of the system are analyzed. An analytical approach and simulation results for the performance of the seeding experiment are presented. First attempts at demonstration of seeding are discussed. Strategies for optimizing overlap conditions are presented.

Zusammenfassung

sFLASH ist ein Experiment, dass den Freie-Elektronen Laser FLASH in Hamburg seedet. Um den FEL-Prozess bei 38 nm zu seeden, nutzt es ein Schema zur Erzeugung hoher Harmonischer (HHG). Der zeitliche Überlapp zwischen dem Elektronenpaket und dem XUV-Puls ist hierbei kritisch. Die Verwendung eines 3. Harmonischen Beschleunigungsmoduls ermöglicht die Erzeugung eines gaußförmigen -Elektronenpakets mit $\sim (400\,\mathrm{fs})_{\mathrm{FWHM}}$. Die Dauer des Seed-Pulses ist $\leq (30\,\mathrm{fs})_{\mathrm{FWHM}}$. Der erwünschte zeitliche Ueberlapp wird in zwei Schritten erreicht. Zunächst wird der optische Laser mit der inkohärenten, spontanen Undulatorstrahlung zeitlich mit Pikosekunden Genauigkeit überlappt. Der zeitliche Überlapp wird dabei in regelmäßigen Zeitabständen gemessen. Dafür wird eine Streakkamera eingesetzt, die im Beschleunigertunnel installiert ist. Dann wird die kohärente Undulatorstrahlung verwendet, um den exakten zeitlichen Überlapp mit Femtosekunden Genauigkeit zu bestimmen. Die physikalischen und technischen Prinzipien des Aufbaus zur Findung des zeitlichen Überlapps werden im Detail beschrieben und die Ergebnisse analysiert. Ein analytischer Ansatz und Simulationsergebnisse zum Seedingexperiment werden vorgestellt. Erste Versuche zur Demonstration des Seedings werden diskutiert. Strategien zur Optimierung des zeitlichen Überlapps werden vorgestellt.

Contents

1 Introduction 1

1.1 Schemes to improve the longitudinal coherence . . . 4

1.1.1 High Harmonic Generation (HHG) . . . 4

1.1.2 High-Gain Harmonic Generation (HGHG) . . . 4

1.1.3 Echo-Enabled Harmonic Generation (EEHG) . . . 5

1.1.4 Super-radiant Cascade Seeding (SCS) . . . 5

1.2 Examples of seeded FEL facilities . . . 6

1.3 Layout of this thesis . . . 7

2 FEL principle and theoretical approach on the relativistic electron and light interaction 9

2.1 Light-electron interaction in FELs . . . 9

2.2 Seeding process in FEL . . . 16

2.3 Optical klystron concept as a tool for generation of coherent radiation . . . 17

2.4 Theory of the High-order Harmonic Generation (HHG) . . . 19

2.4.1 Phase matching . . . 20

3 Longitudinal electron beam diagnostics at FLASH 23

3.1 Optical Replica Synthesizer (ORS) . . . 24

3.2 Transverse Deflecting Structure (TDS) . . . 25

3.3 Terahertz and Optical SYnchrotron radiation LABoratory (TOSYLAB) . . . 26

3.4 Electro Optical Sampling (EOS) . . . 26

3.5 Synchronization system . . . 26

4 Experimental layout of XUV FLASH seeding experiment 31
4.1 Seed drive laser . . . 32
4.1.1 Synchronization with master oscillator . . . 34
4.2 HHG source Characterization . . . 34
4.3 Transport beamline . . . 37
4.4 Undulator section and photon beamline . . . 39
4.5 Six-dimensional overlap of phase-space distribution . . . 41
4.5.1 Transverse overlap . . . 41
4.5.2 Spectral overlap . . . 42
4.5.3 Longitudinal overlap . . . 44
5 Theoretical investigation on the longitudinal overlap between electron beam and seeding pulse 47
5.1 Tolerance studies on the longitudinal jitter using GENESIS . . . 47
5.1.1 Simulation result using measured electron bunch distribution . . . 48
5.1.2 Simulation results using an electron bunch taken from start-to-end simulation . . . 52
5.2 Statistical analysis of the jitter effects . . . 54
5.2.1 Analytical approach . . . 54
5.2.2 Numerical simulation . . . 57
6 Proposed methods for temporal overlap measurement 61
6.1 Measurement with picosecond resolution . . . 61
6.1.1 Photomultiplier tube . . . 62
6.1.2 Streak-camera based measurement . . . 62
6.2 Measurement with femtosecond resolution using MOR setup. . . . 66
6.2.1 Experimental methodology . . . 68
6.2.2 Simulation results using PERSEO . . . 73
7 Beamline and shielding for the longitudinal overlap measurement 77
7.1 Description of the setup . . . 77
7.2 Shielding for the electronic components . . . 81

7.2.1 Radiation measurement in the FLASH tunnel 82

8 Optimization of the beamline 89

8.1 Intensity threshold for the streak camera 89

8.2 Transmission of the transport beamline 92

8.3 Beam intensity control using combinations of spectral filters 96

8.4 Dispersion of the longitudinal overlap beam line. 99

8.5 Effect of the path difference in arrival time 99

9 Measurement results 101

9.1 Coarse longitudinal overlap measurement 101

9.2 Femtosecond resolved temporal overlap using coherent radiation 106

9.3 Attempts for seeding at 38 nm 108

9.4 Offline data analysis 109

10 Conclusion and Outlook 111

A Convolution of two Gaussian distributions 117

B Optimization of the dispersion strength 119

C Possibility of even harmonic coupling in the existing setup 121

D Transmission of the seeding beamline for the NIR laser beam 123

E Neutron and gamma dosimetry 125

F Transient time of the optical wavelengths through different materials 127

Bibliography 136

List of Figures

1.1 Peak brilliance of FLASH in comparison to XFEL and 3rd generation synchrotron radiation sources. 2

1.2 The typical SASE spectrum, taken from a GENESIS simulation. 3

1.3 HGHG scheme. 5

1.4 EEHG scheme. 6

2.1 The electron trajectory and light wave in an undulator 9

2.2 The exponential growth of the FEL pulse energy 12

2.3 SASE characteristics along the undulator 14

2.4 Measured probability distribution of FLASH 15

2.5 Seeding undulator by an external light source 16

2.6 Principle of operation of the optical Klystron. 17

2.7 Schematic of the HHG process 20

2.8 Phase mismatch 21

3.1 The Free-electron laser in Hamburg (FLASH). 23

3.2 The FLASH pulse temporal structure with 10 Hz repetition rate 27

3.3 The laser based synchronization system installed in FLASH 28

3.4 The Arrival time jitter of the electron bunches as determined by the BAM 28

4.1 Schematic layout of the sFLASH section. 32

4.2 Seed drive laser layout. 33

4.3 Synchronization layout of the NIR laser oscillator with MO 35

4.4 HHG setup used for sFLASH. 36

4.5 Spectrum of higher-order harmonics generated in Ar gas by two different NIR focusing mirrors. 37

4.6 HHG transport beamline 38

4.7 Schematic of the extraction beamline 40

4.8 Measured several single shot SASE-FEL spectra 43

4.9 The bandwidth of HHG radiation spectrum detected at the spectrometer after the seeding undulators. 44

5.1 Measured electron bunch distribution 48

5.2 Measured energy spread and mean deviation of the electron bunch 49

5.3 Total power of the seeded radiation pulse as a function of seeding pulse injection time. 50

5.4 The simulated spectrum of seeded pulse for the measured electron bunch distribution. 50

5.5 The contrast of seeded pulse and SASE background 51

5.6 The normalized rms energy spread and the mean deviation form the mean energy for the electron bunch distribution taken from start to end simulation 52

5.7 The output power and spectrum of the seeded pulse relative to the SASE background for the electron bunch distribution taken from start-to-end simulation 53

5.8 The simulated spectrum of seeded pulse 54

5.9 The convolution function and probability of the overlap as a function of τ/σ_j. 56

5.10 The probability that the random jitter remains within a range which assures the overlap of $(C_{s,e}(\tau))$. 56

5.11 Probability of temporal overlap as a function of relative jitter 58

5.12 Probability of overlap as a function of electron bunch length 59

5.13 Probability of optimum overlap $(C_{s,e}(\tau) \geq 0.9)$ for different mean offsets of the laser pulse relative to the electron bunch (μ_s) 60

6.1 Coarse temporal overlap setup installed upstream seeding undulators. . . . 62

6.2 The operation principle of the streak-camera operation, FESCA200, Hamamatsu 63

6.3 Measured streak-camera (FESCA200) resolution. 65

6.4 Synchronization layout of the streak-camera with the master oscillator . . . 67

6.5 Schematic diagram of the modulator-radiator setup 68

6.6 Energy modulation within the modulator as a function of NIR-laser transverse size 69

6.7 Dependency of the 1^{st} harmonic modulation-amplitude on the compaction factor R_{56} for different slice energy spreads (σ_z) of the electron bunch. . . . 71

6.8 The enhancement of coherent light produced within radiator as a function of energy spread. 72

6.9 Logarithmic enhancement of the coherent light in the MOR setup. 72

6.10 Simulated bunching amplitude and emitted radiation using PERSEO . . . 74

6.11 Phase space of selected slices after modulator and radiator 74

6.12 Enhanced power within radiator, taken from PERSEO. 75

7.1 Layout of the coarse and fine longitudinal overlap setup 78

7.2 The remotely accessible optical beamline to the coarse timing setup 79

7.3 The coarse longitudinal overlap setup installed in the container. 80

7.4 The shielding test setup installed in the longitudinal overlap station, coordinate point 164 m in the FLASH tunnel 83

7.5 Experimentally beam photon transmission probability curves for Lead, Carbon Steel and heavy concrete 85

7.6 The constructed shielding box to protect the electronics and photo detectors against neutron and gamma radiation 86

7.7 Container side view and location of TLD pairs (600-700) in each side . . . 87

8.1 The dynamic range of a typical streak camera. 91

8.2 Reflectivity of grazing incidence mirror for the seed drive laser 92

8.3 The spectrum of the modulator/radiator undulator. 95

8.4 Dispersion curve through different materials used in the optical beam line . 100

8.5 Total Dispersion of the beam line 100

9.1 Measured longitudinal overlap between seed drive laser and electron bunch using the streak camera. 103
9.2 Longitudinal scan of the NIR laser pulse relative to the electron bunch . . 104
9.3 The phase scan of the vector modulator (Φ) and the relative temporal offset (ΔT) between seed pulse and electron bunch. 105
9.4 Relative jitter between seed drive laser and the electron bunch. 106
9.5 The electron bunch distribution measured with the TDS during the commissioning shift on Oct. 2010 106
9.6 The electron bunch properties and enhanced coherent signal seen by a CCD camera. 108
9.7 Two Gaussian fit applied on the scan data of the radiator radiation 108
9.8 Example of the scan results, (Apr. 2011) 110

10.1 The spectral and enrgy contrast between seeded signal and the SASE background. 113

A.1 The convolution of electron bunch and seed pulse distribution 117
A.2 The convolution of electron bunch and seed pulse distribution for different electron bunch length 118

D.1 Transmission of the seeding injection beamline for the NIR laser beam. . . 123

E.1 Thermoluminescence signal of TLD-600 and TLD-700 in different location around the shielding container 125

F.1 Transient time of visible wavelengths through different material used in the beamline 127
F.2 Transient time of visible wavelengths through lenses 128

List of Tables

1.1 Examples of seeded FELs . . . 7

3.1 ORS experiment parameters . . . 25

4.1 Energy of the HHG pulses. . . . 36
4.2 HHG divergence for different focusing mirrors . . . 36
4.3 HHG drive laser parameters . . . 37
4.4 Parameters of the seeding undulators. . . . 39
4.5 Spectral bandwidth of the SASE FEL in comparison with the HHG radiation 43

6.1 Specification of the streak-camera, FESCA200 . . . 64
6.2 The parameters used for the analytical study . . . 70
6.3 The electron beam and NIR laser pulse properties used for the PERSEO simulation. . . . 73

7.1 Measured gamma dose after lead and concrete shielding . . . 82
7.2 Neutron and gamma transmission for the Borated-Rubber shielding and concrete breaks . . . 83
7.3 The evaluated neutron and gamma dose for 500 working weeks of FLASH . 84
7.4 Measured gamma radiation and neutron flux transmission through constructed shielding container. . . . 85
7.5 Measured gamma radiation and neutron flux transmission through constructed shielding container. . . . 85
7.6 The result of gamma and neutron dosimetry around the shielding box at FLASH tunnel . . . 86

8.1 Efficiency of the beam line for the seed drive laser to the longitudinal overlap setup. 93
8.2 Measured energies of the synchrotron radiation of the radiator. 94
8.3 Measured attenuation of the seed-drive laser oscillator for different spectral filters. 96
8.4 Measured attenuation of the seed-drive laser oscillator for different neutral density filters. 97
8.5 Analytical estimation on the transmitted energy of the laser after different filters. 98
8.6 The estimated energies of the seed-drive laser and synchrotron radiation after different bandpass filters. 98

1 Introduction

In an attempt to find a broadly tunable source of coherent radiation, the development of the Free-electron laser (FEL) by John Madey and his collaborators in the 1970s [DEM$^+$77] was a challenging progress which overcame the constraints of conventional lasers. Substituting the active medium in conventional lasers, which are based on atomic structures, with free electrons was a step forward toward generating coherent radiation in the spectral range extending from infrared (IR) to visible way to ultraviolet (UV) and beyond to hard X-rays. To characterize molecular and atomic structures large number of photons focused on a sample as small as a molecule squeezed into a time of a few femtoseconds is required, in other words: the X-ray source must display high brightness. The brightness or brilliance of a source is the phase space density of the photon flux (i.e. the photons per unit solid angle per unit solid area), which is a true measure of the properties of the source [Cla04]. There are numbers of exciting experiments that this novel radiation source will make possible, including [BPN84]:

- Condensed matter: surface science, magnetic properties,
- Chemistry: taking atomic scale motion picture of chemical process, molecular vibrational excitation,
- Biology: microscopy, holography, cellular dynamics, DNA sequencing, unraveling the complex molecular structure of a single protein or virus,
- Medicine: medical diagnostics and treatment.

The Free-electron laser in Hamburg (FLASH) at DESY is a user facility providing a unique source of extremely bright, coherent and ultra short pulses of extreme ultra violet radiation and soft X-rays, enabling the researchers to explore the temporal evolution of physical, chemical, and biochemical processes occurring in femtoseconds or picoseconds [FLA07]. After an upgrade in 2010 the femtosecond FLASH pulses reached down to the 4.1 nm wavelength scale [Sch11b].

A comparison between the peak brilliance of advanced synchrotron radiation sources is shown in Fig. 1.1.

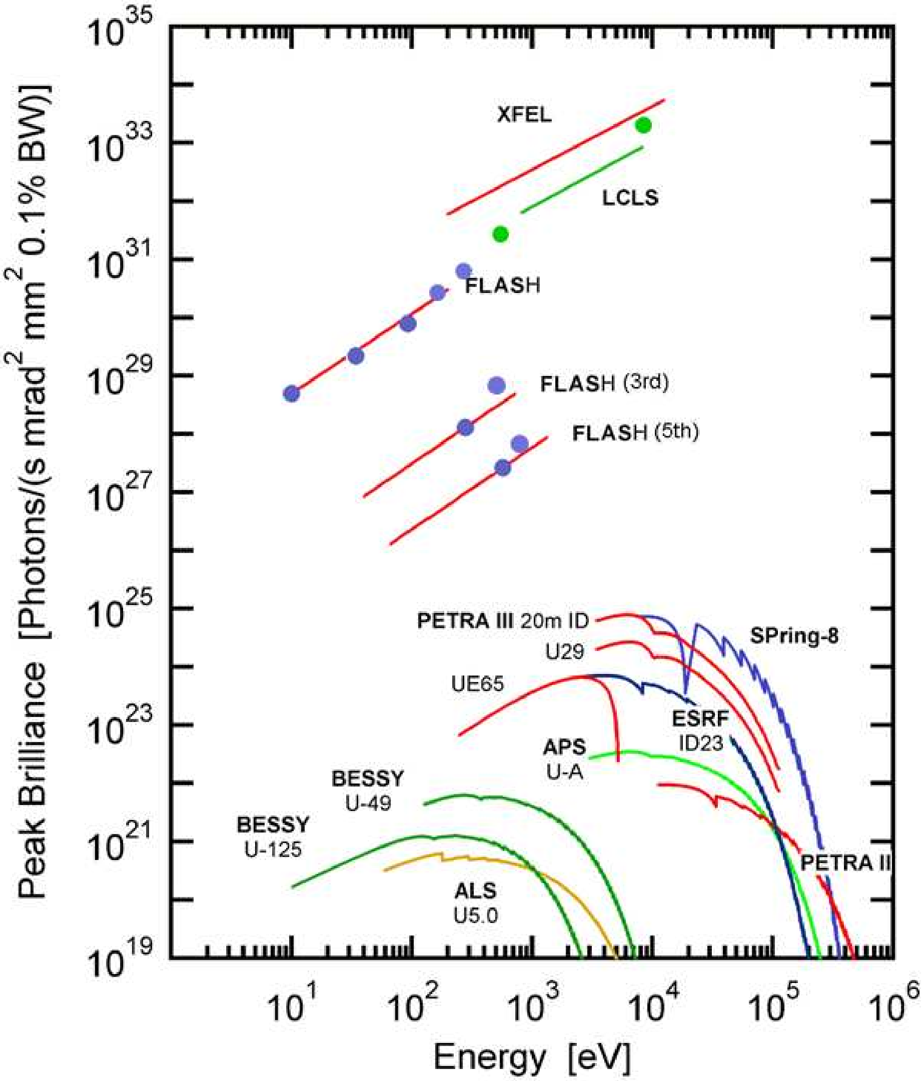

Figure 1.1: Peak brilliance of FLASH in comparison with XFEL and 3rd generation synchrotron radiation sources, adapted from Ref. [Sch10b].

In FLASH the electrons are produced in a laser-driven photoinjector and accelerated up to 1.25 GeV by a superconducting linac. To increase the peak current, the electron bunches are compressed at intermediate energies (150 MeV and 470 MeV) using magnetic chicanes, thereby increasing the current up to ∼ 2.5 kA. The electron bunches with high peak current and relativistic energies enter to a magnetic structure which is called undulator. The sinusoidal trajectories of the electrons within an undulator produce electromagnetic radiation with the wavelength proportional to the undulator period (λ_u), for example at FLASH the undulator period is $\lambda_u = 2.7$ cm over 27 m.

The interaction of electrons and the electromagnetic field within the undulator changes the energy of the electrons and consequently their trajectories within the undulator and therefore they tend to bunch, approaching each other to within one radiation wavelength. This process produces what is termed micro-bunching and results in an exponential growth of FEL radiation. The electromagnetic fields of those adjacent electrons superimpose in phase. Due to progressively increasing in micro-bunching the radiation power $\mathrm{P(z)} \sim \mathrm{P}_{in}\exp(\frac{z}{L_g})$ of such SASE FEL grows exponentially with the distance z along the undulator. Here P_{in} is the effective input power and L_g is the gain length over which the amplitude of the total field grows exponentially [SSY00, Pel02]. The interaction process in the undulator can start either with the aid of an external electromagnetic field, e.g. a laser or by the random synchrotron radiation noise produced by the beam in the undulator entrance. The radiation due to the latter case is called the Self-Amplified-Spontaneous-Emission (SASE) radiation. The spontaneous synchrotron radiation results from statistical fluctuations in the phase distribution of the electrons. As such, the SASE spectrum will reflect its random initialization strongly. A typical spectrum of the SASE FEL radiation and seeded FEL radiation with an external source, taken from a Genesis simulation code [Rei99] is shown in Fig. 1.2.

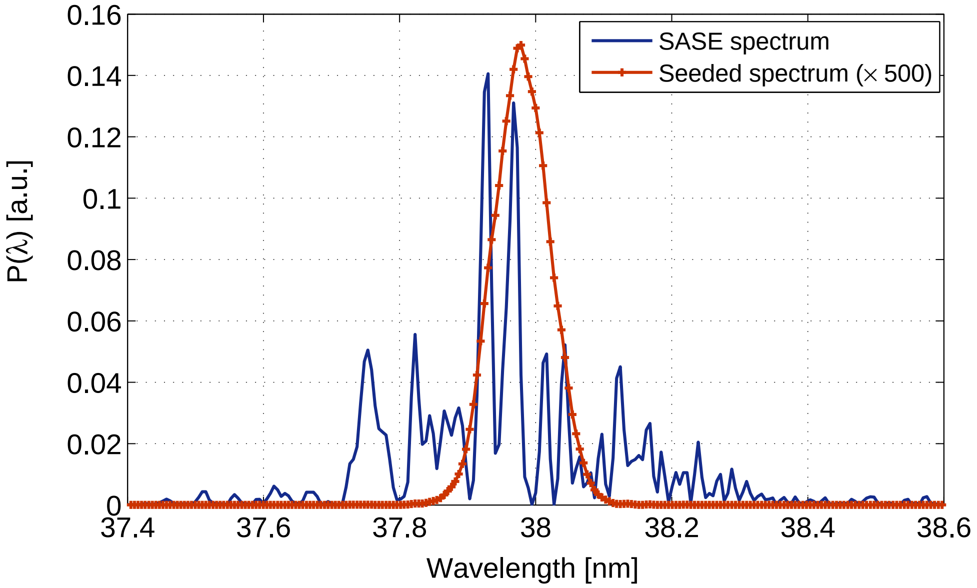

Figure 1.2: *The typical SASE spectrum, taken from GENESIS simulation. The resonance wavelength of the undulator is at 38 nm. The red curve shows the seeded spectrum. The coupled energy of the seed pulse is assumed to be 1 nJ.*

The shape of the SASE FEL spectrum is not smooth but has some random spikes. Further the full bandwidth is also not as narrow as a certain class of experiments would require. The reason for the wide bandwidth is that the coherence length inherent in the SASE process is shorter than the bunch length. Different longitudinal portions of the beam essentially lase independently. To overcome this problem the bunch length might be decreased (single spike with low charge) in which case the coherence length can be about the entire bunch length. Unfortunately, in such a case, the shot-to-shot fluctuations of output power would be excessively large and it becomes difficult to achieve the fully longitudinal coherence and control of the optical phase. Alternatively different configurations have been proposed to improve the performance of the FEL and to control the spiky nature of the output, such as side band FELs, and two stage FELs [FSS+97]. A most promising alternative approach is seeding the FEL with another source of radiation which has a high degree of temporal coherence. In this regard different schemes have also been proposed as discussed below.

1.1 Schemes to improve the longitudinal coherence

1.1.1 High Harmonic Generation (HHG)

This method can be used as a tool to directly seed the FEL with short wavelength radiation which is produced in a high harmonic generation (HHG) process. In a HHG process, as is explained in more detail in Chapter 2, an intense laser field interacts non-linearly with the gas atoms and coherent radiation at frequency multiples, or harmonics, of the fundamental laser is generated. The generated short wavelength radiation can be used as a source for the seeding the FEL in spectral regions that are not accessible in other ways.

1.1.2 High-Gain Harmonic Generation (HGHG)

In this concept the FEL process starts with an external laser field. The seed pulse interacts with the electrons in the first undulator section and energy-modulates the beam. After traversing a dispersive section this energy modulation is converted to a density modulation, as is shown in Fig. 1.3. The second undulator (the radiator) which is tuned to a higher harmonic of the seed wavelength emits and amplifies the coherent light from the inserted micro-bunched electron beam which contains micro-bunching Fourier content at the desired harmonic. This process continuous until the desired wavelength is achieved. In this approach it is better to start with the wavelength close to the desired one, since after each step (frequency conversion) the noise level increases and this degrades the quality of the final FEL output [BZDMK+91, YB+00].

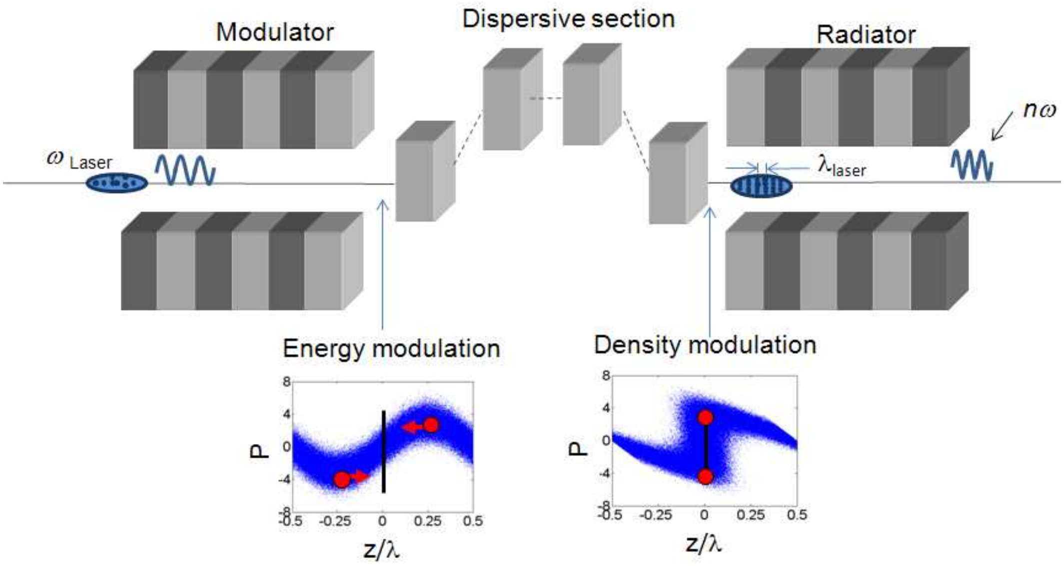

Figure 1.3: *HGHG seeding scheme. A laser with frequency ω modulates the energy of the electron bunch in the first undulator (modulator). Afterward the electron bunch traverses a dispersive section, and the energy modulation is converted to a density modulation. The second undulator, which is tuned to the desired harmonic of the fundamental wavelength of the laser radiates coherently in the tuned wavelength. The longitudinal phase space of the electron bunch before and after the dispersive section is shown [ftEt10].*

1.1.3 Echo-Enabled Harmonic Generation (EEHG)

Echo-enabled harmonic generation is a scheme which generates temporally coherent radiation by up-frequency conversion of a high-power seeding pulse [Stu10a]. In this scheme an external laser modulates the beam energy within the first undulator (modulator 1) and then passes a magnetic chicane. Subsequently a second laser modulates the beam energy in the successive undulator (modulator 2) which is tuned at the wavelength of the second laser. The beam travels then through the second dispersion section, where the energy modulated beam is converted to a density modulated system with very high harmonics obtained due to the strong compression induced in the dispersive sections. The evolution of the phase space structure of the electron bunch is plotted also in the Fig. 1.4.

1.1.4 Super-radiant Cascade Seeding (SCS)

In this method the undulators involved in the cascade sections are tuned at slightly different wavelengths, in which the fundamental frequencies have one of the higher harmonics in common. In this scheme a short intense seed pulse can generate a super-radiant pulse which seeds the following undulator at a common harmonic frequency. The bunching in

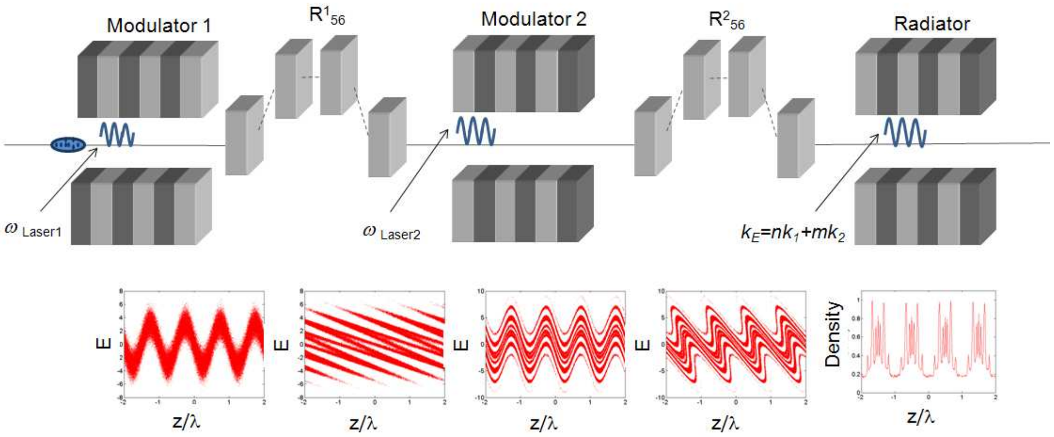

Figure 1.4: *EEHG scheme. The first laser modulates the electron bunch within the first undulator (modulator1); afterward the electron bunch travels through a strong magnetic chicane to over compress the phase space. By using a second laser with the same or different frequency as the first laser, certain correlations imprint on to the bunch. A second chicane is used to convert the energy modulation to the density modulation, [ftEt10])*

the first undulator contains higher harmonics which enhances the radiation in the second undulator at the modulated wavelength. The difference between this scheme with the HGHG method is that the distinction between modulator and radiator is no longer appropriate. The three step energy modulation, density modulation and emission take place simultaneously at different locations along the optical pulse. For more information on this scheme the reader is directed to Ref. [GSM05].

1.2 Examples of seeded FEL facilities

The HHG method was adopted for seeding at FLASH, because it is a straightforward implementation of modern technology and demands a physical footprint consistent with the existing laboratory. For some other FELs different approaches are used for seeding in the VUV-range. Examples of seeded FELs are given in Table 1.1.

A prerequisite condition for seeding the FEL is to satisfy a six-dimensional phase space overlap between the electron bunch and external seed pulse. These six-dimensions are defined as the spatial and angular in the two transverse directions and the spectral and temporal overlap of the seed pulse and radiation due to the electron bunch (longitudinal phase space). In this respect the longitudinal overlap of the seed pulse $(\leq 13\,\mathrm{fs})_{rms}$ and the interacting part of the electron bunch $(\leq 100\,\mathrm{fs})_{rms}$ is quite challenging. For example the best streak camera has a resolution only as good as a few hundred femtoseconds. So

Parameters	FLASH	Fermi@Elettera	SCSS	SPARC	LCLS-II
Seeding option	HHG	HGHG	HHG	Cascade	Echo
Seeding wavelength (nm)	38	4.2	61.5	160-266	6
Seed energy (nJ)	2	n.p*	2	$\leq$ 1 - 50	n.p
Laser wavelength (nm)	800	190-280	800	800	202
rms Laser duration (fs)	13	40-70	130	112	$\leq$100
Laser energy (mJ)	35	$\sim$ 5	100	2.5	0.075
rms bunch duration (fs)	$\geq$ 100	$\sim$600	700	2640	2-100
Electron energy (GeV)	1.25	0.9-1.5	0.250	0.178	4.3
References	[AAB+11]	[ANF10]	[TF+10]	[GPDC10]	[Stu10b]

* not provided

Table 1.1: *Examples of FEL seeding projects [sFE11].*

in this regard new techniques need to be developed to measure and adjust the temporal offset of two pulses within tens of femtoseconds precision.

1.3 Layout of this thesis

The relative simplicity of the HHG method, and available space in our existing FEL facility, makes this method the first choice for a seeding experiment. In this thesis one of the prerequisite steps for the HHG seeding experiment at FLASH is studied and discussed.

In Chapter 2 theoretical approaches on the FEL operation, SASE characteristics, electron and light interaction are presented. The theory of the HHG scheme for producing the XUV pulse as a source for the seeding is discussed more in detail in this chapter . In Chapter 3 of this thesis, the Free-electron laser facility in Hamburg (FLASH) is introduced. The existing diagnostics for the characterization of the longitudinal profile of the electron bunch are also discussed. The synchronization method of the electron bunch along the machine, which is also one of the preliminary steps to achieve the longitudinal overlap of the seed and the electron beam pulse is presented.

In Chapter 4 the installation of the entire seeding setup in the shutdown of 2009, the expected seeding characteristics, and techniques for achieving the fully six-dimensional overlap between the seed pulse and the electron bunch are discussed.

In Chapter 5, simulation results showing the tolerance on the relative temporal jitter between two femtosecond pulses, to achieve gain with seeding, are presented. Furthermore a statistical approach is used to predict the probability of the overlap between temporally jittering seed pulse and the temporally jittering electron bunch. The desired synchronization and the temporal overlap precision for the seeding experiment are discussed in the same chapter.

In Chapter 6 different methods are introduced for finding the coarse and fine temporal overlap between two pulses. Analytical investigations show that a modulator-radiator (MOR) setup can be used as a powerful tool for finding the temporal offset of two femtosecond pulses within 50 fs precision. The concept, possibilities and performance of that method is presented both analytically and experimentally in this chapter.

The layout of a remotely controllable timing diagnostic station, which is installed in the FLASH tunnel is described in detail in Chapter 7. The radiation shielding issues and the scheme for constructing the measurement station in the tunnel are also presented; thanks to the success of this system in the long term protection of the electronic devices against γ and neutron radiation it will be used in the future for the XFEL facility at DESY [XFE].

The discussion is continued over the optimization of the beamline of the longitudinal overlap station in Chapter 8.

The results which were achieved during the commissioning shifts for the seeding experiment are summarized in Chapter 9. These results include the streak camera-based measurements (coarse temporal overlap), temporal overlap using MOR setup (fine-temporal overlap) and the post analysis of some fine scans between the XUV pulse and electron bunch.

2 FEL principle and theoretical approach on the relativistic electron and light interaction

2.1 Light-electron interaction in FELs

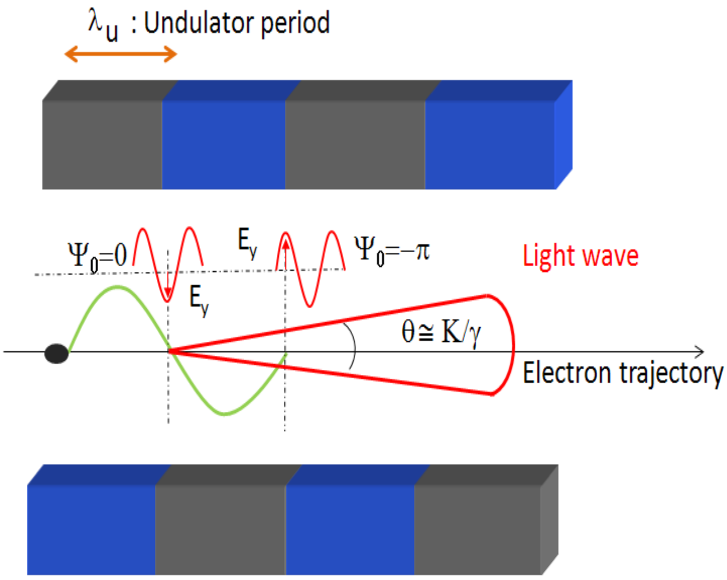

Figure 2.1: *The electron trajectory and light wave in an undulator.*

A Free-electron laser (FEL) uses relativistic electron bunches to produce electromagnetic radiation. Here in basic terms the physics of this process is described.

To prepare the electron beam for a high-gain FEL process [SDR08], electrons are accelerated to relativistic energies using accelerating modules. Using dispersive sections, the current density in the bunch is increased by shortening the time duration of the electron pulse. The relativistic electrons with high peak current (∼ kA) enter a magnetic structure which is called undulator, which is consisting of a periodically alternating transverse magnetic field. The interaction process within an undulator is such that kinetic energy of the relativistic free electrons is converted to electromagnetic radiation in the undulator magnet by interaction with the existing radiation wave. This interaction is mediated by the undulator magnets, which force the electron bunch to a sinusoidal trajectory. The motion of an ultra-relativistic electron traveling along the axis of a planar undulator can be approximated by [SDR08]:

$$z(t) = \bar{v}_z t - \frac{K^2}{8\gamma^2 k_u}\sin(2\bar{v}_z k_u t),\ \ x(t) = \frac{K}{\gamma k_u}\sin(\bar{v}_z k_u t) \tag{2.1}$$

where $k_u = \frac{2\pi}{\lambda_u}$, $K = \frac{eB_u\lambda_u}{2\pi m_e c}$ is the undulator parameter, and B_u is the peak magnetic field of the undulator, λ_u is the period of the undulator magnet, and the average longitudinal velocity of the electron ($\bar{v}_z$) is:

$$\bar{v}_z = c\cdot(1 - \frac{1}{2\gamma^2}(1 + \frac{K^2}{2})) \tag{2.2}$$

Lasing occurs because the undulator and the radiation combine to produce an interference pattern termed a ponderomotive wave that travels slower than the speed of light. The time for an electron to travel one undulator period is $t = \frac{\lambda_u}{\bar{v}_z}$ while light wave travels a distance of $\lambda_u + \lambda_l$ in the same time. For a net energy exchange the relative phase of the electron and the ponderomotive wave must be stationary, and thus the synchronization condition should satisfy [MP90]:

$$\begin{aligned} \frac{\lambda_u}{\bar{v}_z} &= \frac{\lambda_u + \lambda_l}{c} && (2.3)\\ \beta_z &= \frac{\omega/c}{k + k_u} && (2.4) \end{aligned}$$

stating that the electron velocity $\beta_z = \frac{\bar{v}_z}{c}$ should be equal to the phase velocity of the ponderomotive wave with a wave number of electromagnetic and undulator field $(k + k_u)$ and frequency of ω. This wave travels slower than speed of light and can be synchronized with the electrons under the condition presented in Eq. 2.3, which indicates that the light emitted overtakes the electron by one wavelength per undulator period. Using Eq. 2.2 and Eq. 2.3 the resonance condition for undulator radiation is obtained as follows [MP90]:

$$\lambda[nm] = 1.306\frac{\lambda_u[cm]}{E^2[GeV]}(1 + \frac{K^2}{2}) \tag{2.5}$$

where E is the electron beam energy, $K = 0.934\cdot B_u[T]\cdot\lambda_u[cm]$ is the undulator parameter. The radiation emitted from a relativistic electron is within a narrow cone with opening angle of $1/\gamma$ [Jac99]. The axis of this cone is tangential to the sinusoidal trajectory within the undulator magnet, whose maximum angle with respect to the axis is [SDR08]:

$$\theta_{max} \approx K/\gamma_0 \tag{2.6}$$

For the case of an undulator with $K << 1$ the Fourier transform of the radiation on axis due to the sinusoidal electric field would have just one component, the fundamental. For $\theta > 0$, both even and high harmonics of undulator radiation can be observed as follows [MP90]:

$$\lambda = \frac{\lambda_u}{2m\gamma^2} \cdot (1 + K_{rms}^2 + \theta^2\gamma^2) \tag{2.7}$$

where m is the Fourier harmonic number.

The stochastic density modulation within the bunch generates spontaneous radiation. This radiation, which serves as a seed pulse, is exponentially amplified along the undulator. This process is called Self-Amplified Spontaneous Emission (SASE) and is shown in Fig. 2.2. The open red circles are the measurement points achieved at FLASH and the solid line shows the theoretical prediction. The progress of micro-bunching along the undulator is shown schematically in the same figure.

The SASE can be achieved provided a set of proper conditions are obtained for the electron bunch quality. The longitudinal charge distribution and the transverse size (σ_r) of the electron bunch play an important role in determining the efficiency of the lasing process. The dependence of the FEL power gain in the one-dimensional limit (ignoring, e.g., diffraction) on the beam current I and transverse root mean square (rms) size of the electron bunch σ_r, is defined in the following formula:

$$\begin{aligned} L_G &= \frac{\lambda_u}{4\pi\rho\sqrt{3}} \\ &\propto \gamma(\frac{\sigma_r^2}{I_0})^{1/3} \end{aligned} \tag{2.8}$$

where ρ is the FEL parameter, depending to the undulator parameter K, and the period of the undulator magnet λ_u [BPN84]:

$$\rho = \{\frac{I}{I_A}\frac{\gamma\,\lambda_r^2}{16\,\pi^2\,\sigma_{trans}^2}\frac{K^2}{(1+K^2/2)^2}[J_0(\frac{K^2}{4+2K^2}) - J_1(\frac{K^2}{4+2K^2})]^2\}^{1/3} \tag{2.9}$$

where γ is the Lorenz factor, $I_A = \frac{mc^3}{e}$ =17 kA is the Alfven current, $J_{0,1}$ are Bessel functions, σ_{trans} is the electron transverse (rms) size. Equation 2.8 reveals that a small

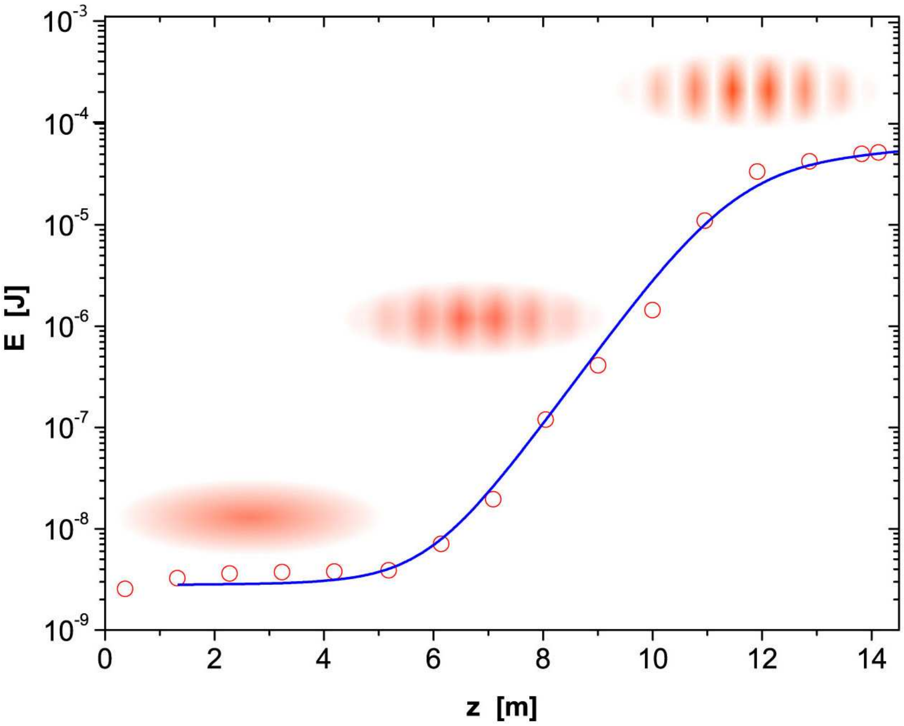

Figure 2.2: *The exponential growth of the FEL pulse energy E as a function of the length z traveled in the undulator. The open red circles are measurement points achieved at FLASH for the electron energy of 245 MeV. The solid curve shows the theoretical prediction. The progress of micro-bunching is indicated schematically, adapted from Ref. [FLA07].*

emittance ($\sigma_r^2 = \epsilon\beta$) and high peak current are required for shortening the gain length in high gain FELs.

In principle for the generation of maximally coherent radiation, the longitudinal bunch length σ_z should be smaller than the wavelength of the radiation. In other word, a relativistic electron beam moving in a sinusoidal orbit can radiate coherently if the wavelength of the synchrotron radiation exceeds the length of the bunch ($\lambda_L \geq \sigma_z$). There is a limit for the shortening of an electron bunch, using standard compression techniques, due to space charge effects. But the energy exchange between electrons within the bunch and the radiation field can generate micro-bunches which are spaced at, and are thus shorter than, the radiation wavelength and thus radiate coherently. These micro-bunches are created due to the fact that, depending on their location in the ponderomotive wave, some of the electrons give up energy to the radiation, lose momentum and go through a longer sinusoidal path and fall behind an electron with no energy change; those that gain energy on the other hand, move forward. This process thus produces bunching with period equal to the undulator radiation wavelength which is given in Eq. 2.5.

Assuming full transverse coherence the total radiation power averaged over an ensemble is as follow:

$$< P(\omega) >= P(\omega) N (1 + (N-1) \mid \hat{f}(\omega)^2 \mid) \tag{2.10}$$

where P(ω) is the radiation power from a single electron, N is the number of electrons within the bunch and $\hat{f}(\omega)$ is the Fourier transform of the longitudinal distribution function of the beam $f(z)$, normalized by $\int_{-\infty}^{\infty} f(z)\,dz = 1$. The first term of Eq. 2.10 is due to incoherent radiation, and the second term - to coherent radiation. The total radiated power of the coherent radiation is:

$$P_{coh} = N \cdot P_{incoh} = N \cdot N \frac{e^2 c \gamma^4}{6\pi\epsilon_0 r^2} \tag{2.11}$$

where P_{incoh} is the incoherent radiation power at the respective wavelength, r is the radius of curvature of the particle trajectory in a bending magnet.

SASE-FEL bandwidth

The spectral bandwidth of SASE radiation varies at different points along the undulator, as it is shown in Fig. 2.3. In the first part, which is called undulator regime, the radiation is an incoherent superposition of radiation from any individual electron. In this part due to finite electron bunch emittance, the radiation is partially transversely coherent. Further on due to SASE interaction and modulation in the electron bunch the intensity and coherence are enhanced and the radiation amplitude increases exponentially. The growth stops due to the energy spread caused by the SASE interaction itself [Kim86]. The SASE bandwidth in saturation as well as undulator regime is $\frac{\Delta\omega}{\omega} \approx \frac{1}{N}$, where N is the number of undulator periods. In the exponential regime the bandwidth is $\frac{\Delta\omega}{\omega} \approx \frac{\sqrt{\rho N}}{N}$.

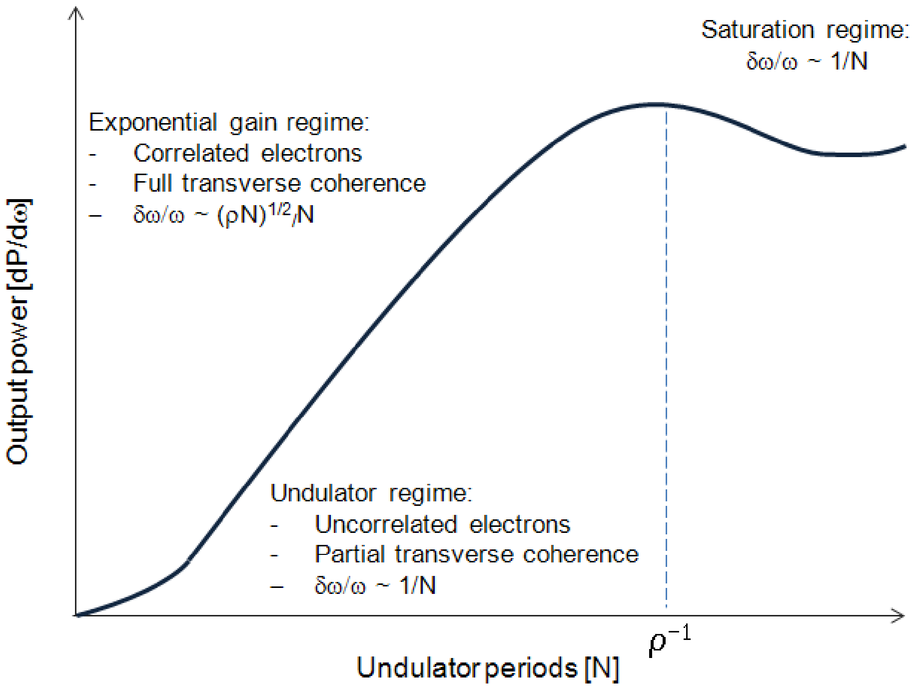

Figure 2.3: *SASE characteristics along the undulator. In the undulator regime, the radiation is transversely partially coherent due to the finite bunch emittance ($\rho N \ll 1$). In the exponential gain regime, the radiation intensity and coherence is increased due to FEL interaction, and the radiation amplitude is increasing exponentially. The growth continues to the point ρ^{-1}, where the energy spread generated due to the FEL interaction itself stops the further growth of the radiation saturation regime. The bandwidth in saturation as well as undulator regime is* $\frac{\Delta\omega}{\omega} \approx \frac{1}{N}$*, where N is the number of undulator periods [Kim86].*

Properties of the SASE radiation

Starting from shot noise (random electron longitudinal positions within the bunch), the undulator and as a consequence the SASE radiation shows random variation and fluctuation in the spectral domain. As was shown in Fig. 1.2, the SASE radiation shows several spikes with different height. The number of individual spikes, which can be assigned to longitudinal modes, can be calculated as $M = \frac{T_{bunch}}{\tau_{coh}}$, where T_{bunch} is the electron bunch temporal distribution and τ_{coh} is the coherent time (a time over which there is a correlation in the field, which is the slippage that occurs during one gain length, $\lambda_r \times \frac{L_g}{\lambda_u c}$). The so-called gamma distribution function, yields variance of the normalized FEL pulse energy and the number of longitudinal modes [SSY03].

$$p_M(u)du = \frac{M^M \cdot u^{M-1} \cdot exp(-Mu)du}{\Gamma(M)} \tag{2.12}$$

where u is the normalized pulse energy and $\sigma_u^2 =< (u- < u >)^2 >= \frac{1}{M}$.

In Fig. 2.4 the measured probability distribution of the SASE pulse energy for the wavelength of 5.7 nm at FLASH is shown [FLA11]. The blue curve is the gamma distribution (Eq. 2.12) which fits nicely to the measured probability distribution of the FLASH pulse energy in linear regime. From this curve the coherence time is estimated to be 4 fs. The number of modes is measured 9.5 and the fluctuation in FEL pulse energy is 32.5%. The number of modes decreases for shorter electron bunches. For the case that the electron bunch duration is equal to the coherence time, only one mode would exist, which in a spectral domain would mean a single spike thus an ideal situation from the time-bandwidth product viewpoint. On the other hand, Eq. 2.12 indicates that the fluctuations in output power are maximized in this case.

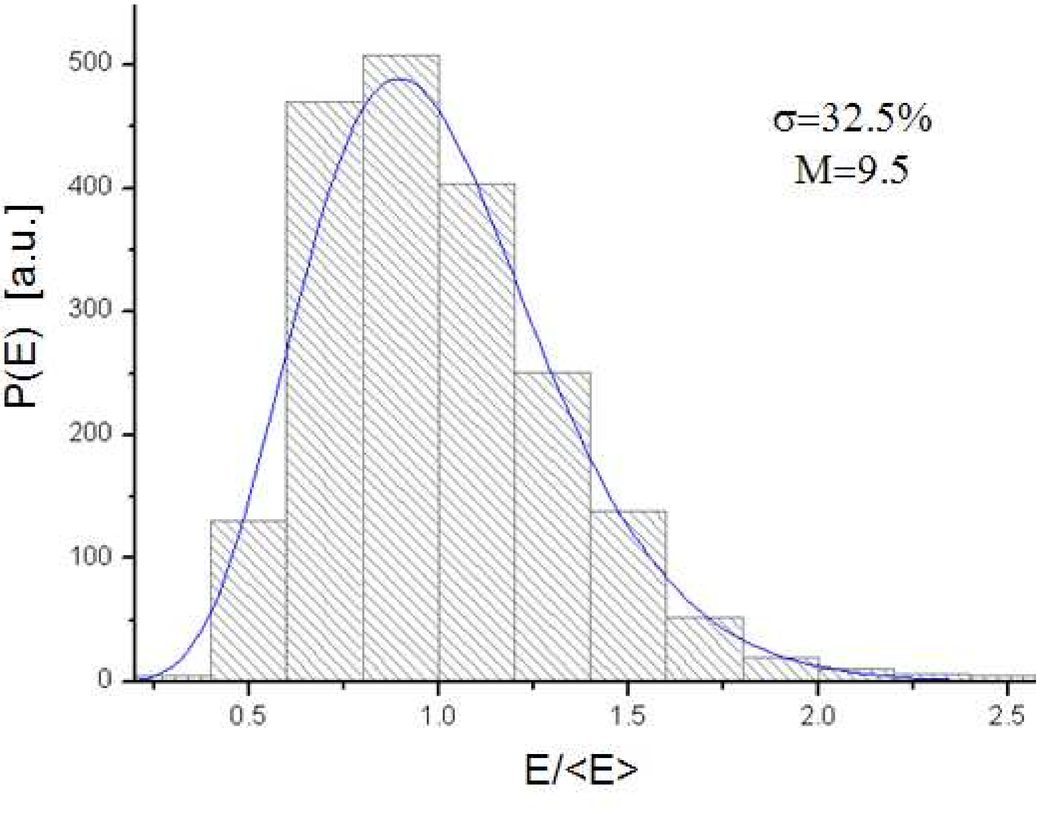

__Figure 2.4:__ Measured probability distribution of FLASH pulse energy in the linear FEL-regime at a wavelength of 5.7 nm. The blue curve is the gamma distribution which is plotted for the energy variance of 32.5%. The number of modes are 9.5 which yields 4 fs coherence time for a 40 fs pulse length, adapted from Ref [FLA11].

2.2 Seeding process in FEL

One approach to improve the longitudinal coherence of the SASE FEL is to seed the electron bunch by an external fully coherence light source within an early undulator section, see Fig. 2.5.

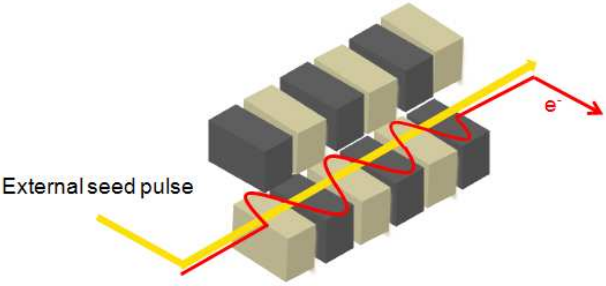

Figure 2.5: *Seeding undulator by an external light source.*

The energy exchange between the relativistic electron bunch and the light wave can be expressed as follows [MP90]:

$$\frac{d\gamma}{dt} = -\frac{e}{mc}\vec{E}\cdot\vec{\beta} = -\frac{e}{mc}E_x\beta_x \tag{2.13}$$

where E is the electric field of the light wave and $\beta_x = \frac{K}{\gamma}cos(k_u z)$ is the transverse component of the electron velocity normalized to c. Here K and k_u are undulator parameter and wave number, respectively. For energy exchange the electron bunch velocity must have a component parallel to the electric field of the wave. Assuming a plane wave with constant amplitude which co-propagates with the electron bunch ($E_x(z,t) = E_0 cos(k_l z - \omega_l t + \psi_0)$) one can rewrite Eq. 2.13 as follows:

$$\begin{aligned} \frac{d\gamma}{dt} &= -\frac{e}{mc}E_x\beta_x \\ &= -\frac{e}{mc}E_0 cos(k_l z - \omega_l t + \psi_0)\frac{K}{\gamma}cos(k_u)z \\ &= -\frac{eE_0K}{2\gamma mc}(cos\psi - cos\bar{\psi})) \end{aligned} \tag{2.14}$$

where $\psi(t) = (k_l + k_u)z - \omega_l t + \psi_0$ is the ponderomotive phase and $\bar{\psi} = \psi - 2k_u z$ is the fast oscillating phase. If the undulator is sufficiently long the energy modulated beam converts to the density modulated one and the electrons self-bunch at one radiation wavelength. The same process happens inside an optical klystron where the three steps of energy modulation, density modulation, and emission of coherent radiation occurs separately within a modulator-undulator, dispersive section, and a radiator-undulator, respectively.

2.3 Optical klystron concept as a tool for generation of coherent radiation

Optical klystron (OK) is yet another concept which has been used to generate coherent harmonic radiation [CD82]. An OK is constituted by two short undulators, separated with a dispersive section. In the first undulator (the modulator), an electron beam is interacting with the radiation field of an external laser, or by the spontaneous radiation of the electron beam itself, receives an energy modulation which can be transformed to a density modulation within a chicane and coherently enhances the emission of the radiation in the following undulator (the radiator), Fig. 2.6.

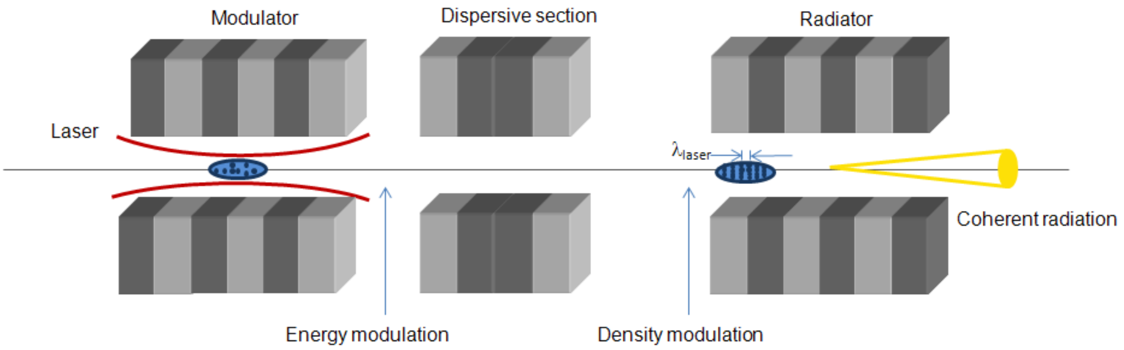

Figure 2.6: *Principle of operation of the optical klystron.*

Assuming a normal distribution for the particles before the fist undulator ($f_0(P) = \frac{1}{\sqrt{2\pi\sigma_E^2}} e^{-\frac{P^2}{2\sigma_E^2}}$) the phase-space distribution in the first undulator becomes $f(P, \psi)$, where $P = E - E_0$ is the energy deviation of the particles, σ_E is the slice energy spread and $\psi = \frac{2\pi z}{\lambda}$ is the phase of the particles. The distribution of the particles at the entrance of the dispersive section is $f_0(P - P_0 sin(\psi))$, where $P_0 sin(\psi)$ is the induced energy modulation within the electron bunch. After the dispersive section, the particles with energy deviation of P will come to the new phase $\psi - P\frac{d\psi}{dP}$ and consequently to the new phase-space distribution of $f(P - P_0 sin(\psi - P\frac{d\psi}{dP}))$. Here $\frac{d\psi}{dP}$ is the dispersion strength parameter [Sal05]:

$$\begin{aligned} \frac{d\psi}{dP} &= \frac{2\pi}{\lambda}\frac{dz}{\delta E} \\ &= \frac{2\pi}{\lambda}\frac{R_{56}}{E_e} \end{aligned} \tag{2.15}$$

where E_e is the energy of the electron, and $R_{56} = \frac{\lambda}{2\pi}\frac{E_e}{\sigma_E}$ is the optimum longitudinal compaction factor. Here $dz = R_{56}\frac{\delta E}{E_0}$ is the path length difference between particles with reference energy (E_0) and particles with energy of ($\delta E + E_0$). The δE can be due to energy modulation with amplitude (P_0) and also due to the energy spread (σ_E).

The integration of the phase-space distribution over the energy provides the beam density distribution, and a Fourier expansion of that would reveal harmonic components of the density modulation. The micro-bunching amplitude for the fundamental component of the bunched beam current is given by [Sal05]:

$$a_1 = 2J_1\,(P_0\frac{d\psi}{dp})\,exp\,(-\frac{1}{2}\,(\frac{d\psi}{dP})^2\sigma_E^2), \tag{2.16}$$

where P_0 is the amplitude of induced energy modulation, and $P_0\frac{d\psi}{dP} = \frac{2\pi}{\lambda}\frac{R_{56}}{\delta(E)}$ is the so called bunching parameter. The Bessel function accounted to energy modulation (P_0) and the exponential term accounted to the energy spread (σ_E). When energy spread is negligible the only contribution would come from the Bessel function. The normalized output power of the first harmonic after a planar undulator can be obtained as follow [Sal05]:

$$\begin{aligned}\hat{W} &= \frac{W}{W_0} = F(N_D) \qquad (2.17)\\ &= \frac{2}{\pi}\{arctan(\frac{1}{2N_D}) + Nln(\frac{4N_D^2}{4N_D^2+1})\},\end{aligned}$$

where $N_D = \frac{2\pi\sigma_r^2}{\lambda L}$ is the diffraction parameter and depends on the undulator length L, the resonance wavelength λ and the transverse size of the electron beam σ_r.

The normalization factor W_0 for the planar undulator is given by [Sal05]:

$$W_0 = \frac{K^2}{2+K^2}\frac{I}{\gamma I_A}\frac{\pi^2 a^2}{2}A_{JJ}^2 N_u W_b, \tag{2.18}$$

$$A_{JJ} = \{J_0(\frac{K^2}{4+2K^2}) - J_1(\frac{K^2}{4+2K^2})\},$$

where $W_b = m_e c^2\gamma I_0/e$ is the total power of the beam, N_u is the number of undulator periods, $I_A \approx 17kA$ is the Alfven current, J_n is the Bessel function of the n^{th} order and a is the amplitude of the modulation.

The radiation power from the modulated beam is above the incoherent radiation power when the amplitude of modulation a exceeds the shot noise level:

$$a > \frac{1}{\sqrt{N_u N_\lambda}} \tag{2.19}$$

where $N_\lambda = \frac{I\lambda}{ec}$. The incoherent radiation power into the central cone can be estimated by [Sal05]:

$$W_{incoh} = 4\pi^2 \frac{eI}{\lambda} \frac{K^2}{2+K^2} A_{JJ}^2 \tag{2.20}$$

The enhancement of the power in the radiator can be used as an indicator for the overlap between the electron bunch and the external seed laser field, which in this case provides the modulating field in the optical klystron. The potential of this concept, as a fine resolved method for finding the temporal overlap between two femtosecond pulses, is discussed more quantitatively in Section 6.2.

2.4 Theory of the High-order Harmonic Generation (HHG)

The physics behind HHG production can be understood with a semi-classical model. In this process, a high intensity, low-frequency laser interacts nonlinearly with many-electron atoms, and yields shorter wavelength, harmonic radiation. In HHG the atoms are ionized in the strong field of the laser and an ion and free electron pair is produced. The quasi-free electron accelerates in the field of the laser, and with the change in the sign of laser field it is driven back to the atomic core, recombining with the ion. In this process the kinetic energy of the electron E_{kin} together with the binding energy is emitted as a photon with the frequency of $\omega = \frac{(E_{kin}+I_P)}{\hbar}$, where I_P is the atomic ionization potential [FLL$^+$88, MGJ$^+$87]. The three step model for generation of higher harmonics [Cor93] is shown in Fig. 2.7.

This process repeats every half cycle of the driving laser, so that the emitted radiation is periodic with a periodicity of 1.3 fs for the 800 nm driving laser.

The harmonic spectrum drops down for the first few harmonics and then it shows a plateau over which the intensity is the same for the rest of the harmonics until it reaches a sharp cutoff. The cutoff is a limit of the highest harmonic orders, which can be generated efficiently. The maximum energy at the end of the plateau is $\Omega_{max} = I_p + 3U_p$ where $U_p = \frac{E^2e^2}{4m\omega^2}$ is the ponderomotive energy in the laser field of strength E and frequency of ω. Here m and e are the mass and charge of the electrons.

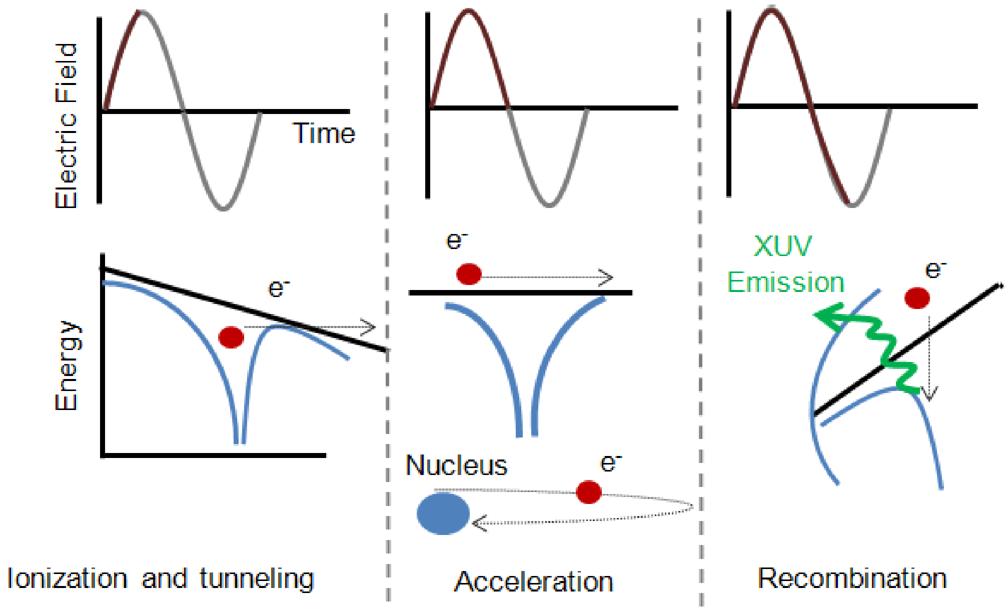

Figure 2.7: *Schematic of the HHG process. left: The strong laser field overcomes the Coulomb barrier in the atom, so the electrons can tunnel out and become separated from the atom. middle: The free electron accelerates in the field of the laser and when the sign of the field is reversed (right), the electron accelerates back towards the nucleus, and during the recombination process a photon with higher energy is emitted.*

2.4.1 Phase matching

Harmonics which are generated in different positions in the medium must interfere constructively in order to build up the harmonic intensity. The condition for the phase matching is:

$$\Delta\vec{k} = q\vec{k}_L - \vec{k}_q = 0 \tag{2.21}$$

where k_L is the laser wave number, and k_q is the wave number of the q^{th} harmonic. If this condition is not satisfied, the coherent growth of the harmonic would take place over the coherence length, $L_c = \pi/\Delta k$ as shown in Fig. 2.8.

The source of phase difference between the qth harmonic and the driving laser in a gas-cell target can be classified as follows [All04, HMS$^+$09, DRB$^+$99]:

- Neutral gas dispersion, $\Delta\Phi \approx \frac{2\pi P(1-\eta)\delta(\lambda_L)}{\lambda}$,
  where P is the pressure in atmosphere, η is the ionization fraction, $\delta(\lambda_L)$ is the difference between the indices of refraction of the gas at the fundamental and harmonic wavelengths.

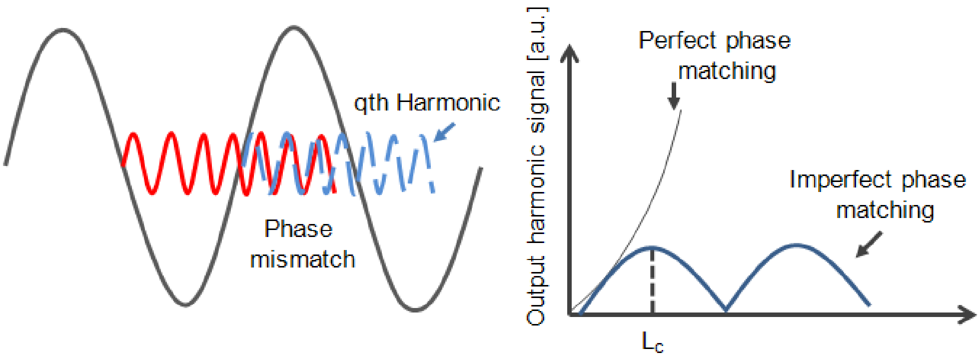

Figure 2.8: *left: The phase mismatch. Right: The growth of harmonic power as a function of the longitudinal coordinate z [Lyt08].*

- Plasma dispersion, $\Delta\Phi \approx P\eta N_{atm} r_e \lambda_L$,
  where N_{atm} is the number density in one atmosphere and r_e is the classical electron radius. By tuning the gas pressure the contribution of neutral atom and electron plasma can be canceled out.

- Geometrical phase shift, $\Phi_g(z,t) = q \arctan(\frac{z}{z_R})$,
  where z_R is the Rayleigh length of the driving laser. To avoid this so-called Guoy phase shift one should use larger laser beam size, by de-focusing the beam. This in turn means that higher laser energy is required.

- Single-atom dispersion, $\Phi(z,t)_j = \alpha_j \cdot I(z,t)$,
  The single atom phase Φ_j which strongly depends on the coefficients of the long and short trajectories (α_j) and can be estimated as above for the plateau region, for $I \approx 10^{14}\frac{W}{cm^2}$.

The so-called long quantum trajectory results from the electrons which are ionized immediately after the peak of the laser field and re-encounter the ion after a relatively long excursion (up to full cycle of the laser). A short quantum trajectory results from the electrons that are ionized shortly after the peak of the laser field and propagate for half a laser cycle [ZL$^+$08]. Their different responses to the variation of the laser intensity is the source of HHG temporal and spectral incoherency. By varying the focusing conditions and geometry, the two contributions can be distinguished to some extent [BLT$^+$98]. The HHG concept was chosen as a source of coherent radiation for the seeding experiment at FLASH. The experimental setup is presented in more detail in Chapter 4.

3 Longitudinal electron beam diagnostics at FLASH

The free electron laser in Hamburg (FLASH) is a user facility which produces ultrashort photon pulses (50-200 fs)$_{\mathrm{FWHM}}$ with wavelength down to 4.1 nm [Sch11b]. The average single pulse energy is (10-400) μJ. The layout of the FLASH is shown in Fig. 3.1.

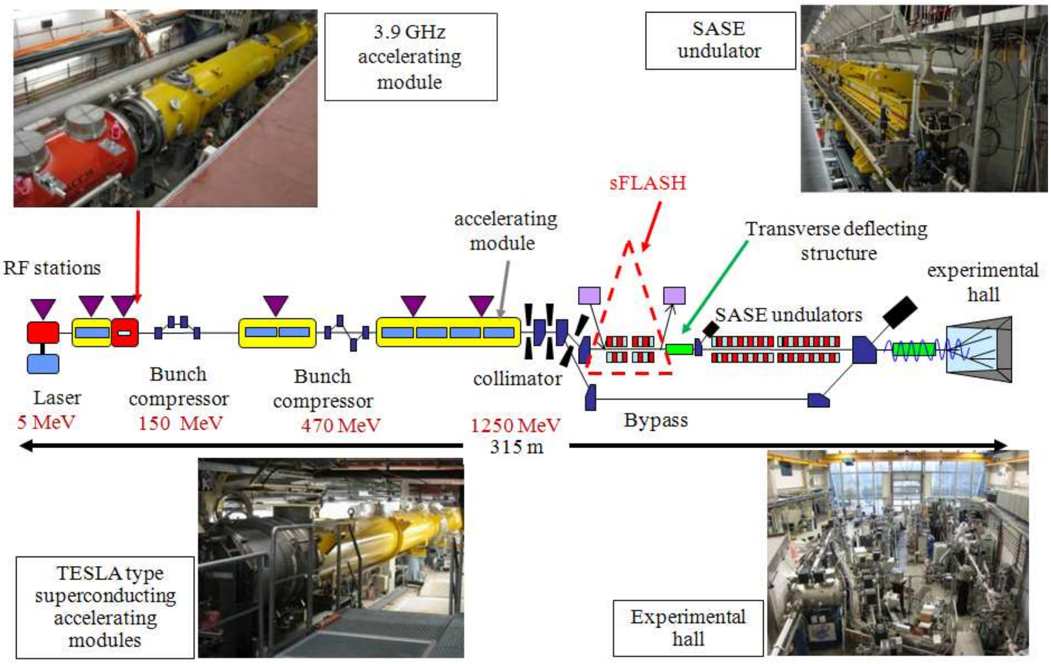

Figure 3.1: *The Free-electron laser in Hamburg (FLASH), adapted from [Sch10a].*

In FLASH the high-charge-density electron bunches which are required for the SASE operation, are produced in the UV-laser-driven photo injector. The initial acceleration happens in the RF gun cavity, with 1.3 GHz resonance frequency. The electron bunch is accelerated quickly to relativistic energies, to avoid the space charge effect that repels them from each other, which can produce both bunch lengthening and emittance growth. Electron bunches reach 1.25 GeV after traversing seven accelerating modules. As discussed in the previous chapter, three prerequisite conditions for the SASE process in an FEL are: high peak current, very low emittance, and small energy spread. To reach high peak current, two bunch compressors are installed to longitudinally compress the electron bunch at moderate energies. Bunch compression requires that the electron bunches accelerate off-crest in the RF field and obtain an energy chirp. After the two bunch compressor sections the electron bunch current rises to ~ 2.5 kA. Afterwards, the electron bunches enter the 27 m long undulator section and, depending on the energy of the electron and undulator characteristics, coherent radiation down to 4.1 nm can be produced. In the SASE FEL an ultrashort, high-peak-current relativistic electron bunch is used to amplify its own spontaneous emission radiation in one pass through the undulator until it reaches saturation. In order to monitor the longitudinal profile of the electron bunch, which plays an important role in the SASE process, different experimental setups are installed in the FLASH tunnel. In the 2009 shutdown, a third harmonic accelerating module was installed in the FLASH tunnel. This module is employed to minimize the correlated, nonlinear energy spread along the bunches. The cosine-like accelerating field induces an energy spread over the length of the bunch. The 3^{rd} harmonic of the fundamental frequency is used to linearize the RF field distribution in the vicinity of the bunch, allowing more efficient bunch compression. Flattening also reduces the growth of transverse phase space. The installed module at FLASH operating at 3.9 GHz consists of four nine-cell cavities [VAB+10]. With installation of this module, FLASH has obtained three operation modes with long, intermediate, and short bunch length. Different diagnostics for characterizing the longitudinal phase space are installed at FLASH, from which the seeding project benefits. In this section a short description of each experimental station is presented.

3.1 Optical Replica Synthesizer (ORS)

This method is used to measure the longitudinal profile of the ultra relativistic electron bunches in FLASH by creating an optical pulse with the same longitudinal profile as the electron bunch [Sal05]. This is achieved by energy modulating the electron bunch with a relatively long external laser within a short undulator (the modulator, vertically polarized), which produces spontaneous radiation with the same polarization as the laser. After traversing a magnetic chicane, the energy modulated beam is converted to the density modulated one. Following that the micro bunched electrons will emit coherent radiation in the second undulator (the radiator, horizontally polarized) which is resonant at the laser (or double) frequency [AZM+08]. Using frequency-resolved optical grating techniques the electron bunch profile can be extracted from the optical pulse [Tre00]. Differing polarizations in modulator and radiator are used to separate the seed laser from the generated coherent radiation. The parameters of the ORS undulator is indicated in Table. 3.1.

Parameter	Value
Undulator period length	200 mm
Max magnetic field	0.42 T
Number of periods	5
Max K value	7.8
Gap diameter	38 mm
Undulator length	z=1 m
R_{56} of the chicane	0 - 150 μm
Laser pulse length	$(200\text{ - }3000\,\text{fs})_{FWHM}$

Table 3.1: *ORS experiment parameters.*

A conventional fast photodiode and optical transition radiation (OTR) screens were used to measure the temporal and spatial overlap between laser and electron in the modulator section [AZM$^+$08]. The amplitude of the energy modulation, phase-space distribution of the particles in each step (modulator, dispersive section and radiator) and the enhanced power are discussed in detail in Chapter 6.

3.2 Transverse Deflecting Structure (TDS)

The transverse deflecting structure (TDS) is used for mapping the longitudinal profile of the bunch, slice emittance and correlated energy spread measurements [Bg11]. This diagnostic is installed upstream of the FLASH undulator and consists of a vertical deflecting RF structure (2.856 GHz) and a subsequent drift to a transverse profile monitor. The transverse RF field in a cavity is used to separate the head and tail of the electron bunch, and thus the TDS translates the longitudinal coordinate into the transverse one. Use of a horizontal kicker and an off-axis screen make the parasitic operation of the TDS with the FLASH operation possible. The theoretical resolution of the measurement is 10-50 fs [Bg11].

3.3 Terahertz and Optical SYnchrotron radiation LABoratory (TOSYLAB)

Downstream of the first bunch compressor, named BC2, the TOSYLAB beamline transports the full synchrotron radiation of the third magnet in the bunch compressor. A crystalline quartz window, which separates the beam vacuum with the experimental station, transmits a large fraction of the radiation spectrum. The coherent far-infrared and incoherent visible synchrotron radiation from the FLASH bunch compressor is used to measure the longitudinal profile and stability of the electron bunch [GBRS08]. Using a conventional streak camera a direct time domain measurement has been performed with resolution of better than 500 fs [Ham10]. For the accelerating phase of 6 ° forward of crest in the first accelerating module, which is located upstream of the first bunch compressor, the rms bunch length is measured to be about 2.5 ps [GBRS08].

3.4 Electro Optical Sampling (EOS)

In this non-invasive method the electric field of the electron bunches is used to extract information about the longitudinal charge distribution of the electron bunch in the sub-picosecond domain [CSS+05]. For a highly relativistic electron bunch moving in a straight line in vacuum, the local electric field is almost entirely concentrated perpendicular to its direction of motion [WMG+02, YMG+00]. Detection of this field as a function of time at a fixed position therefore provides a way to determine the length and longitudinal shape of the electron bunch. This electric field $E_r = \frac{Z_0 c_0 Q}{2\pi r}\lambda(z)$ induces birefringence in a non linear Electro Optical (*EO*) crystal which is located in the vicinity of the electron beam. The crystal display birefringence when an electromagnetic field is present (Pockels-effect). The field of the electron is sampled with a (Ti:Sa) laser with 25 fs duration which is focused on the crystal. By scanning the phase of the laser relative to the electron bunch, the longitudinal profile of the electron can be determined. Using this method the bunch profile is determined with resolution better than 100 fs [SC+05]. The synchronization of the laser pulse and the accelerator RF has been achieved within $(50\text{-}60\,\text{fs})_{rms}$ [LAF+08].

3.5 Synchronization system

At FLASH the electric field used for the acceleration can be employed for pulses up to 800 μs length. Thus with spacing of 1 μs, up to 800 bunches can be accelerated, a beam format which is called a bunch train and is shown in Fig. 3.2. Within a bunch train, the repetition rate of the electron bunches is therefore 1 MHz while the FLASH RF pulse repetition rate is 10 Hz.

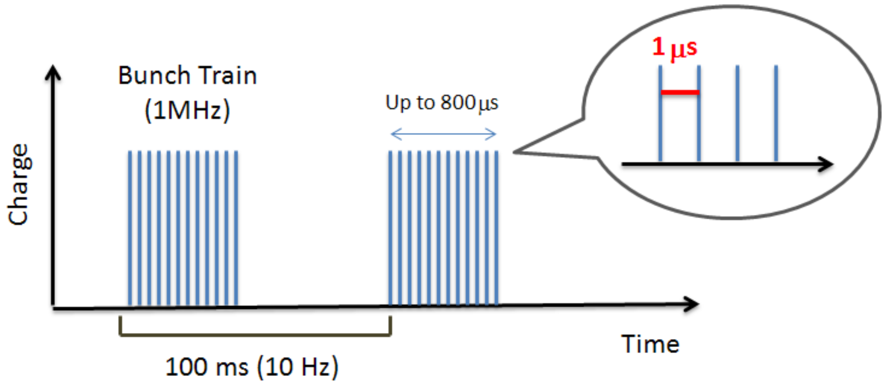

Figure 3.2: *The FLASH pulse temporal structure with 10 Hz repetition rate. Each bunch train can carry up to 800 bunches with minimum spacing of 1 µs.*

RF and optical synchronization have been implanted in the FLASH machine. The purpose of the timing system is to trigger different devices of the accelerator on certain events. These devices are typically gun, kickers, klystrons, data acquisition modules, external lasers for the pump probe and seeding experiments, etc, which all need to be synchronized with the RF. In addition, one of the most challenging task for the operation of the high-gain FELs is the control and arrival time stability of the electron bunch at the entrance of the undulator. The sources of the electron bunch arrival time jitter are the phase and amplitude variations of the photo-cathod laser, the RF gun and superconducting accelerating modules. The large compression factor required to achieve the peak current in order of kA causes large arrival time jitter due to a small energy chirp. Therefore at FLASH facility conventional RF and optical synchronization was implemented for successful operation of the FEL. The reliable performance of the synchronization system is the main step before realizing the seeding experiment. The layout of the synchronization system installed at FLASH is shown in Fig. 3.3.

The Bunch Arrival time Monitors (BAMs) are installed in 4 stations of the machine. The (BAMs) are used to determine the arrival time of the electron bunch relative to the optical timing reference [BFG+10]. The BAM key component is based on the commercials Mach-Zehnder type Electro-Optical-Modulator (EOM). In this regard four button-type electrodes are mounted around the vacuum chamber to pick up the signal. The opposing electrodes cancel the effect of the electron beam position on its arrival time [HSL07]. The traversing electron bunch induces a voltage in the beam pickups which is transferred into a laser amplitude modulation. This modulation is measured with photo-detectors and

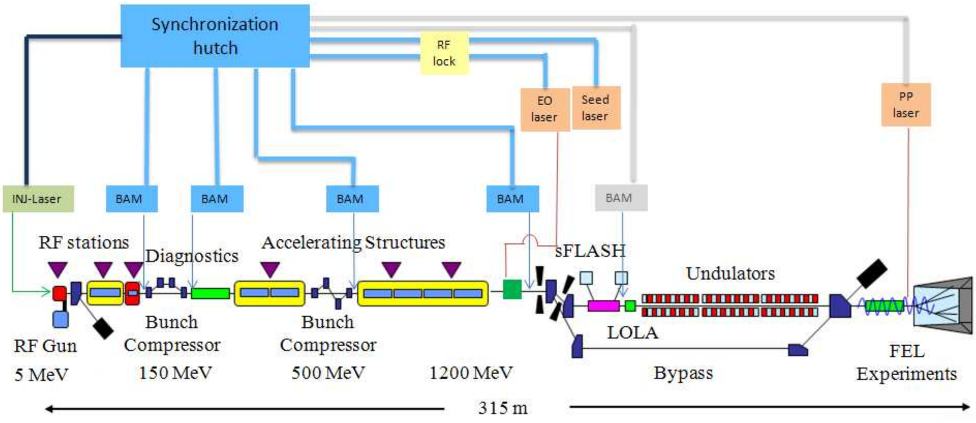

Figure 3.3: *The laser based synchronization system installed in FLASH tunnel. The bunch arrival time monitors (BAMs) which are installed in four stations are used to determine the arrival time of the electron bunch relative to the optical timing reference [SBP+11].*

sampled by a fast ADC. The reference optical laser is adjusted such that it samples the pickup signal at its zero crossing.

By use of the beam based feedback the stability of the electron bunch arrival time for 100 bunches is shown in Fig. 3.4; the measured stability of the electron bunches is within $(25\,fs)_{rms}$. Without feedback the arrival time jitter is approximately (50-70) fs.

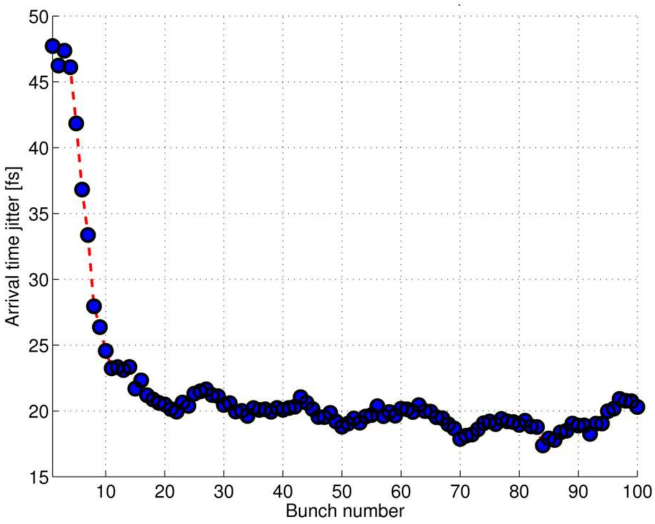

Figure 3.4: *The Arrival time jitter of the electron bunches as determined by the BAM, using beam based feedback. The measured stability is better than* $(25\,fs)_{rms}$. *Without feedback, the arrival time jitter is approximately 50 fs. Due to latency of the feedback system, a couple of bunches in the train is required to reduce the jitter. The bunch distance is about 1μs, taken from [SBP+11].*

Due to latency of the feedback system a couple of bunches in the train is required to reduce the jitter. The bunch distance is $1\mu\,\mathrm{s}$. The arrival time stability of the electron bunch is limited by path length changes in the magnetic chicanes used for bunch compression. For the FLASH machine, an electron beam timing jitter of 60 fs translates into tight tolerances on the amplitude and phase stability of the RF in the most critical accelerating cavities of 10^{-4} and 0.03°, respectively [SgK+07].

4 Experimental layout of XUV FLASH seeding experiment

As discussed in Chapter 2, the high-order harmonic generation (HHG) approach can be used as a source of coherent short-wavelength radiation. Using this radiation as a seed pulse, the longitudinal coherence of the FEL output can be improved by removing the random spikes both in the temporal profile and frequency domain spectra of SASE radiation. Putting this principle into practical application, a seeding experiment has been conducted at FLASH (sFLASH) in order to improve the following aspects:

- High brightness and peak flux;
- Temporal coherence of the FEL output pulse;
- Improve the synchronization in pump-probe performance;
- Reduction of the undulator saturation length.

Fig. 4.1 shows the configuration of the seeding experiment, which has been installed at FLASH during the shutdown of 2009. The XUV pulse ($\lambda_s = 38\,\mathrm{nm}$) is generated with the HHG process, which is a nonlinear interaction of a high power Near-Infrared (NIR) laser field ($\lambda_L = 800\,\mathrm{nm}$) with Argon (Ar) gas. The XUV beam is transported into the FLASH tunnel using grazing incidence mirrors. The XUV beam can be focused at different points along the undulator, using different focusing multilayer mirrors (f =6.25 m; 7 m; 8.5 m) which are remotely exchangeable.

The interaction of the electron bunch and the seed pulse within a 10 m long undulator section produces coherent radiation, which can be detected with a spectrometer in the out-coupling beamline. The pre-requisite condition for the seeding experiment is the six-dimensional phase space overlap, (x, y, x', y', E, and t) between the seed pulse and the electron bunch. To this end, the longitudinal overlap setup is installed upstream the seeding undulator. The transverse overlap diagnostics are installed at different positions along the beamline and within the undulators. The XUV spectrometer installed at the extraction beamline is used for the spectral overlap between the seed pulse and the SASE radiation generated in the seeding undulator. The operation principle and the first results are discussed in detail in this chapter.

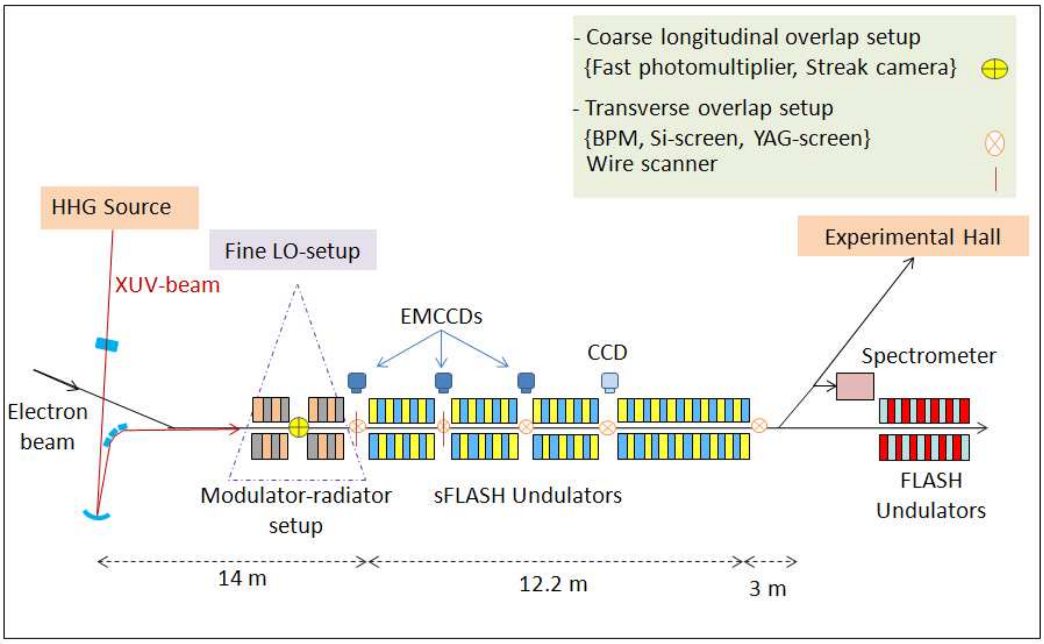

Figure 4.1: *Schematic layout of the sFLASH section: The grazing-incidence mirrors are used to transport the generated XUV pulse (38 nm) to the electron beamline. A focusing multilayer mirror is focusing the beam within the first undulator. This focusing mirror is remotely exchangeable between different focal lengths ($f = 6.25\,\mathrm{m}; 7\,\mathrm{m};$ and $8.5\,\mathrm{m}$). The XUV and sFLASH FEL and SASE pulses can be resolved in the spectrometer. The setup for the coarse and fine temporal overlap and other diagnostics for the transverse overlap are also shown.*

4.1 Seed drive laser

The 21st harmonic (H21) of a Titanium:Sapphire (Ti:Sa) laser is used as a seed pulse in the sFLASH experiment. The seed pulse is generated by focusing the NIR laser into an *Ar* gas target. The drive laser system is based on Chirped Pulse Amplification (CPA) of a Ti:Sapphire laser operating at a repetition rate of 10 Hz. Its central wavelength was measured to be approximately $\lambda_L = 800\,\mathrm{nm}$, and the root-mean-square (rms) pulse duration is $\sigma_{zL} = (14.06 \pm 0.08)\,\mathrm{fs}$. In CPA technique the ultrashort laser pulse is stretched out in time prior to the gain medium using a pair of gratings. Then the stretched pulse, whose intensity is sufficiently low compared with the intensity limit of gigawatts per square centimeter, is safely introduced to the gain medium and amplified. Finally, the amplified laser pulse is re-compressed back to the original pulse width through the reversal process of stretching, achieving orders of magnitude higher peak power than laser systems could generate before the invention of CPA [SM85]. The schematic layout for the seed drive laser is shown in Fig. 4.2.

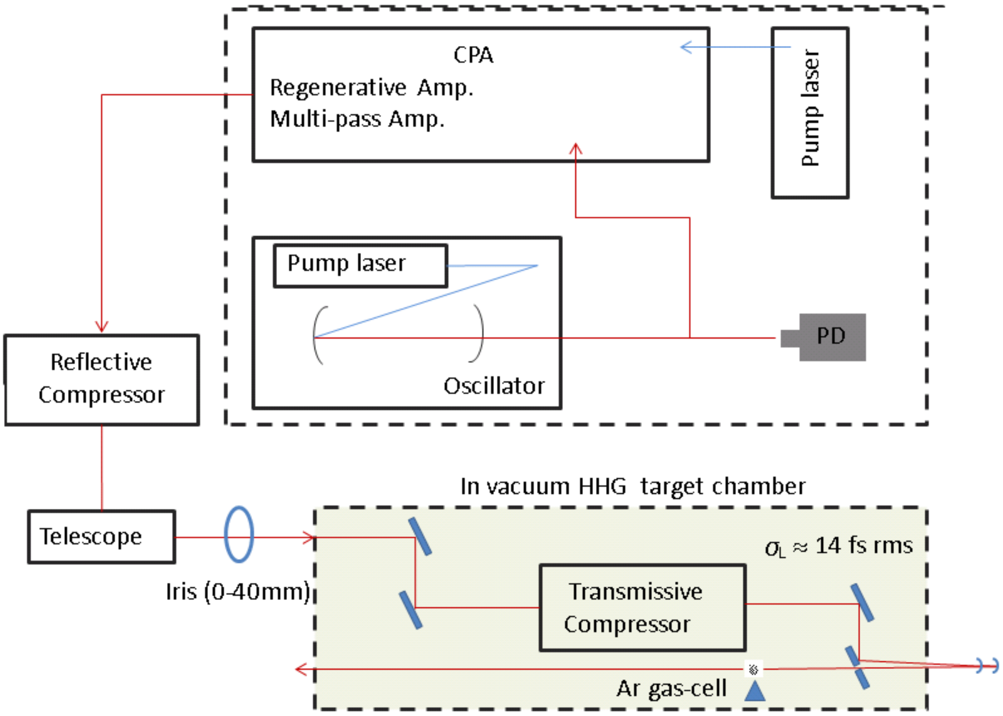

Figure 4.2: *Seed drive laser layout. The ultra short laser pulses (λ=800 nm) are generated based on CPA technique. The reflective and transmissive compressors are used to generate ultra short laser pulses with σ_{zL}=14 fs duration. Using an iris, the optimum laser pulse intensity is coupled into the gas cell.*

The initial component of the laser system is a mode locked oscillator, and is synchronized to a 81 MHz master oscillator with an electronic feedback loop, followed by a regenerative amplifier and a compression system. The laser pulse compression takes place in two steps. The laser pulse is compressed down to few hundreds of femtoseconds, by means of a reflective compressor in air and then it is compressed down to $(14\,\text{fs})_{rms}$ by the transmissive compressor which is placed in vacuum to avoid breakdown. The first compressor is placed a few meters before the HHG chamber and the second one is located in vacuum within the HHG chamber. The reason for using two compressors is the tendency of a femtosecond laser pulse to break up into filamentary structures due to self-phase modulation as it passes through different optical material. The filamentation occurs due to the growth of small perturbations in the laser wavefront [BT66].

4.1.1 Synchronization with master oscillator

In order to synchronize the HHG drive laser, part of the NIR laser oscillator is sent to a fast photodiode for the synchronization to the laser with the electron bunch, see Fig. 4.3. The photodiode signal is filtered and sent back to a Phase Locked Loop (PLL) circuit. This feedback system controls the phase of the laser oscillator relative to the RF signal of the FLASH Master Oscillator (MO), by changing the cavity length. The signal of the photodiode is coupled to a mixer together with the MO signal. The product of both signals, which are sent to the mixer are described as follows:

$$\sin(\omega_L t + \phi_L) \cdot \sin(\omega_{RF} t + \phi_{RF}) = \frac{\cos[(\omega_L + \omega_{RF})t + (\phi_L + \phi_{RF})]}{2} - \frac{\cos[(\Delta\omega)t + \Delta\phi]}{2},$$

where $\Delta\omega = \omega_L - \omega_{RF}$ and $\Delta\phi = \phi_L - \phi_{RF}$ are the frequency difference and the phase difference between the seed laser oscillator signal (index L) and RF signal of master oscillator (index RF), respectively. The RF low pass filter blocks the fast frequency components $(\omega_L + \omega_{RF})$. The output voltage of the mixer is thus proportional to the phase difference between the two input pulses. A proportional-integral-derivative (PID) controller compensates the phase difference by changing the phase of the laser relative to the MO signal .

A vector modulator is used to manually adjust the timing of the laser relative to the RF signal. The vector modulator is in principle a phase shifter which controls the phase of the signal via analog or digital commands [VM10]. The minimum jitter of the NIR laser relative to the RF is measured to be about $(65\,\text{fs})_{rms}$. The relative jitter of the electron bunch and the RF signal of the MO is also varied from $(65\,\text{fs})_{rms}$ to $(200\,\text{fs})_{rms}$ with the feedback on, depending on the operation mode of the machine [BFG+10].

4.2 HHG source Characterization

Maximum conversion efficiency can be obtained by optimizing the laser intensity, gas pressure, and position of the gas jet relative to the laser focus, as was explained in Chapter 2. The energy of the NIR laser after the second compression is E_L=22 mJ. The laser intensity is optimized by an iris and focused into the pulsed gas-cell, as shown in Fig. 4.4.

Different schemes are designed and constructed to focus the NIR laser into the gas cell with the focal lengths of f_L=1.5 m, 2.5 m, 3 m, 3.5 m, 5 m, and 7 m. For the case of f_L=3 m it was observed that the maximum HHG yield occurs when the gas cell is placed 60 mm before the focal point of the laser [Mit11]. The experiment showed that the HHG

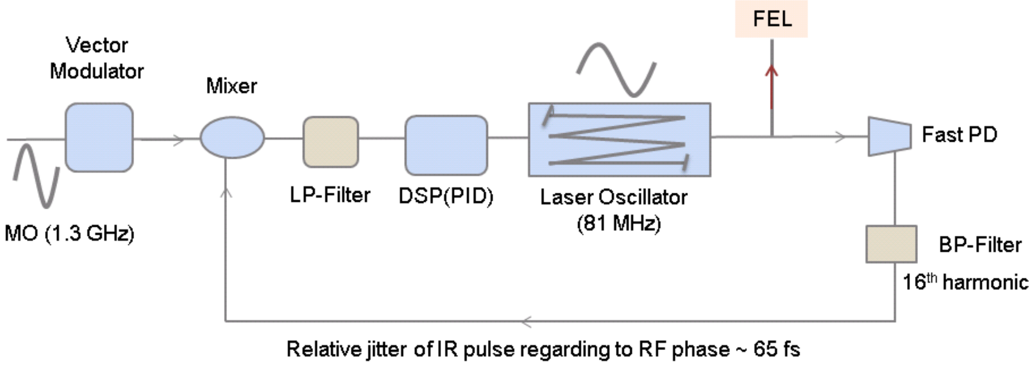

Figure 4.3: *Synchronization layout of the NIR laser oscillator with MO. A part of the NIR laser oscillator signal (81 MHz) is sent to the fast photodiode. A bandpass filter selects the 16th harmonic. This signal together with the RF master oscillator (1.3 GHz) are mixed together. The fast frequency components are blocked using a low-pass filter. The PID controller compensates the phase difference between the two incoming signals. The vector modulator can be used to change the relative phase of the laser pulse with respect to the MO manually.*

yield is maximized when the gas jet is placed in the converging part of the laser beam. Accordingly the laser pulse with the optimum energy and focal length is focused into the gas cell in the HHG target chamber. The current length of the gas cell is 50 mm.

The residual gas density which exist in the second HHG chamber (10^{-5} Torr) is used to measure the energy of the generated HHG pulse using a High-order Harmonic meter (HH-meter). The generated HHG pulse is directed either to the adjacent FLASH tunnel or, using two pairs of triplet mirrors, to the diagnostic station in the lab. The diagnostic station is equipped with a Hartmann wavefront sensor, XUV-spectrometer and a XUV-CCD camera. The spectra of the HHG radiation measured with the spectrometer in the lab is shown in Fig. 4.5.

An aluminum filter is placed in the beamline. Excluding the contribution of oxide layer, this filter has about 40% transmission for the 11th harmonic, zero transmission for the lower orders, and approximately 60% transmission for the higher order harmonics. The minimum estimated energy of the 21st harmonic E_{H21} was measured with different diagnostics, see Table 4.1. The energy and photon-number plateaus provide a lower and an upper limit for the energy of the 21st harmonic. The error of each individual measurement is also calculated in terms of error propagation. The big uncertainty in the HHG-meter measurement is mainly due to shot-to-shot harmonic fluctuations. For more information the reader is directed to Ref. [Mit11]. The energy stability of the HHG pulse is measured to be about $\sigma_{H21} = 25\%$. The divergence of the HHG pulse is measured in the laser laboratory using an XUV-CCD camera. The plane and focusing multilayer mirrors which

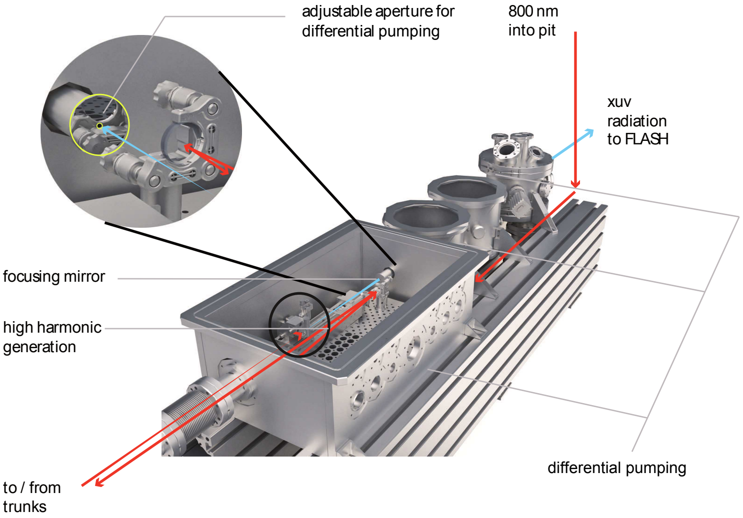

Figure 4.4: *HHG setup used for sFLASH: The NIR laser (red arrow) is sent to the target chamber containing the pulsed gas nozzle. The channel is filled with Ar gas at a repetition rate of 10 Hz. Different schemes can be used for focusing of the NIR laser into the gas channel. The HHG beam is directly transferred to the adjacent FLASH tunnel. Alternatively, the XUV beam can be directed to the diagnostic station using two pairs of triple mirrors, taken from Ref [Mit11].*

were installed in the transport beamline, were used to image the far field and near field of the H21. The elliptical shape of the HHG pulse determines two divergences relative to the wide and narrow axis of the ellipse as indicated in Table 4.2.

Diagnostic	with energy plateau	with photon-number plateau
CCD camera	$E_{H21} \geq (0.23 \pm 0.03)\,\mathrm{nJ}$	-
HH-meter	$E_{H21} \geq (0.5 \pm 0.1)\,\mathrm{nJ}$	$E_{H21} \geq (14.9 \pm 2.2)\,\mathrm{nJ}$
XUV-Photodiode	$E_{H21} \geq (1.4 \pm 0.4)\,\mathrm{nJ}$	$E_{H21} \geq (2.4 \pm 1.2)\,\mathrm{nJ}$

Table 4.1: *The energy of the generated XUV pulse with and without assumption of the plateau [Mit11].*

f =1.5 m	$f = 3$ m
$\theta_{narrow} \leq (0.34 \pm 0.01)\,\mathrm{mrad}$	$\theta_{narrow} \leq (0.56 \pm 0.01)\,\mathrm{mrad}$
$\theta_{wide} \leq (0.78 \pm 0.01)\,\mathrm{mrad}$	$\theta_{wide} \leq (0.84 \pm 0.03)\,\mathrm{mrad}$

Table 4.2: *HHG divergence for different focusing mirrors [Mit11].*

The energy of the NIR laser is measured to be (22.1±1.3) mJ for the iris diameter of 24 mm, for the f=3 m case. The energy stability of the NIR laser is measured to be

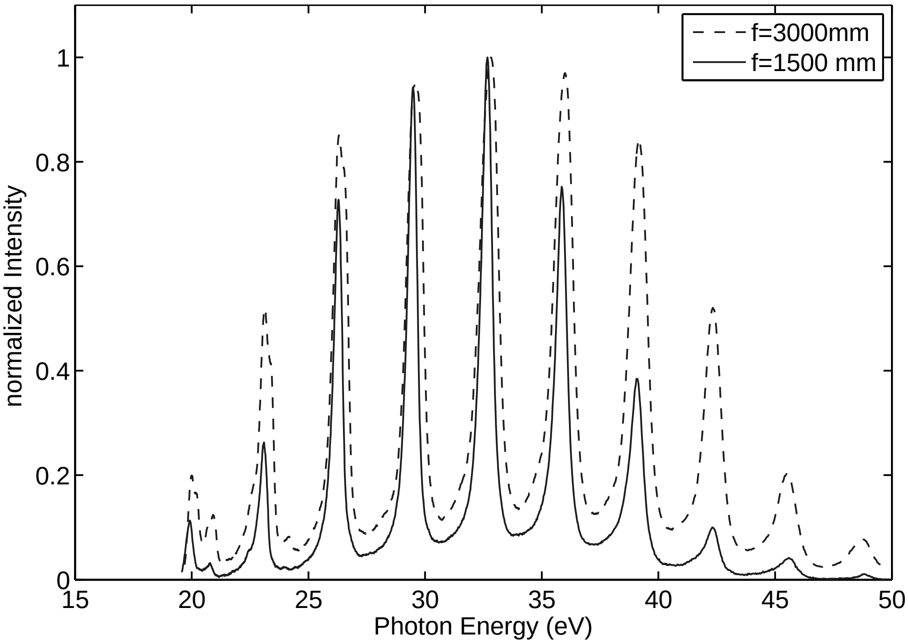

Figure 4.5: *Spectrum of higher-order harmonics generated in Ar gas by two different NIR focusing mirrors, adapted from Ref. [Mit11].*

better than 5% rms. To measure the laser beam quality a CCD camera was placed at the position of the gas-cell. After scanning 20 points over 250 mm around the laser focus, the M^2, beam waist and the Rayleigh length were calculated, as given in Table 4.3:

Parameter	Value (f=1.5 m)	Value (f=3 m)
M_x^2	1.11±0.05	1.12±0.02
w_{0x}(μm)	107 ±4	173±2
z_{Rx} (mm)	41 ±5	105 ±4
M_y^2	1.62±0.08	1.87±0.05
w_{0y}(μm)	97 ±6	186 ±4
z_{Ry} (mm)	23 ±4	75 ±5
θ_{Lx}(mrad)	(2.64±0.05)	(1.65±0.02)
θ_{Ly}(mrad)	(4.25±0.08)	(2.56±0.05)

Table 4.3: *HHG drive laser parameters, [Mit11].*

4.3 Transport beamline

The HHG radiation is coupled to the electron beamline by using four grazing incidence mirrors (1"). Half of the mirror substrate is coated with TiB_4C for 38 nm and the other half is coated with the MoB_4C for 13 nm. The first plane mirror reflects the beam upwards at an incident angle of 13.9 ° to a spherical multilayer mirror nearly at normal incidence. Afterwards, the next three mirrors bend the HHG radiation by a total angle of 84 ° [Böd11]. A schematic layout for the transport beamline is shown in Fig. 4.6.

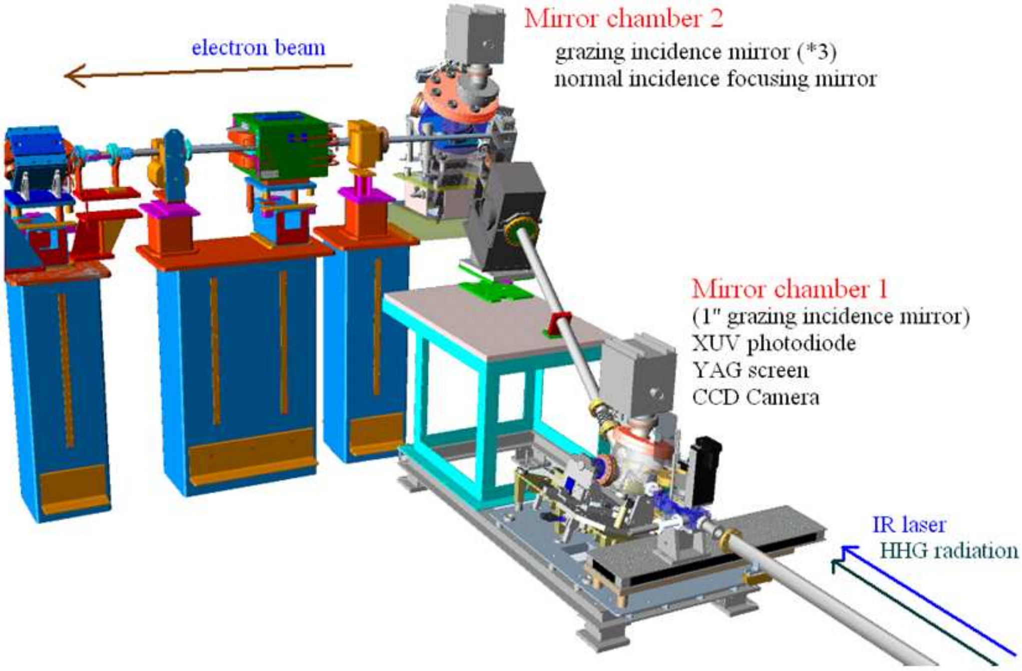

Figure 4.6: *HHG transport beamline. The NIR laser and HHG beams are directed from the laser lab to the adjacent FLASH tunnel using two mirror chambers. The first chamber contains a grazing incidence mirror and sends the beam upwards, to the same height of the electron beamline. In this chamber a CCD camera, an XUV photodiode, and a YAG screen are installed for beam characterization. Three other grazing incidence mirrors in the second chamber bend the beam by a total angle of 84°. The focusing mirror station in this chamber is also remotely adjustable in order to change between different focal lengths, f =6.25 m, 7 m, and 8.5 m [Böd11].*

The focusing of the HHG beam within the undulator can be performed by using different normal incidence focusing mirrors. The focusing mirrors are coated with multi-layer coatings of ($Sc/Si{+}B_4C$) and ($Mo/Si{+}B_4C$) to focus radiation at the wavelengths of 38 nm and 13 nm, respectively. The overall transmission of the beamline at 38 nm is estimated to be 20% [B$^+$10]. In addition to the XUV mirrors a dielectric coating mirror, which is optimized for the wavelength of $\lambda = 800$ nm, is installed to focus the NIR laser at the beginning of the modulator-radiator setup for the synchronization purposes. The focal length of this mirror is $f = 5$ m.

4.4 Undulator section and photon beamline

The FEL component of sFLASH consists of a 10 m long variable-gap undulator, with three 2 m long undulators (Type U32), followed by a 4 m long undulator, (Type U33) [DHMR+09]. In Table 4.4 the relevant undulator parameters are listed. Phase shifters and moveable quadrupoles are installed between undulators to correct the phase advance of the electron bunch relative to the seed pulse as well as the transverse focusing of the electron beam. The undulator intersections are 70 cm long and are equipped with different diagnostics to characterize the spatial beam properties.

	U32	U33
Min gap	9.0 mm	9.0 mm
Period length λ_u	31.4 mm	33 mm
K_{max}	2.72	3.03
Number of poles	120	240

Table 4.4: *Parameters of the seeding undulators.*

The seeding undulators deflect the electron bunch in the horizontal plane and therefore the horizontal electric-field component of the HHG pulse would interact with the electrons. At the source the NIR pulse as well as HHG pulse are 99.8% horizontally polarized. Due to geometry of the transport beamline the polarization of the beam would change slightly. That means, for the fully horizontally-polarized HHG pulse at the source, electric field components parallel (E_x) and perpendicular (E_y) to the deflection plane of the undulator would be about 45% and 15% of the input field at the source, respectively. For the fully-horizontally polarized beam at the source, the transmission of the beamline at 38 nm is estimated to be 20% [Böd11].

After the undulator section a magnetic chicane separates the electron bunch from the seed pulse vertically. The XUV and undulator radiations are directed into a XUV spectrometer using grazing incidence mirrors, see Fig. 4.7. The carbon-coated Si plane mirrors are used to reflect the beams. The reflectivity at a grazing angle of 5 ° is larger than 85 % [SJ+04]. The photon beamline continues with the first diagnostic chamber which is equipped with a YAG screen and an alignment paddle. Following that, the switching mirror chamber sends the radiation either to the diagnostics branch, which includes the XUV spectrometer and the intensity monitors, or into the experimental hutch, where time resolved pump-probe studies can be performed [CAB+09].

To measure the gain of the seeded radiation, three Multi Channel Plates (MCPs) are installed in the diagnostics branch. The scattered radiation from a gold mesh is directed to the MCPs in different geometrical position. The spectrometer with gold-coated grating and 3 ° of incidence, is capable of measuring a single shot spectrum. The slit size of the spectrometer is adjustable from 5 μm to 500 μm. The measured resolution of the spectrometer is $\delta\lambda/\lambda = 600$ [Cur11].

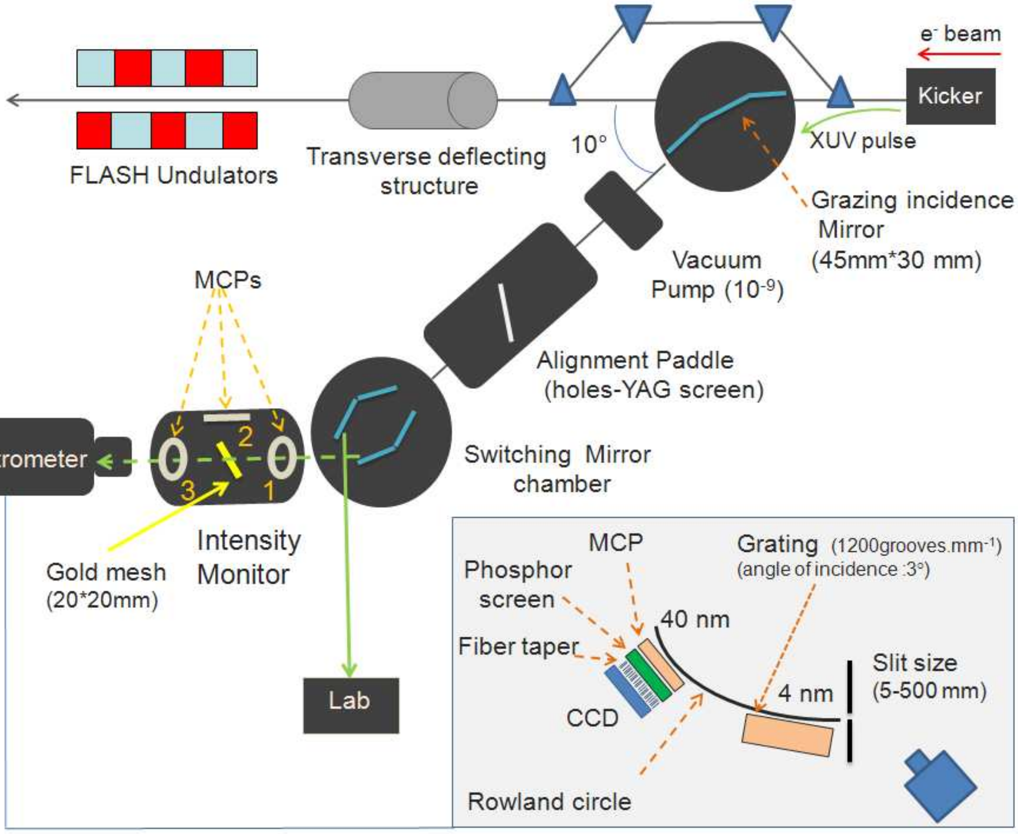

Figure 4.7: *Schematic of the extraction beamline: The FEL and HHG radiation coming from the right are deflected with the first mirror-chamber and then pass through the diagnostics block. The second mirror-chamber deflects the radiations either to the laser hutch for time-resolved experiments or to the diagnostics branch which includes a spectrometer and MCPs. The gold coated grating of the spectrometer is placed behind the slit, see figure down right. The MCP is tangent to the Rowland circle. Data readout is done with a CCD which is connected with a fiber tapers to the phosphor screen. The MCP-phosphor assembly can be placed at any position along the Rowland circle to detect the wavelengths from 4 nm to 40 nm. The measured resolution of the spectrometer is* $\delta\lambda/\lambda = 600$

.

The mentioned-above spectrometer was used for finding the spectral overlap between HHG and sFLASH SASE radiations. In addition, it was used to demonstrate the enhanced seeded signal and to compare it to the background SASE radiation, upon fully six dimensional overlap between HHG pulses and electron bunch which is explained in the following section.

4.5 Six-dimensional overlap of phase-space distribution

For achieving the seeding, sufficiently accurate spectral, transverse, and longitudinal overlap between the HHG radiation and the electron bunch at the entrance of the seeding undulator is required. To achieve that, the orbit of the electron bunch with beam energy of $E_e = 700\,\mathrm{MeV}$ was tuned along the entire length of the machine in order to establish the SASE signal with energy of ($\geq 50\,\mu$J) from the FLASH FEL undulators. After dispersion compensation the SASE spectrum was recorded to redetermine the electron beam energy. Thereafter, the TDS was used to measure the longitudinal distribution of the electron bunch. Literally for achieving the temporal overlap between HHG pulse and the electron bunch, the duration of the electron bunch should be longer than its longitudinal jitter relative to the HHG pulse. As the next step, the seeding undulators were closed to the correct gap and the electron beam was steered around the extraction mirror, which is located downstream of the seeding undulators. The further tuning has been done to re-correct the orbit of the electron bunch and to reduce the losses. After the tuning process, the six-dimensional phase space overlap was achieved by employing the following steps.

4.5.1 Transverse overlap

According to the tolerance studies for the seeding experiment at FLASH, the angular and transverse deviation of the seed pulse and the electron bunch along the undulator should be suppressed within $35\,\mu$m and $20\,\mu$rad, respectively [MAB$^+$08].

Therefore four diagnostic stations for the transverse overlap are installed before each of the seeding undulators, see Fig. 4.1. Each of the stations is equipped with a Beam Position Monitor (BPM), an Optical Transition Radiation (OTR) Si-screen to map the electron bunch profile, and a YAG screen for monitoring the HHG radiation profile. The first three stations are provided with electron-multiplying CCD (EMCCD) cameras to improve the imaging of the low intensity HHG radiation. Wire scanners have been installed in the first two diagnostics stations and they were used to benchmark the measurements with the screens.

The alignment laser (λ=500 nm) which is installed in the tunnel and the NIR laser were used for the pre-alignment. Afterwards, the HHG radiation was propagated to the spectrometer in the extraction beamline. The transverse alignment between the two beams was done with remotely accessible motorized mirrors in the transport beamline.

The measured horizontal and vertical waist sizes of the HHG radiation within the first seeding undulator are w_{0x} =(0.409±0.098) mm and w_{0y} =(0.651±0.187) mm respectively, for the case of f =6.25 m [Böd11].

The transverse overlap between the seed pulse and electron bunch was achieved with the accuracy about 50 μm and 50 μrad [Böd11].

4.5.2 Spectral overlap

After transverse overlap of the HHG radiation with the electron bunch inside the undulators, the spectrum of the HHG radiation was recorded using the XUV spectrometer. To maintain the spectral overlap two approaches were followed:

- Tuning each undulators individually in order to overlap the spectrum of spontaneous radiation with the HHG spectrum;
- Closing all four undulator gaps based on previously done magnetic calibration.

Because of the large distance between the first undulator and extraction mirror and weak intensity of the undulator radiation, an aperture could not be used to limit the bandwidth of the radiation. Therefore, for the first case, the accuracy of the measurement would decrease due to contribution of the off-axis undulator radiation [AAB$^+$11]. For the latter case, the gaps of all four undulators were adjusted simultaneously using the calibration curve till the sFLASH-SASE was achieved. The orbit was corrected in order to have just the on-axis radiation in the spectrometer. Using the same calibration curve, the wavelength of the observed SASE radiation in the spectrometer was moved toward the wavelength of the H21. In Fig. 4.8, the single shot SASE-FEL spectrum and the average spectrum over 2000 shots are shown. For comparison the measured spectrum of the HHG radiation is shown in Fig. 4.9.

The actual resolution of the spectrometer is $\lambda/\Delta\lambda = 600$, this means that at 38 nm one can resolve approximately 0.063 nm. The measured spectral bandwidth of SASE-FEL radiation and HHG radiation are compared in Table 4.5.

The bandwidth of SASE-FEL radiation can be estimated analytically using Eq. 2.9. For the electron energy of E_e =700 MeV, σ_r =60 μm and λ_r =38.6 nm , the gain length, the FEL parameter and the bandwidth at saturation are L_g =0.42 m, $\rho = \frac{\Delta\lambda}{\lambda} = 3.6 \times 10^{-3}$ and $\Delta\lambda \sim 0.14$ nm, respectively. According to Fig. 2.3 the SASE-FEL bandwidth before

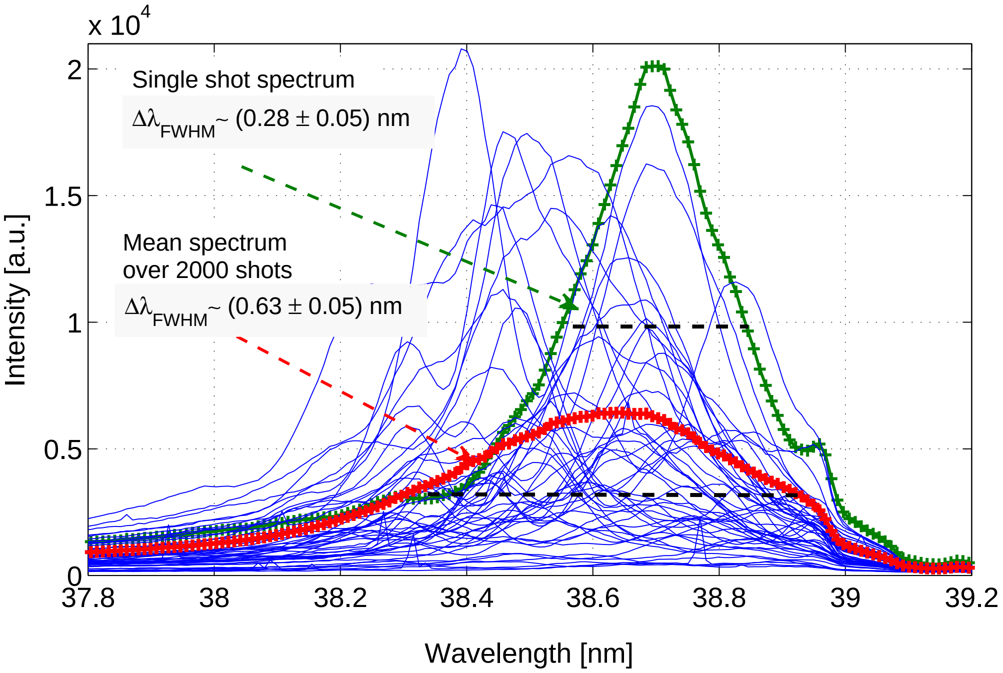

Figure 4.8: *Several single shot SASE-FEL spectrum measured with the spectrometer in the extraction beamline. The red curve shows the average over 2000 single shots.*

saturation is estimated to be $\delta\lambda = \frac{\lambda_r}{N}(\rho N)^{1/2} = 0.13\,\mathrm{nm}$, where N =312 is the total number of undulator-periods.

The comparison between the measured SASE-FEL bandwidth with the result of analytical estimation shows that the FEL did not enter the saturation regime. Even in this regime the bandwidth of SASE-FEL and HHG radiation is comparable, therefore narrowing of the seeded signal in the XUV-spectrometer will be hardly detectable.

	$(\Delta\lambda\,(\mathrm{nm}))_{FWHM}$	$\frac{\Delta\lambda}{\lambda}$
SASE-FEL (single shot)	0.28±0.05	$(7.2\pm0.5)\times10^{-3}$
SASE-FEL (Mean spectrum)	0.62±0.05	$(16.1\pm0.5)\ \times10^{-3}$
HHG-radiation (single shot)	0.2±0.1	$(5\pm2)\ \times10^{-3}$

Table 4.5: *Spectral bandwidth of the SASE FEL in comparison with the HHG radiation, estimated from the measurement.*

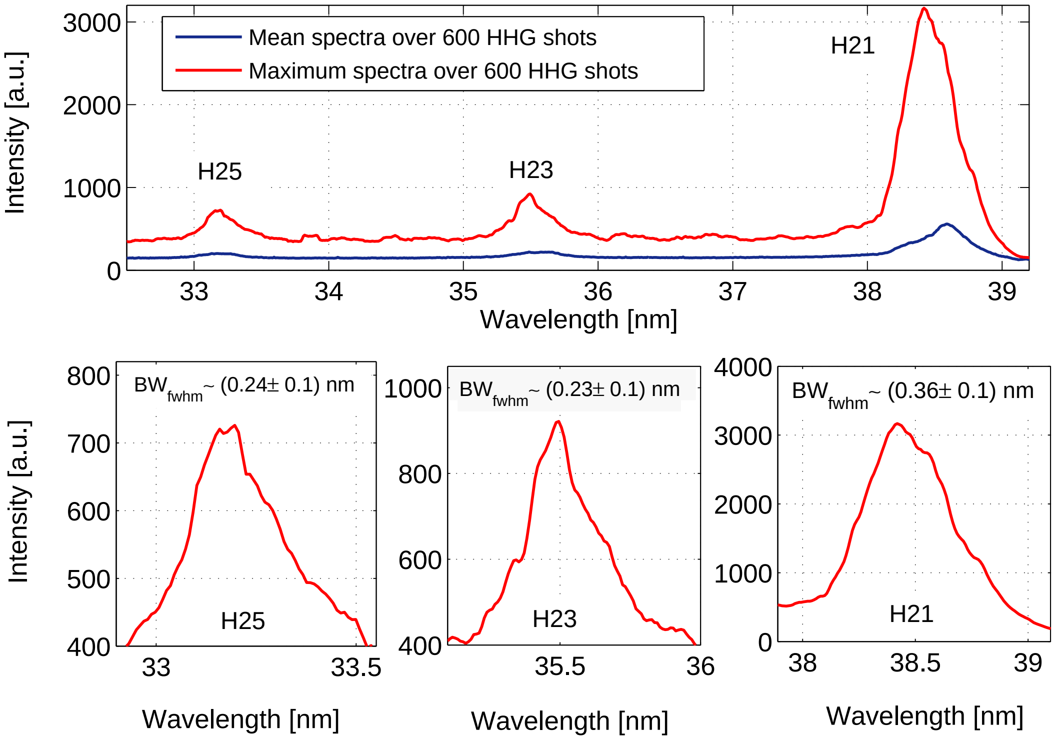

Figure 4.9: *The bandwidth of HHG radiation spectrum detected at the spectrometer after the seeding undulators.*

4.5.3 Longitudinal overlap

One of the crucial tasks for seeding is finding the longitudinal overlap between the seed pulse ($\sigma_s \simeq 8.5\,\mathrm{fs}$) and the lasing part of the electron bunch distribution ($\sigma_l < 100\,\mathrm{fs}$).

Two techniques are employed to achieve the temporal overlap at sFLASH. Firstly, a streak camera based approach measures the arrival times of the NIR laser pulse and the electron bunch (using spontaneous undulator radiation) with sub-picosecond resolution. The spontaneous radiation is taken from the first undulator of ORS experiment (5 periods, 200 cm periodic length, 1 m total length) which carries information about the arrival time of the electron bunch [SSS07] .

Secondly, for a finer resolution, a modulator-radiator based system is used in which the laser imprints an energy modulation onto the electron bunch within the modulator section. The energy modulated beam passes through a dispersive section, where the energy modulation converts to a density modulation. In case of overlap between the external seed laser and the electron bunch, coherent light will be produced in the radiator, a process similar to that occurring in an optical klystron. The generated coherent light imprints the temporal overlap with femtosecond resolution.

Since this part of the overlap system is the main topic of this thesis, the simulations, tolerance studies, analytical approaches, as well as the construction work, and the experimental results on this subject are discussed in detail in the following chapters.

5 Theoretical investigation on the longitudinal overlap between electron beam and seeding pulse

5.1 Tolerance studies on the longitudinal jitter using GENESIS

As was explained in the previous chapters, one of the major step to do the seeding experiment is finding the longitudinal overlap between the seeding pulse with rms length of $\sigma_s \simeq 8.5\,\mathrm{fs}$ and the electron bunch. The longitudinal distribution of the electron bunch depends on the charge, on the phase and amplitude of the accelerating modules and also on the third harmonic cavity which has been newly installed in the FLASH machine.

Due to the mean longitudinal jitter of electrons ($\sigma_{je} \simeq 70\,fs$) and HHG pulse ($\sigma_{js} \geq 65\,fs$) relative to the RF, an appropriate electron bunch length is desired to overcome the existing uncertainties. In addition further simulation studies are needed, since the lasing part of the electron bunch distribution is not fully known, due to energy spread. The goal of the simulation presented in this section is to show the sensitivity and resolution which is needed for finding the longitudinal overlap between the two pulses. The footprint of the electron bunch characteristics in the final result and the impact of the longitudinal jitter on the overall output is also studied. Following this simulation the statistical analysis is presented which shows the probability of finding the longitudinal overlap in presence of different longitudinal jitters of arrival time for the two pulses.

For this reason in the first step an electron bunch which has been used in one of the commissioning shifts is used as an input file for the simulation together with a normal Gaussian distribution as the seed pulse. As a comparison the longitudinal electron bunch distribution, taken from start-to-end simulation is also used. The advantage of the latter distribution is that the emittance of the electron bunch is also taken into account.

5.1.1 Simulation result using measured electron bunch distribution

Due to random relative jitter between the electron bunch and the seed pulse, in different instances the seed pulse will hit different parts of the electron bunch distribution. The interaction of two pulses in different longitudinal positions along the bunch is simulated using the GENESIS code [Rei99], to demonstrate the impact of this jitter on the output power.

As an input file for this simulation a Gaussian temporal profile is assumed for the seed pulse with $\sigma_s \simeq 8.5\, fs$. Using the Transverse Deflecting RF-Structure (TDS) [Bg11] the electron bunch length, slice energy spread and bunch current were extracted and used as an input for the simulation, see Fig. 5.1.

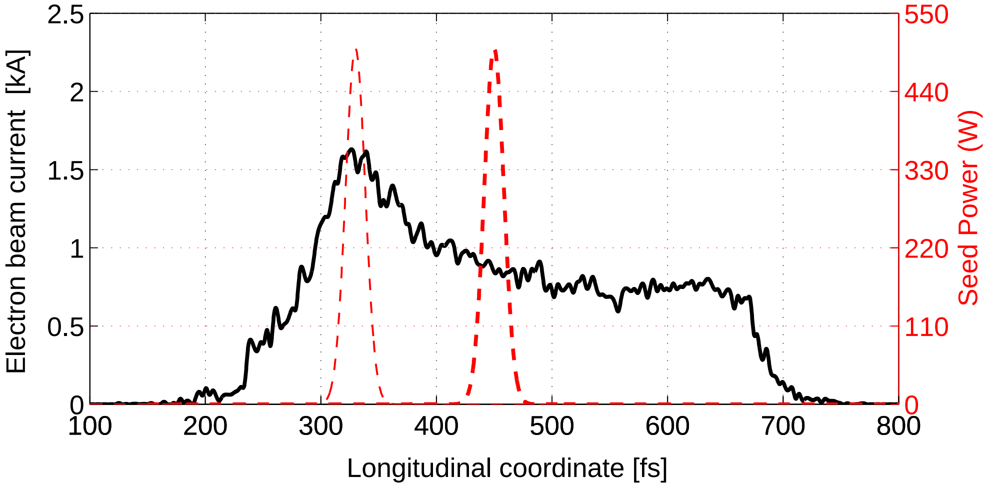

Figure 5.1: *A typical electron bunch distribution taken from the measurement is plotted in black. The seed pulse in red dashed-line is shown in two random positions along the electron bunch with energy of 700 MeV and charge of 400 pC.*

The mean energy of the electron bunch was measured to be E_e =700 MeV with a charge of 400 pC. The simulation examines the FEL performance in the first three undulators, which have a period length of λ_u=3.14 cm and total length of 8.15 m (including intersection areas). Under these conditions, the resonance wavelength of the undulators agreed with the seed wavelength, λ_{res} =38 nm. The Rayleigh length of the seed field was assumed to be z_R =1.55 m (at the waist in the beginning of the undulator, z_{waist} =0). The seed beam waist radius (with M^2 =1) can be computed as [SDR08]:

$$w_0 = \sqrt{\frac{z_R \cdot \lambda_{res}}{\pi}} = 136.9\,\mu\,\mathrm{m}$$

For the electron bunch with defined rms transverse normalized emittances of (ϵ_{nx}=ϵ_{ny} =2 mm-mrad) and beta functions of (β_x=6 m, β_y=7.5 m), the transverse electron beam sizes would be:

$$\sigma_{ex} = \sqrt{\frac{\beta_x \epsilon_n}{\gamma}} = 93.6\,\mu\,\mathrm{m}$$

$$\sigma_{ey} = \sqrt{\frac{\beta_y \epsilon_n}{\gamma}} = 104\,\mu\,\mathrm{m}$$

The energy spread and mean deviation from the mean energy within the bunch are plotted in Fig. 5.2. The coupled seed pulse energy in the beginning of the seeding undulator is estimated to be 10 pJ.

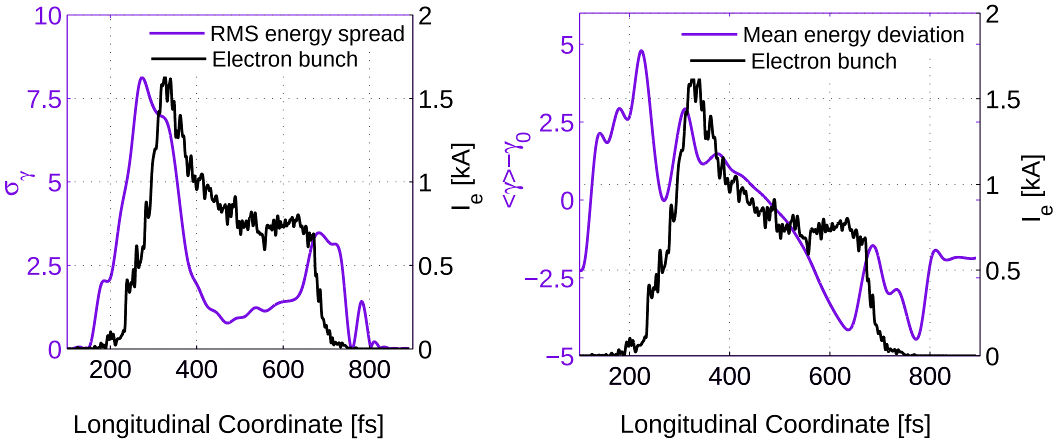

Figure 5.2: *Left: rms energy spread (σ_γ), Right: mean deviation from the mean energy ($< \gamma > -\gamma_0$) taken from the measurement. The graphs show 3.5 MeV energy spread and about 1 MeV energy deviation at the peak of current distribution.*

As is shown in Fig. 5.2 at the point with the peak current ($\sim 300\,fs$) there is a relatively large energy spread σ_E=3.5 MeV and mean deviation about 1 MeV, both of which affect the interaction process between electron bunch and seed pulse. For this reason, the simulation is repeated for different longitudinal positions of the seed pulse along the electron bunch, separated by steps of approximately 33 fs. The effects of relative jitter on the total output power and spectrum is plotted in Fig. 5.3 and Fig. 5.4, respectively. The peak FEL power occurs at the point with the minimum energy spread and mean deviation from mean energy along the bunch (t_s =450 fs) and not at the position of the peak current (t_s =340 fs), see Fig. 5.3. The seeded signal at the exit of the undulator is appeared approximately 17 fs ahead of the initial seed position. The slippage of the 38 nm seed light over 6 m undulator section with total number of periods of $N_u = 191$ is $t_{slippage} = \frac{\lambda_r \times N_u}{c} \sim 24$ fs. The time difference can originate from the contribution of amplified SASE background with the seeded pulse.

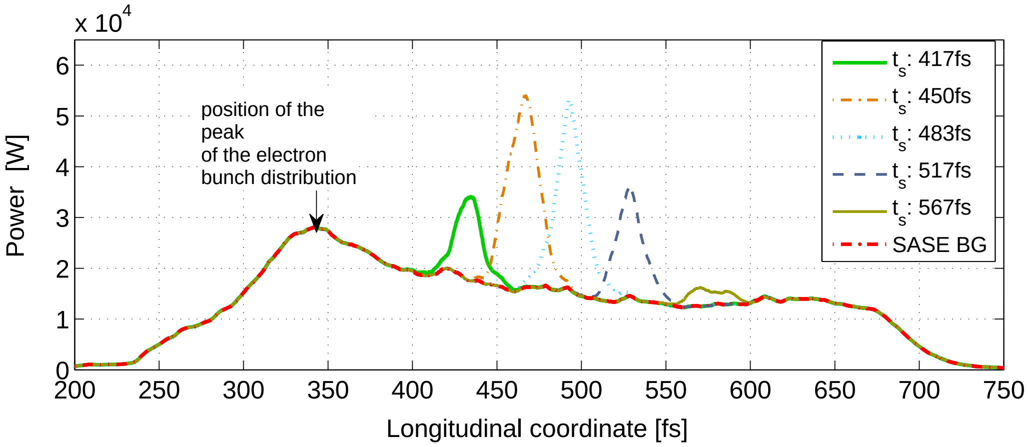

Figure 5.3: *Total power of the seeded radiation pulse as a function of seeding pulse injection time.*

Another aspect of the FEL performance is indicated in Fig. 5.4, in which changes in the spectrum of the seeded signal are considered as a function of seeding pulse injection time.

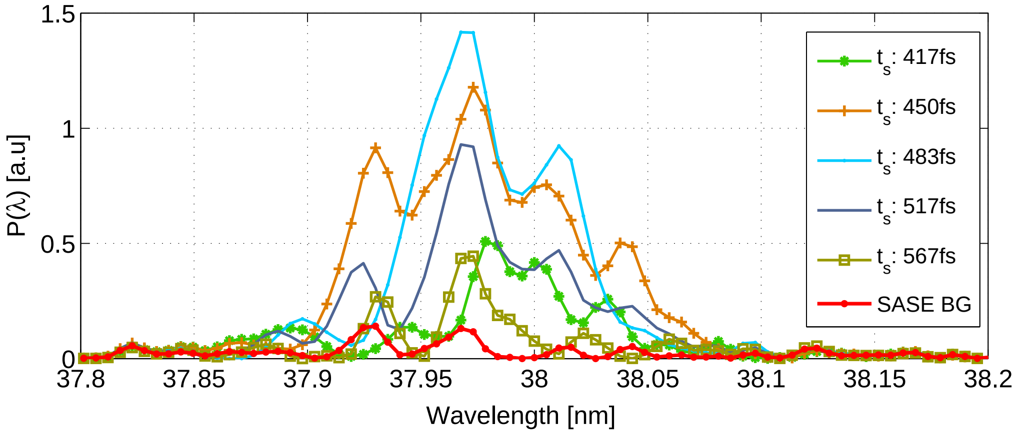

Figure 5.4: *The spectrum of simulated seeded pulses as a function of seeding pulse injection time.*

The energy-contrast for different seeded points along the electron bunch is plotted in green bars in Fig. 5.5. The spectral contrast, which is shown with orange bars in the same figure, is defined as the ratio of the maximum of the seeded pulse spectrum to the maximum of the SASE background, at resonance wavelength within 0.1 nm bandwidth.

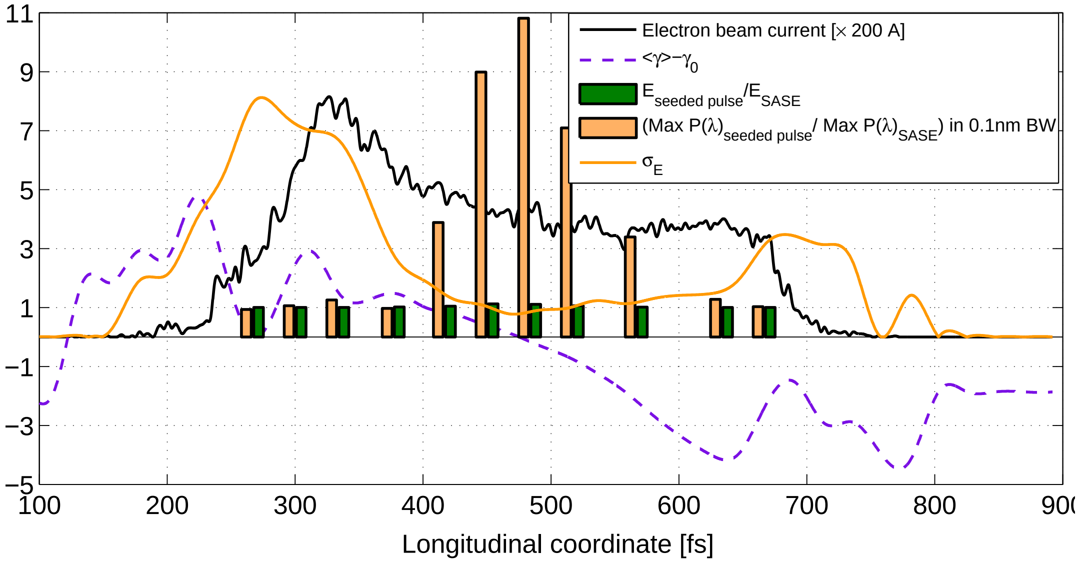

Figure 5.5: *The contrast of seeded pulse and SASE background.*

The electron bunch distribution, energy spread and mean deviation from mean energy are also plotted for comparison. The systematically low contrast is due to the low estimated coupled energy between electron and seed pulse in beginning of the seeding undulator. For the points in which the relative jitter is bigger than 66 fs, the contrast drops drastically. Observing the FEL output with the MCPs installed on the extraction beamline, this contrast maybe hard to observe due to fluctuations in the SASE signal. As was shown in Fig. 2.4, the fluctuation in FEL pulse energy is approximately 32.5%. This result shows that the observable contrast between SASE and seeded pulse (spectrally and also in the power point of view) depends strongly on the electron bunch properties such as energy spread, and also the relative longitudinal jitter between two femtosecond pulses. This gives rise to the need for higher beam arrival time stability, and also implementing a diagnostic method having better than 100 fs resolution for the overlapping process.

5.1.2 Simulation results using an electron bunch taken from start-to-end simulation

In this section, a different approach is discussed to obtaining the electron bunch distribution, in which a phase space distribution is taken from the output of a start-to-end beam dynamic simulation [Zag09]. The electron bunch distribution, energy spread and mean deviation at the exit of the third seeding undulator obtained in this manner are presented in Fig. 5.6. Energy spread along the bunch is less than 1.5 MeV and the mean energy deviation along the bunch varies up to 2.5 MeV in the central part of the bunch. The transverse normalized emittances in x and y directions are $\epsilon_x = 1.67$ mm-mrad and $\epsilon_y = 1.34$ mm-mrad, respectively. The charge of the electron bunch was 1 nC for both measured and simulated electron bunch distributions. The duration of the electron bunch is about 500 fs for both cases. The energy of the electron bunch for the measured distribution and simulated one were 700 MeV and 1 GeV, respectively.

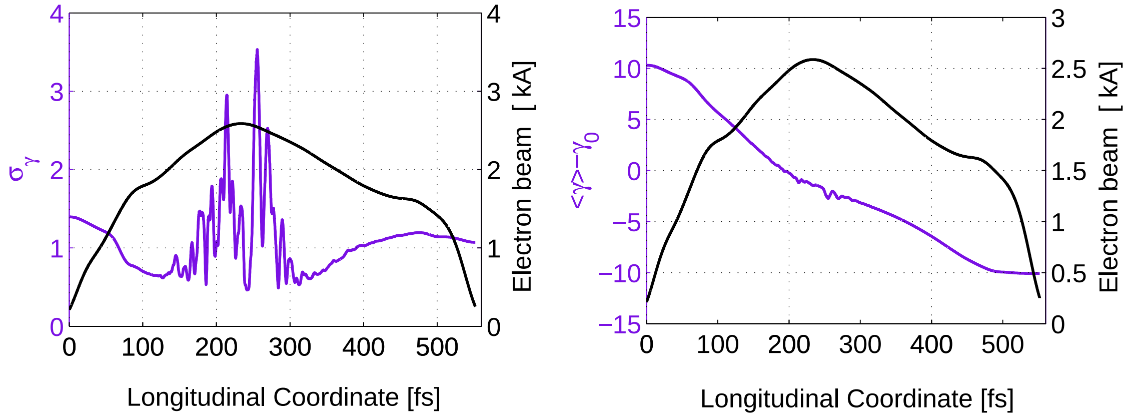

Figure 5.6: *Left: The normalized rms energy spread of the electron bunch distribution taken from start-to-end simulation. Right: the mean deviation form the mean energy. The electron bunch distribution is plotted in black.*

The electron bunch distribution taken from start-to-end simulation is used as an input for the GENESIS simulation. The energy of the seed pulse is assumed about 10 pJ at the entrance of the seeding undulator. The spectrum and output power of the seeded signal at the exit of the third undulator are shown in Fig. 5.7. The colored circles in Fig. 5.7(b) show the expected position of the seeded signal, considering the slippage effect. Enhancement in those points are hardly observable.

The same approach was applied to estimate the power and spectral contrast of seeded signals relative to the SASE background, see Fig. 5.8. Due to low seed pulse energy, which is in shot noise level of SASE, the power enhancement of the seeded pulse is not perceptible.

Due to the intrinsic relative jitter between two pulses, the chance to observe the enhanced signal gets even smaller. As a consequence an analytical study is presented in the following section to show the probability of the overlap between jittery pulses.

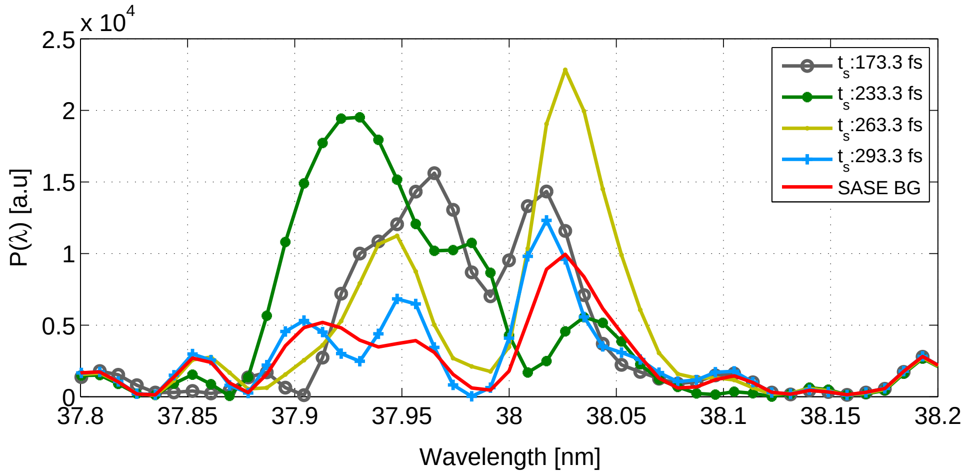

(a) *The spectral distribution of the seeded pulses.*

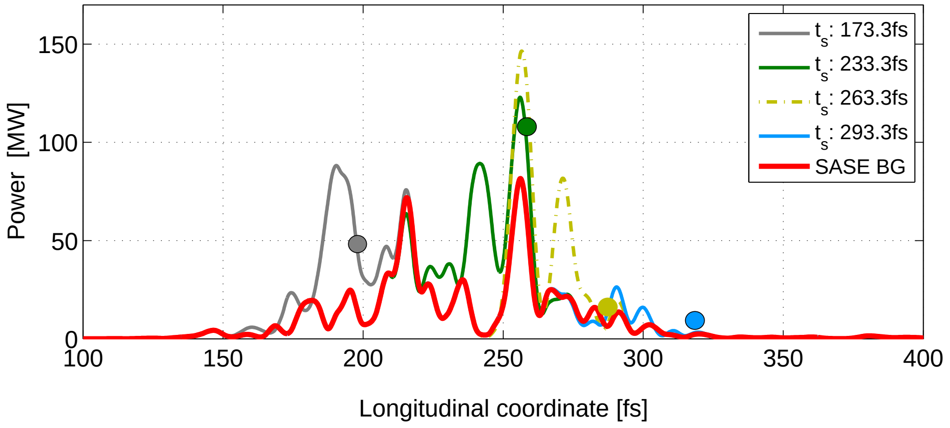

(b) *The output power of the seeded pulses. The colored circles show the expected position of the seeded pulse, considering the slippage effect.*

Figure 5.7: *The output power and spectrum of the seeded pulse relative to the SASE background for the electron bunch distribution taken from start to end simulation. The simulation is repeated for different seed pulse injection time along the longitudinal coordinate of the electron bunch.*

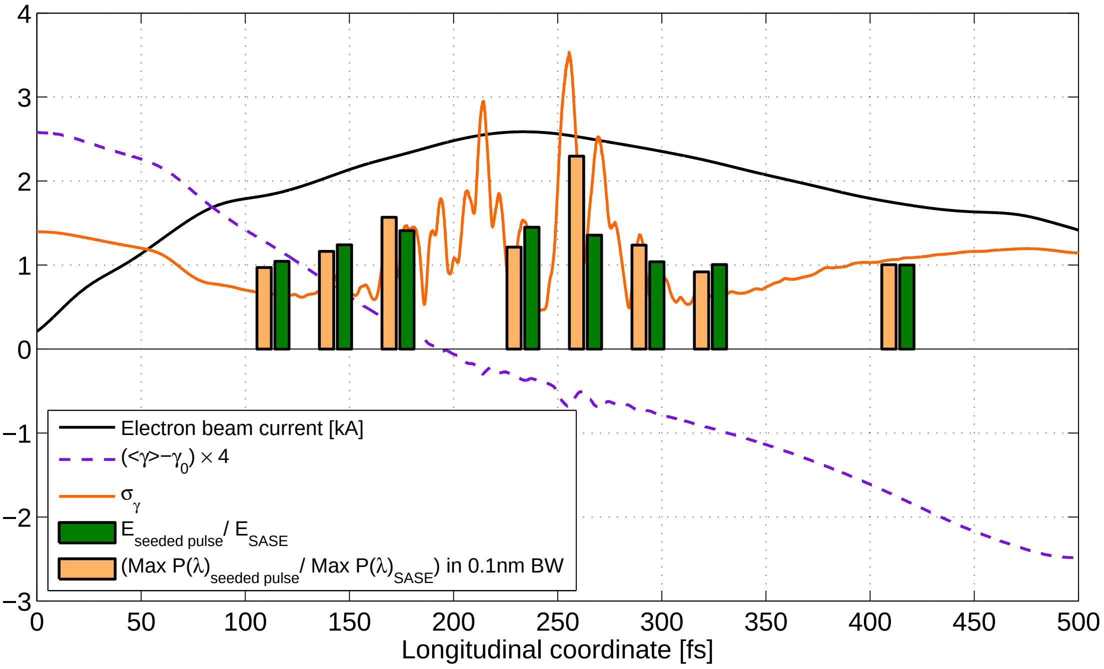

Figure 5.8: *The simulated spectrum of the seeded pulse for different delays between the HHG pulse and electron bunch.*

5.2 Statistical analysis of the jitter effects

5.2.1 Analytical approach

As was discussed above, due to the intrinsic longitudinal jitter of the laser $\sigma_{jl} \sim 100\,\text{fs}$ and the electron bunch $\sigma_{je} \sim 70\,\text{fs}$ the task of finding temporal overlap between these two short femtosecond pulses plays an important role in enabling the seeding experiment. The seeded FEL is a linear amplifier before reaching to saturation, so the output should be proportional to the convolution of the seed pulse and the electron bunch. For a better understanding of a probable longitudinal overlap between these two pulses, an analytical and statistical study is presented in this section.

One of the most important concepts in Fourier theory, the convolution, can be used here to determine the amount of overlap between the seed pulse and electron bunch, which is indicated in Eq. 5.1,

$$C_{s,e}(\tau) = f_e(t) \otimes f_s(t) = \int_{-\infty}^{\infty} f_e(t) \cdot f_s(t-\tau)\, dt \tag{5.1}$$

Here the convolution $C_{s,e}(\tau)$ between electron bunch and seed pulse is a function of τ, which is the temporal offset between two pulses, see App A. Thus the information about the longitudinal overlap between two pulses, which are subject to relative random jitter τ, will be embedded in this convolution function. The functions $f_e(t)$ and $f_s(t)$ are the longitudinal distribution of the electron bunch and the seed pulse, respectively, which are assumed to have a Gaussian distribution:

$$f_s(t) = \frac{1}{\sqrt{2\pi}\sigma_s} e^{-\frac{(t-\mu_s)^2}{2{\sigma_s}^2}}, f_e(t) = \frac{1}{\sqrt{2\pi}\sigma_e} e^{-\frac{(t-\mu_e)^2}{2{\sigma_e}^2}} \tag{5.2}$$

Here μ is the mean and σ^2 is the variance of the related distribution. The usual approach to solve Eq. 5.1 is to use the convolution theorem [Boa83]:

$$C_{s,e}(\tau) = F^{-1}[F[f_e(t)] \cdot F[f_s(t)]] = \frac{1}{\sqrt{2\pi\sigma_T^2}} e^{-\frac{\tau^2}{2\sigma_T^2}} \tag{5.3}$$

where $\sigma_T^2 = ({\sigma_e}^2 + {\sigma_s}^2)$ and $\tau = (\mu_s + \mu_e)$.

To estimate the threshold temporal offset (τ_{th}) between the pulses of interest, one would need to write the inverse of Eq. 5.3 as follow:

$$\tau_{th} = \sigma_T \sqrt{2 \log\left(\frac{1}{\psi}\right)} \tag{5.4}$$

where $\psi = \frac{C_{s,e}(\tau)}{C_{s,e}(0)}$ is the normalization factor. Here the optimum overlap can be defined as the $C_{s,e} \geq 0.9$. According to Eq. 5.4, the temporal offset between the electron bunch and seed pulse should be $\tau_{th} \leq 46.1$ fs to satisfy the optimum overlap condition. The probability to find a signal above the threshold can be estimated by:

$$P_{>} = 2 \int_0^{\tau_{th}} f_j(t)\, dt_j = erf\left(\frac{\tau_{th}}{\sqrt{2}\sigma_j}\right) \tag{5.5}$$

where $f_j(t) = \frac{1}{\sqrt{2\pi\sigma_j^2}} \exp\left(-\frac{t_j^2}{2{\sigma_j}^2}\right)$ is the relative jitter between the electron bunch and seed pulse which has a Gaussian distribution. As an example, in our case the probability of the optimum overlap for the τ_{th} =47 fs is $P_{>} \approx 0.3$. As another example, if the rms jitter is twice the threshold time ($\tau_{th} = \sigma_j/2$) then $P_{>} \approx 0.38$. In Fig. 5.9 the convolution of the electron bunch and the seed pulse for different τ/σ is shown. In the same figure the probability that the random events, under influence of normally distributed jitter with σ_j =122 fs, stay within the threshold limit τ_{th} is also shown.

The probability that the jitter remains within a range which assures the overlap of ($C_{s,e}(\tau)$) is shown in Fig. 5.10. As is shown, the probability of the optimum overlap between the seed pulse and the electron bunch is about 20%.

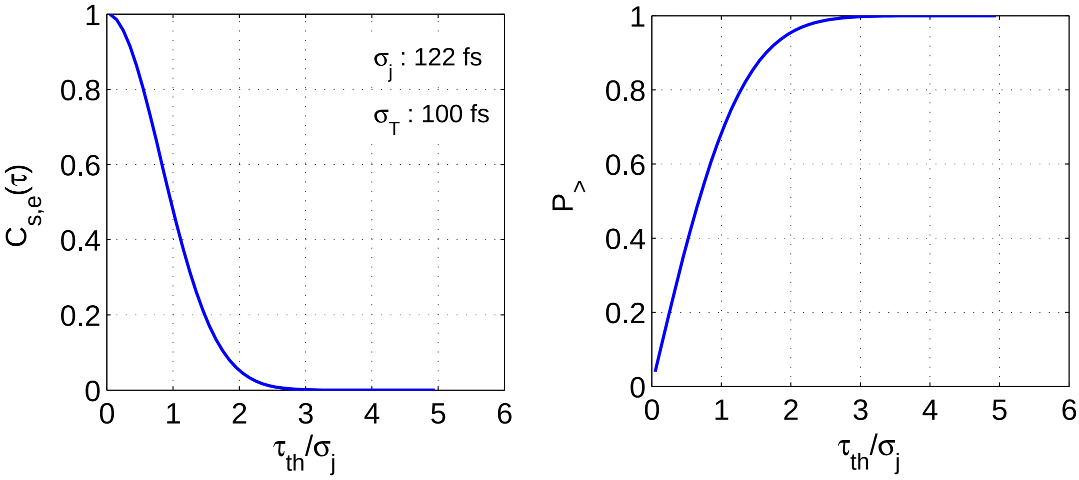

Figure 5.9: *Left: The convolution of the seed pulse (σ_s =10 fs) and the electron bunch (σ_e =100 fs) as a function of τ/σ_j. Right: The probability that the convolution function, under influence of normally distributed jitter with σ_j =122 fs, stays within the threshold limit τ_{th}.*

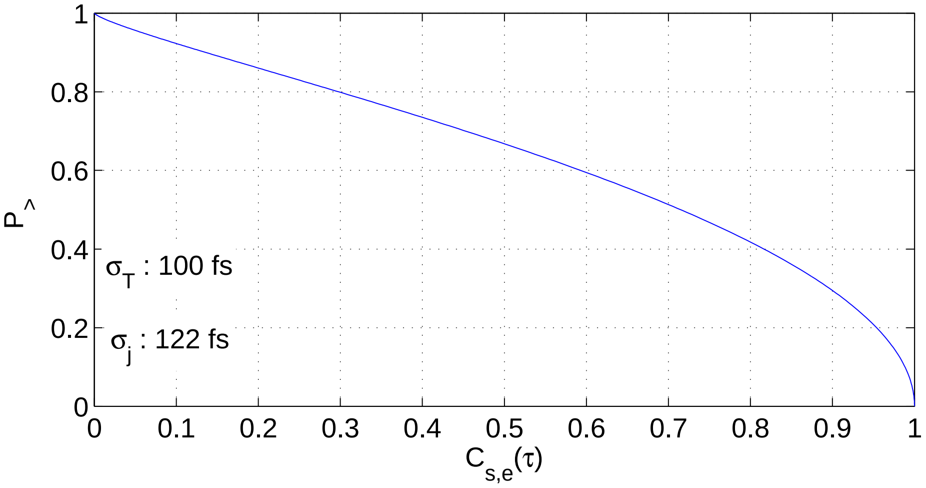

Figure 5.10: *The probability that the random jitter remains within a range which assures the overlap of ($C_{s,e}(\tau)$).*

5.2.2 Numerical simulation

In this section the probability to have the optimum overlap is estimated, using numerical simulation, for different varying parameters such as: relative random jitter between two pulses and electron bunch duration. For the beginning 500 number of shots per each steps was considered to have a trustable statistical analysis.

The effect of relative longitudinal jitter

The temporal offsets between the seed pulse and electron bunch are due to the longitudinal jitter of the pulses relative to each other. Any phase jitter in the RF gun, photocathode drive laser, and the accelerating modules causes energy jitter, and due to the differing delays through the dispersive section, this energy jitter translates to jitter in arrival time. Using beam arrival time monitors (BAM) installed in the FLASH accelerator, the average longitudinal jitter of the electron bunch was measured about 70 fs, using beam based feedback. A normal distribution for the longitudinal jitter of the electron bunch and the seed pulse as well is assumed with the standard deviations given by $\sigma_{je} = 70\,\mathrm{fs}$, and $\sigma_{js} = 100\,\mathrm{fs}$, respectively.

The random positions for the electron bunch and seed pulse can be defined as follows,

$$\mu_{e,s} = \mu_{e_0,s_0} + \sigma_{e,s} \cdot randn(1, M) \tag{5.6}$$

where M is the number of evaluations, σ is the standard deviation and μ_0 is the mean of the distribution. By substituting Eq. 5.6 in Eq. 5.3, the probability of the temporal overlap for the M different relative jitters between two pulses can be obtained. The results for different initial temporal offset is shown in Fig. 5.11. There is about 30% probability of optimally overlapping the electron bunch of $\sigma_e = 100\,fs$ with the seed pulse of $\sigma_s = 10\,fs$ using randomly generated jitter. The probability of overlap drops down to about 1% for the case in which the electron bunch and seed pulse are separated about 300 fs.

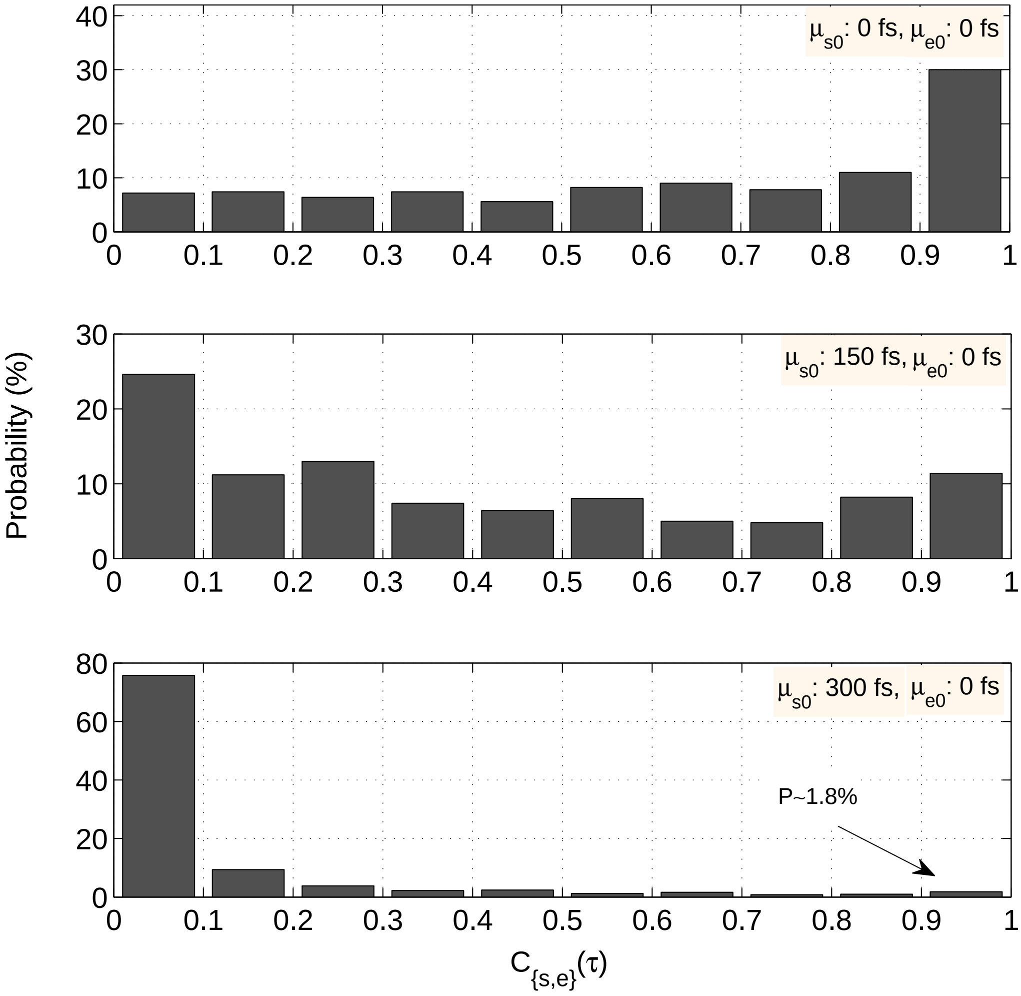

Figure 5.11: *The probability of the overlap between the laser pulse and electron bunch with normal-random generated longitudinal jitter. Here* μ_{s0} *is the mean offset between the seed pulse* ($\sigma_s = 10\,fs$) *and electron bunch* ($\sigma_e = 100\,fs$).

The effect of longitudinal electron bunch length

Due to differences in the compression process in the bunch compressors, the longitudinal profile of the electron bunch is subject to change along with the above-discussed overall jitter in arrival time . Providing a reasonable energy spread along the electron bunch, as well as high peak current ($\sim 2\,\mathrm{kA}$), and an appropriate electron beam duration, all at the same time (to fulfill the prerequisite condition for the longitudinal overlap of two jittering femtosecond pulses) presents a challenge. In this regard the effect of longitudinal length of the electron bunch on the randomly generated overlap function is presented in Fig. 5.12

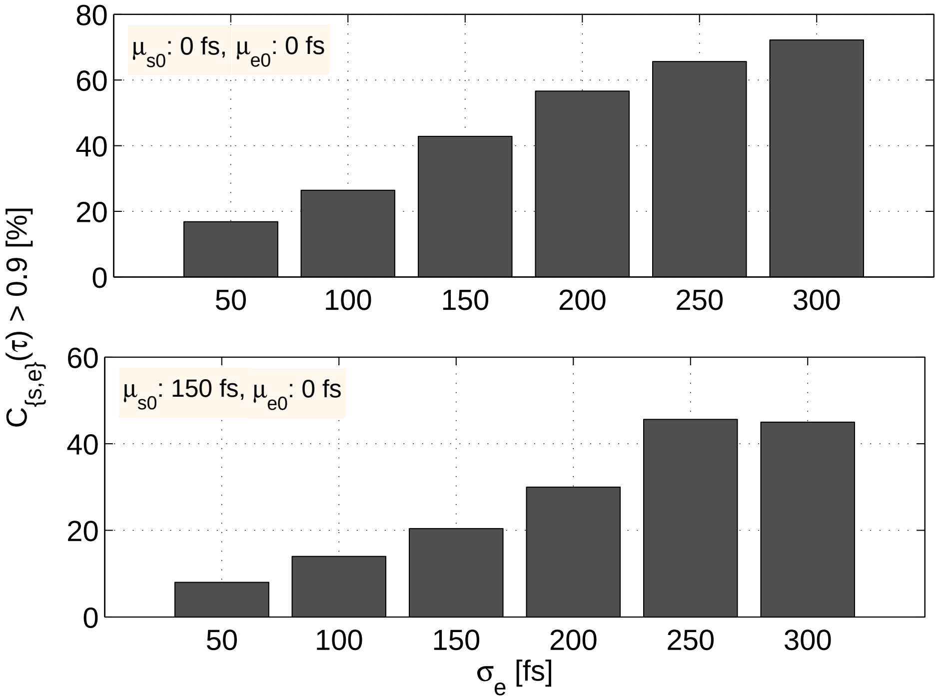

Figure 5.12: *The probability of the longitudinal overlap between seed pulse and electron bunch as a function of electron bunch duration. The figure in the top shows the probability of the optimum overlap for the zero initial temporal offset between pulses of interest. figure below shows the statistic for the case, that two pulses are separated initially about 150 fs.*

Again, in this statistical approach 500 number of shots per step is considered. The temporal offsets between two pulses are considered to be zero for the graph in the top and 150 fs for the graph below. There is still 10% probability to have the overlap between two pulses for the electron with $\sigma_e = 50\,fs$. The statistical analysis show that there is approximately 10% chance to bring two pulses together in an optimal way. In experiment, the scanning procedure that moves the laser relative to electron bunch is performed with 50 fs step in the fine temporal overlap setup.

Number of shots per scan

In Fig. 5.13 different numbers of evaluations are considered to estimate the probability of the optimum overlap. The rms jitter of the electron bunch and seed pulse are estimated to be 70 fs and 100 fs, respectively. In view of analysis and uncertainties on beam parameters, a number of approximately 50 hots seems to be a reasonable choice for a trustable statistics and would save the time during the commissioning shifts.

The statistic studies also show that the fine temporal overlap should be achieved better

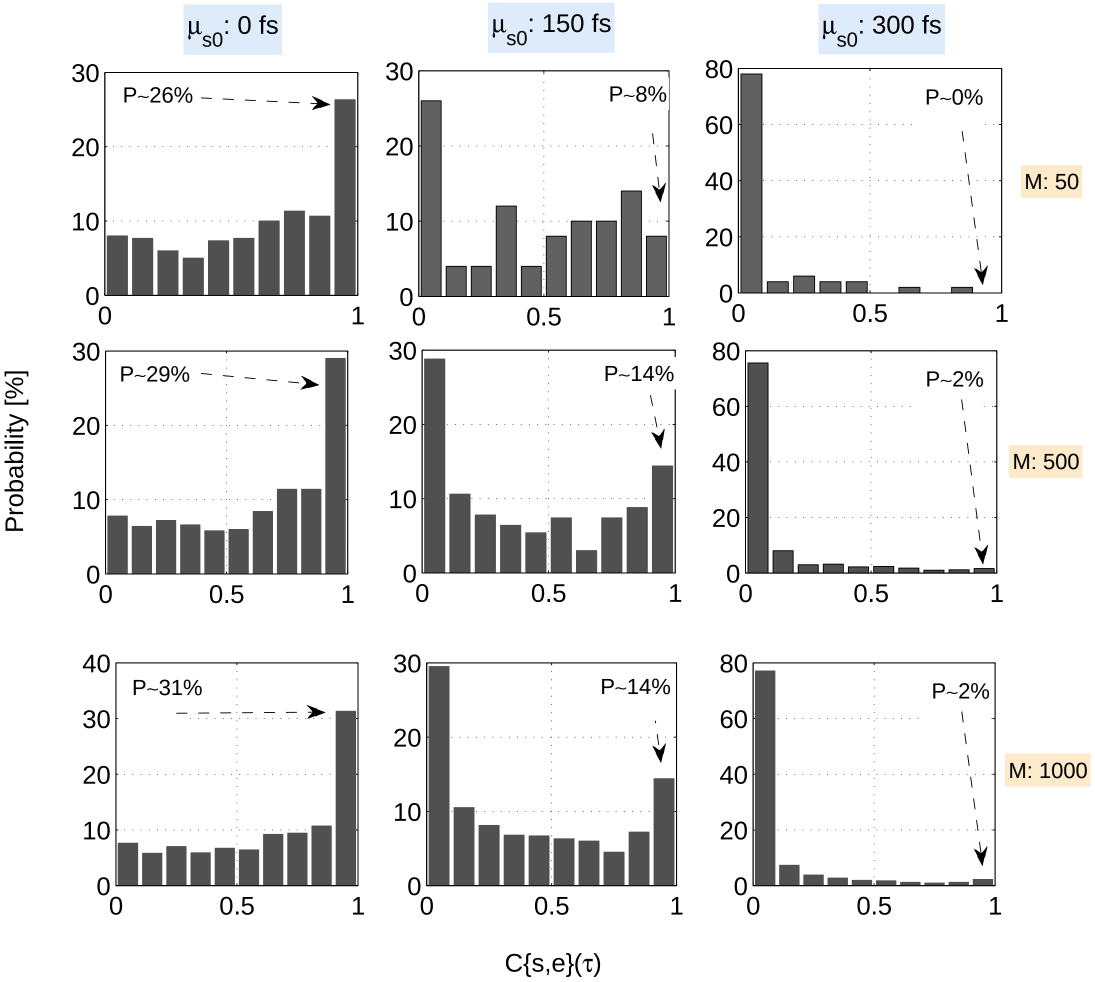

Figure 5.13: *Probability of optimum overlap ($C_{s,e}(\tau) \geq 0.9$) for different mean offsets of the laser pulse relative to the electron bunch (μ_s). M is the number of evaluations considered per each case.*

than 300 fs. The optimum overlap would hardly be achieved with the above-mentioned relative jitters of the electron bunch and seed pulse. The results of simulation show that the observable contrast decreases if the relative jitter is more than approximately 60 fs. The electron bunch properties, including energy spread and mean energy deviation also play an important role for the seeding experiment. Proposed methods to find the temporal overlap with required precision are discussed in detail in the following chapters.

6 Proposed methods for temporal overlap measurement

The characterization of the temporal profile of the laser pulse $(\sim 33\,\mathrm{fs})_{\mathrm{FWHM}}$ and electron bunch distribution is one of the most important preliminary steps in the seeding project. In this chapter possible electronic methods for measuring ultra short pulses and their temporal overlap are recounted which satisfy the purpose of this thesis in the most optimum ways.

6.1 Measurement with picosecond resolution

The NIR laser pulse and spontaneous radiation of the undulator carry information about the arrival times of the HHG pulse and the electron bunch, respectively. As an initial step in measuring the relative arrival times of these pulses, the coarse longitudinal overlap setup with picosecond resolution was installed after the first undulator of the ORS experiment, which is located upstream of the seeding undulator, see Fig. 6.1. The incoming lights are reflected out of the electron beamline using a silver-coated screen. The beams are forwarded to the detector station using 6 silver-coated mirrors. The transport beamline to the photo-detector station is explained more in details in Chapter7.

The strategy to find the temporal overlap between the HHG pulse and electron bunch with picosecond resolution is as follows: First, using a beam splitter a part of the NIR-laser beam is sent to a photomultiplier tube (PMT). The time difference between the two pulses can be measured within a few nanoseconds resolution using this detection method. Second, a streak camera based measurement provides the coarse temporal overlap better than 500 fs. In the following sections the technical characteristics of the photo-detectors, which were used, are explained.

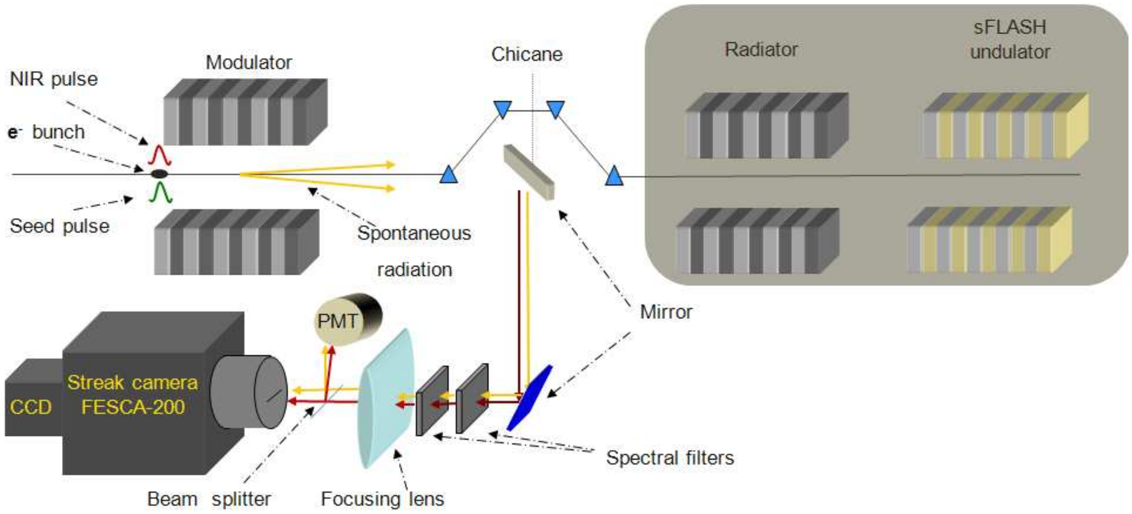

Figure 6.1: *Coarse temporal overlap setup installed between undulators of ORS-experiment. This setup is located upstream of seeding undulators. The temporal overlap between spontaneous radiation of the undulator and the NIR laser pulse is measured firstly by a photo-multiplier (nanosecond resolution) and secondly using a streak camera with resolution better than 0.5 ps.*

6.1.1 Photomultiplier tube

The PMT is composed of a photocathode, which converts light to photo electrons, which are then amplified by a cascading process. The photo-generated electrons, after an initial acceleration, are amplified through a series of dynodes via secondary emission. The multiplied secondary electrons emitted from the last dynode are collected by the anode. Unfortunately the photo electric response times are limited, thus restricting PMT detection utility when one is measuring femtosecond or picoseconds pulses. The PMT which was used in the experiment (H6780-20 model) has an effective area of 8 mm^2 and a rise time about 700 ps [Ham11b].

6.1.2 Streak-camera based measurement

The basic operation principle of the streak-camera (FESCA200) [Ham10, Rul05] is depicted in Fig. 6.2.

The light pulses arrive on the slit at different times, and a combination of lenses images them to the photocathode. There the incident light pulses convert to photoelectrons, just as in the photomultiplier. The resulting flux is collimated, strongly accelerated and deflected by an ultra-high-speed sweep of an applied electric field, through the streak unit.

To reduce the initial velocity distribution of the photo-electrons, the streak tube uses

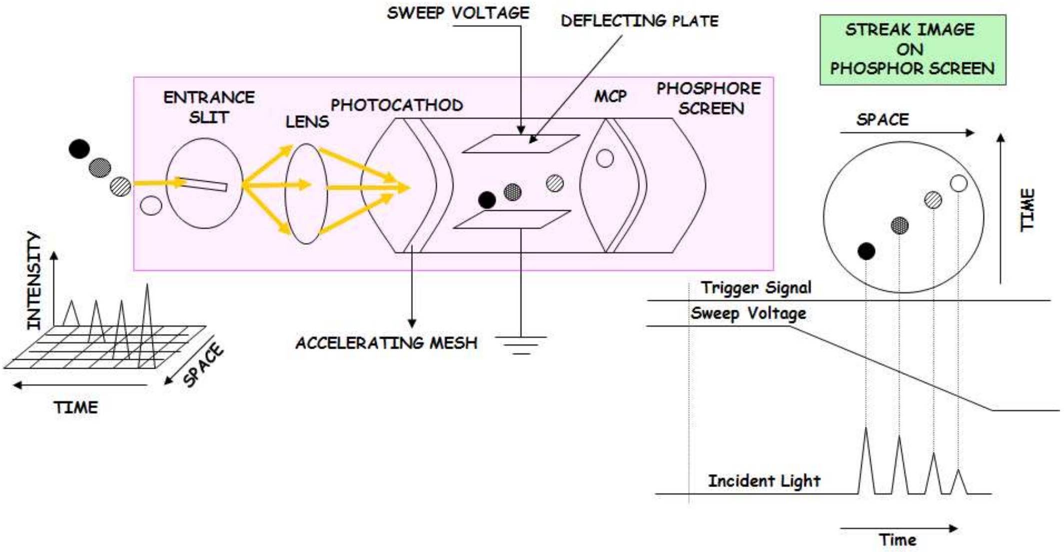

Figure 6.2: *The operation principle of the streak-camera operation, FESCA200, Hamamatsu.*

magnetic focusing, which can increase the field intensity between the photocathode and accelerating electrode. Then the impact of the electrons on the phosphor screen is mapped along an axis which is calibrated in time by the sweep itself. The light intensity here reflects the electron density and is a true image of the pulse itself.

To avoid space charge effects, one should keep the emissivity of the photocathode as low as possible. In order to increase the luminosity of the phosphor screen, a micro-channel plate is inserted to multiply the electrons by a factor of up to 1000 before the phosphor screen. The final image is read with a standard CCD camera using a computer and a frame grabber. The specification of the streak-camera which is used for our measurements are listed in Table. 6.1.

According to the type of the laser and measurement two different ways for recording the streak images can be implemented, either a single shot 'single sweep', or averaging over set of data using the synchro-scan mode. In the synchro-scan mode, the high-speed sweep (≈5 ns) repeats periodically and is synchronous to the incoming laser pulse. The resolution for the synchro-scan streak-camera is better than 50 ps.

Components

As shown in Fig. 6.2, the streak-camera FESCA200 [Ham10], consists of the following components:

- Input optics

Parameter	Value
Spectral response	280 to 850 nm (S20)
Effective photocathode size	$\phi\,3\,\mathrm{mm}$
Temporal resolution	better than 300 fs
Sweep time at full screen(10.29 mm)	20 ps, 50 ps, 100 ps, 200 ps, 500 ps
Trigger jitter	less than ± 20 ps
Operating mode	Focus/streak
Image magnification	1:1
Slit width	0-200 μm
Slit length	0-15 mm
Resolution (pixel)	1280 × 1024

Table 6.1: *Specification of the streak-camera, FESCA200*

The optics at the ingress of the streak camera are designed to image the incident light to the photocathode. To have a uni-dimensional image on the photocathode a slit with variable width is used. The dispersive parts of the optics for FESCA 200 are assembled of two materials, SiO_2 and CaF_2 with total thickness of 3.6 mm and 24.4 mm respectively. The image magnification is unity.

- Streak unit
  The streak unit consists of a deflection plate which can deflects the incoming photoelectrons with a rapidly time-changing kick. Before sweeping, an accelerating field due to accelerating voltage applied in the range between 2 kV to 5 kV brings the photoelectrons to keV energies.

- Image intensifier
  The image intensifier consists of a photocathode, the multichannel plate, and the phosphor screen. In the gate mode operation which is needed for the smallest time range (20 ps) the voltage of photocathode is set to zero or more to prevent it from unwanted photons. In the normal operation the voltage is set to -200 V.

- Output optics
  The output optics system connects the image intensifier, phosphor screen and read out camera.

Streak camera resolution

The time resolution of the streak camera measurement is a function of the spatial photo electron distribution and the size of the slit. The temporal profile of the electrons reflects the temporal evolution of the light intensity on the slit. The wavelength of the incoming light also impacts on the temporal resolution. For shorter wavelengths (photon energies larger than the work function of the cathode), photoelectrons from the photocathode spread spatially, due to the enhanced spread in transverse momenta, and result in a spread in the travel time inside the streak tube. When the number of photoelectrons is increased, space-charge forces are enhanced, producing another limitation in the resolution. Another parameter to improve the resolution is the sweep rate of the streak unit. The relative timing between electron flux and the sweep should be precisely set. A higher precision and resolution can be achieved with higher sweep rate. In practice, resolution of the FESCA200 is better than 300 fs. An example for the measured resolution of FESCA200 is shown in Fig. 6.3. One of the disadvantages of this kind of streak-camera for finding the temporal overlap between two pulses is the shot-to-shot fluctuation of the streak image on the phosphor screen, which is mainly due to the fluctuation in the trigger timing of the sweep circuit [Ham10]. The fluctuation due to timing jitter is about 20 ps.

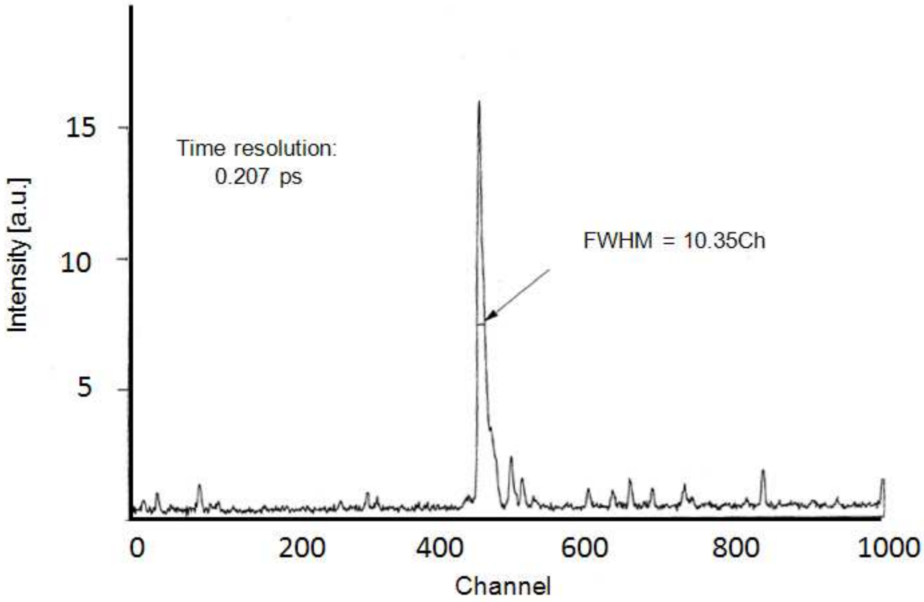

Figure 6.3: *Measured streak-camera (FESCA200) resolution. The size of each channel (pixel) is* $6\,\mu m$.

Synchronization of the streak camera with the master oscillator

To obtain the optimum resolution, the relative timing between sweep rate and arrival of the photo electron flux should be precisely set. For this to happen part of the incident beam is detected by means of a photo-detector (photomultiplier or a photodiode) dedicated to synchronization purposes. In this case the output signal of the photodiode can trigger the sweep, or through a photo-switch connecting it to the streak tube's deflecting plate electronics it can provide jitter free timing [Rul05]. In the experimental setup explained here, the external trigger coming from the master oscillator (MO) with fundamental frequency of 1.3 GHz is also used for synchronization purposes.

In Fig. 6.4, the synchronization of the streak-camera with the RF master oscillator is illustrated. A part of the incoming beam is reflected to a photomultiplier. A 10 Hz trigger (1 ns rms jitter), coming from the FLASH timing system is sent to the first delay generator DG535 with $(50\,\mathrm{ps})_{rms}$ channel to channel jitter, 5 ps resolution), which can produce up to four output signals [DG511]. The generated output ($\approx$ 1 ns rms jitter) with appropriate delay relative to the external trigger, is then sent to the CCD camera controller (channel B), to the main unit as a gate mode controller (channel D), and to the streak unit via another delay box (HMI box) [HMI] reducing the jitter to $(10\,\mathrm{ps})_{rms}$ by synchronization to the 108 MHz of the master oscillator.

The high-stability delay box C6878, is used as a phase shifter to adjust further the delay time of the trigger signal by adjusting the phase of the input signal. In addition the phase can be stabilized and that allows the reliable acquisition of the streak images, [Ham11a]. For the input signal of 108 MHz (the 12th harmonic of the MO frequency) that is used for the synchronization, delay of the trigger signal can be adjusted automatically up to 9.23 ns.

6.2 Measurement with femtosecond resolution using MOR[1] setup.

Due to the limit in the resolution of current optical and electronic methods, one would need to find another concept to measure the temporal difference between the femtosecond pulses of interest with resolution in the order of sub-100 femtoseconds.

The principle of operation of Optical-Replica Synthesizer setup (ORS) was introduced in Chapter 3. The ORS is based on the optical klystron concept which was discussed in Chapter 2. This scheme has been experimentally deployed at FLASH for measuring the longitudinal profile of the electron bunches [SSS07]. An analytical investigation presented in this section shows the potential of this setup for measuring the temporal overlap between two femtosecond pulses, see Fig. 6.5.

In presence of an undulator field and a very large external laser field, obeying the resonance

---

[1] MOdulator-Radiator setup

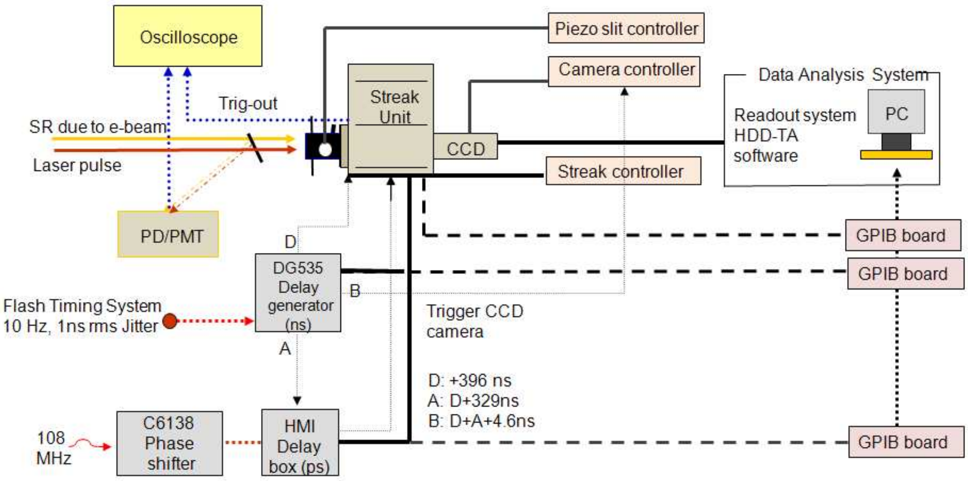

Figure 6.4: *Synchronization layout of the streak-camera based measurement with sub-picosecond synchronization with the master oscillator. A part of the two incoming beams to the streak-camera are coupled out to a relatively fast photo-detector. This signal is sent to the oscilloscope together with the output trigger of the streak unit to adjust the relative timing and to find the signals within the camera time range (largest* $\approx 500\,ps$*). The 10 Hz signal coming from the FLASH timing system with 1 ns rms jitter is coupled to a delay generator unit (DG535) with intrinsic jitter of 50 ps. Afterwards another delay box (HMI) is used to reduce the existing jitter furthermore by using the 12th harmonic of MO fundamental frequency (108 MHz). The intrinsic jitter of this box is 10 ps. The 108 MHz signal is coupled firstly to a phase shifter (C6138) which can be remotely operated. This box stabilizes the phase and allows more stable acquisition of the streak images.*

condition in Eq. 2.5, the electrons are bunched. This bunching is enhanced by passage through a chicane with an R_{56} that can be varied up to 150 μm in the current setup, see App B.

Electrons with different energies pass through different paths in the chicane. This effect induces an enhanced density modulation in the previously energy-modulated electron bunch. The density-modulated beam is then passed through the second horizontally polarized undulator where it may emit coherent spontaneous radiation that is reflected to a spectrometer transport line by a screen. In case of perfect overlap between NIR pulse and electron bunch, a significant enhancement in the coherent light can be observed. The resonance condition can be also obtained when the laser is a multiple of the undulator frequency, see App C. For our case the coupling at the fundamental wavelength is studied. The parameters of the modulator and radiator are presented in Table. 3.1.

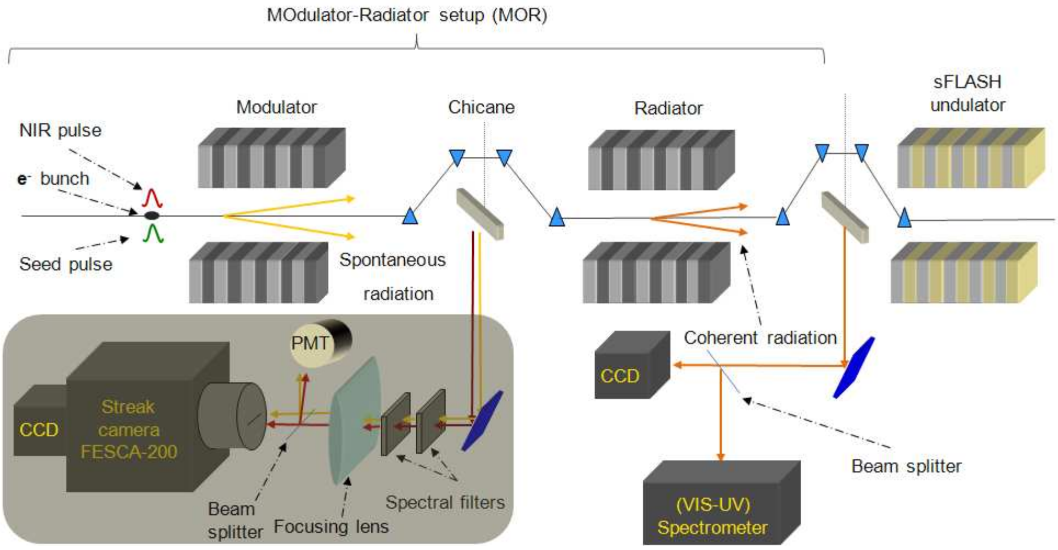

Figure 6.5: *Schematic diagram of the modulator-radiator setup. The spontaneous radiation from the first undulator (modulator), together with the NIR pulse, is coupled out to the first station using an OTR screen. The overlap of two pulses are achieved within 500 fs using a streak camera-based measurement. Using a downstream chicane ($R_{56} = 150\,\mu m$) the electron bunch that is modulated in energy within the modulator becomes modulated in density. The emitted coherent light after the second undulator (radiator) indicates the presence of longitudinal and transverse overlap between the two pulses, which can be resolved spectrally using a VIS-UV spectrometer or a CCD camera.*

6.2.1 Experimental methodology

To perform fine temporal overlap with femtosecond resolution, the modulator is tuned to be resonant at the NIR pulse wavelength, 800 nm. The NIR pulse ($t_{\text{FWHM}} \sim 33$ fs, energy ~ 22 mJ) is focused at the beginning of MOR setup by a focusing mirror with focal length of f=5 m.

The energy of the laser is measured to be $\Delta U_L \sim (50 \pm 5\ \mu\text{J})$ at the optical station after the modulator, see section. 8.2. The total power (P) and corresponding electric field (E_T) of the NIR pulse are $P = \Delta U_L/(\sigma_t.\sqrt{2\pi}) = 607\,\text{MW}$ and $E_T = \sqrt{\frac{2I}{c\epsilon_0}} = 381.5\,\frac{\text{MV}}{\text{m}}$, respectively, where $I = 2\times10^{10}\,\frac{\text{W}}{\text{cm}^2}$ is the NIR beam intensity.

Due to vertical polarization of the modulator, only the vertical component of the laser field (E_y) can contribute in the interaction process. Simulation results using the optical design software ZEMAX [zem11] show that the vertical field component of the NIR laser beam after propagation through the seeding beamline is about 50% of the total field ($E_y = 0.54E_T$), see App D. The size of the mirrors that are used in the beamline put a limit on the transportation of the initial field. Assuming the vertical electric field strength to be 20% of the total field the coupled electric field would be $\mathrm{E}_y = 76.3\,\frac{\mathrm{MV}}{\mathrm{m}}$. The fundamental harmonic of laser interacts with the electron bunch and induces the energy modulation amplitude (P_0) as follow:

$$P_0 = K_p \frac{e}{2} \frac{E_y z}{\gamma} = 244\,\mathrm{keV} \tag{6.1}$$

where $K_p = 8.8$ is the peak undulator parameter and $z = 1\,\mathrm{m}$ is the length of the modulator.As was explained in Chapter 4, focusing mirrors are installed in the beamline to focus the HHG pulse within the first seeding-undulator. Among them a dielectric-coated mirror with $f = 5\,\mathrm{m}$ is placed to focus the NIR laser at the beginning of the modulator with more than 80 % reflectivity. Use of this mirror yields the highest modulation of the electron bunch due to higher transported energy with a small transverse size of the NIR laser, approximately $(1\,\mathrm{mm})_{\mathrm{FWHM}}$. In Fig. 6.6 the amount of energy modulation for different transverse sizes of the NIR laser is plotted.

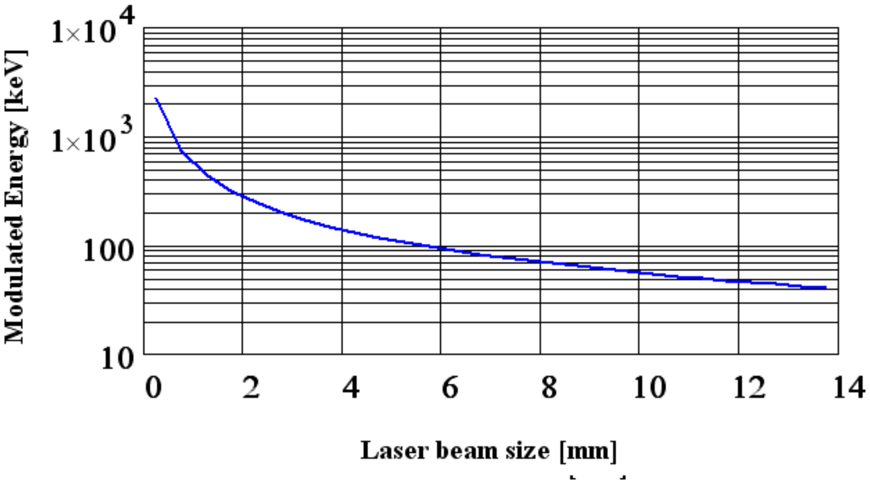

Figure 6.6: *Energy modulation within the modulator as a function of NIR-laser transverse size.*

For an electron beam with energy of $E_e = 700\,\mathrm{MeV}$ and a dispersive section strength of $\mathrm{R}_{56} = 150\,\mu\mathrm{m}$, the relative longitudinal shift of the electrons at the exit of the dispersive section would be:

$$dz_{max} = R_{56}\,\frac{P_0}{E_e} = 53.8\,\mathrm{nm} \tag{6.2}$$

which gives rise to a maximum density modulation (D_m) and associated enhancement of the coherent signal with respect to the incoherent signal as follows:

$$D_m = \frac{2\pi}{\lambda_L} dz_{max} = 0.42 \tag{6.3}$$

$$En_c = N \cdot {D_m}^2 \sim 10^7 \tag{6.4}$$

where $N = \frac{Q'}{e} = \frac{Q\lambda_L/(c\sigma_t)}{e}$ is the estimated number of electrons in the bunch, which are interacting within one laser wavelength (λ_L =800 nm), and Q is the total charge. For an electron bunch with Q =1 nC and duration of σ_t =300 fs, approximately 5.5×10^7 electrons are considered to take part in the laser-modulation interaction. It should be mentioned that in estimating the enhancement the uncorrelated energy spread and energy chirp are not taken into account. For this reason in the following section the effect of energy spread on the fundamental bunching is presented.

The role of uncorrelated energy spread on the fundamental bunching

The enhanced coherent power due to the fundamental component of the current modulation at the radiator can be estimated according to the theory presented by Saldin, et. al. [Sal05]. The electron beam properties, dispersive strength, and the amplitude of the energy modulation, assumed for this analytical study, are summarized in Table. 6.2.

Parameter	Symbol	Value
Electron beam energy	E_e	700 MeV
Uncorrelated energy spread (rms)	σ_E	500 keV
Dispersive strength	R_{56}	154.4 μm
Energy modulation amplitude	P_0	244 keV

Table 6.2: *The electron beam properties, dispersive strength, and the amplitude of the energy modulation, assumed for this analytical study.*

As was discussed in Chapter 2, the energy modulated beam converts to a density modulated one within the chicane. Therefore a set of harmonics would exist in the radiator. The most important component is the fundamental term which is in resonance with the radiator. The amplitude of this fundamental micro bunching is expressed as a product of a Bessel function and an exponential term as expressed in Eq. 2.16. The fundamental harmonic component of the micro-bunched current for our case can be deduced to be:

$$a_1 = 2J_1\left(P_0 \frac{2\pi}{\lambda_L}\frac{R_{56}}{E_e}\right) \exp\left[\frac{-1}{2}{\sigma_E}^2\left(\frac{2\pi}{\lambda_L}\frac{R_{56}}{E_e}\right)^2\right] = 0.28 \tag{6.5}$$

The dependency of the 1^{st} harmonic amplitude on R_{56} is introduced both in the Bessel argument and in the exponential term. In Fig. 6.7 the role of the slice energy spread on the fundamental bunching amplitude with different values of R_{56} is shown.

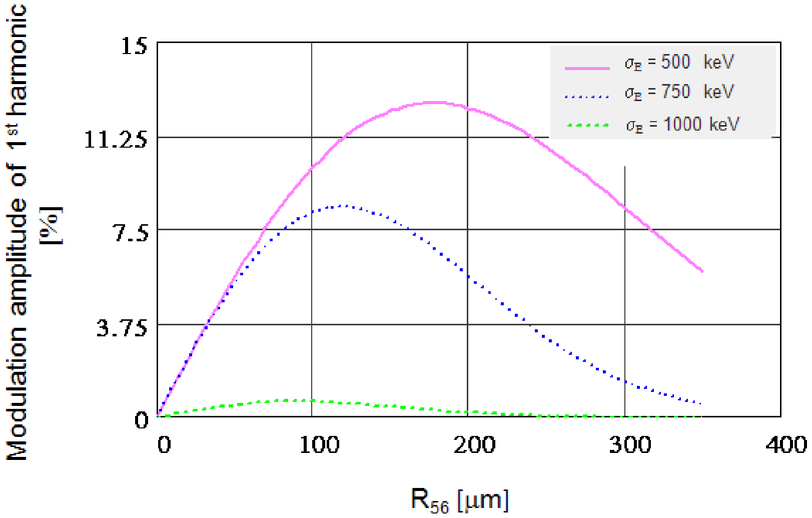

Figure 6.7: *Dependency of* 1^{st} *harmonic amplitude on the compaction factor* R_{56} *for different slice energy spreads* (σ_z) *of the electron bunch.*

The total radiation power (W) is estimated using Eq. 2.17 and Eq. 2.18.

$$W = W_0\, F(N_D) = 44.5\,\mathrm{MW} \tag{6.6}$$

where $W_0 = 68.5\,\mathrm{MW}$ is the normalization factor for the planar undulator. The dimensionless parameter $F(N_D) = 0.65$ is calculated using Eq. 2.17 for the diffraction parameter $N_D = 0.14$. The number of photons within the generated coherent radiation $(800\,\mathrm{nm}, 1.5\,\mathrm{eV})$ can be estimated at $N_{ph} = \frac{W\sigma_t}{1.5\,eV} = 6 \times 10^{12}$, where $\sigma_t = 32.9\,\mathrm{fs}$ is the NIR laser FWHM duration.

In the experiment this level of enhanced radiation can be easily detected by a CCD camera. As an example, for the CCD-camera, model Basler-A311f [Bas11], the size of the sensors and each pixel individually are $30\,\mathrm{mm}^2$ and $(10\,\mu\mathrm{m}\times 10\,\mu\mathrm{m})$ respectively. Assuming a homogeneous energy distribution over all pixels, approximately 2×10^7 photons would be detected by each pixel of the sensor, which is far above the minimum photon number required for the detection of the camera. The uncorrelated (slice) energy spread of the electron bunch plays an important role in the final bunching within the modulator and thus in the coherent radiation which is generated within the radiator. The dependence of the bunching and followingly the generated power in Eq. 2.18 on the slice energy spread is plotted logarithmically in Fig. 6.8. The dependency of the coherent light production on the strength of the chicane R_{56} for different uncorrelated energy spreads σ_E is plotted logarithmic in Fig. 6.9.

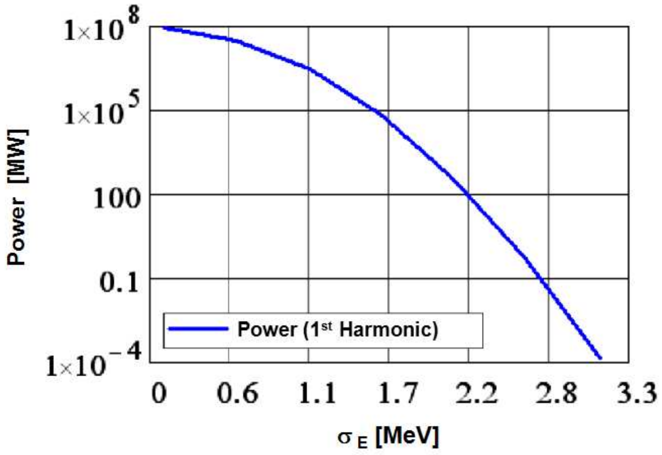

Figure 6.8: *The logarithmic plot shows the coherent power produced within the radiator at the fundamental wavelength of the NIR laser as a function of slice energy spread of the electron bunch.*

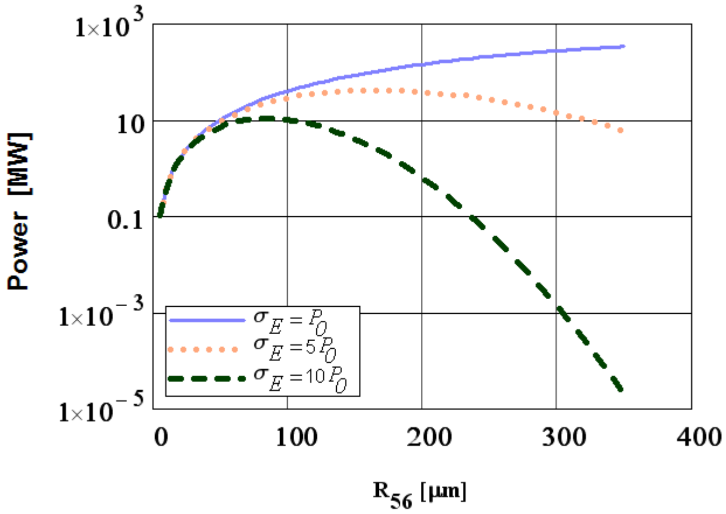

Figure 6.9: *Logarithmic enhancement of the coherent light in the MOR setup as a function of the chicane strength (R_{56}) for different ratio between modulated energy (P_0) and energy spread of the electron bunch (σ_E).*

6.2.2 Simulation results using PERSEO

A numerical simulation code called PERSEO [Gia] has been used to explore the electron bunch interaction with the external light source in the context of the MOR setup. The parameters of the interest, which are summarized in Table. 6.3, describe an electron bunch taken from a start-to-end simulation (see Fig. 5.6) interacts with the field of the NIR laser pulse in the modulator.

Parameter	Symbol	Value
Electron beam energy	E_e	1000 MeV
Uncorrelated energy spread (rms)	σ_E	0.04 %
Normalized x-emittance	ϵ_x	1.67 mm mrad
Normalized y-emittance	ϵ_y	1.34 mm mrad
Peak current	$\hat{I}$	2.6 kA
Bunch length (rms)	σ_{ez}	135.3 fs
Energy chirp		14 MeV/mm
Seed wavelength	λ_s	800 nm
Peak seed power	E_s	50 μJ
Seed energy	P	1.6 GW
Seed length (rms)	σ_{sz}	12.7 fs

Table 6.3: *The electron beam and NIR laser pulse properties used for the PERSEO simulation.*

The amplitudes of the modulation for the fundamental wavelength and second harmonic are shown in Fig. 6.10. The properties of the modulator and radiator are summarized already in Table. 3.1.

The violet curve shows the fundamental bunching coefficient at the end of the modulator ($a_1 \sim 0.5$). The field emission amplitude through the entire undulator is plotted as a red curve. The large R_{56} causes a separation between the longitudinal coordinate position associated with the bunching and that of the generated radiation pulse. The electron bunch is plotted in black dashed-line for comparison.

The phase-space of a selected slice, with width of 10 μm around the peak of the electron bunch current, is shown in Fig. 6.11, to illustrate the scenario described above.

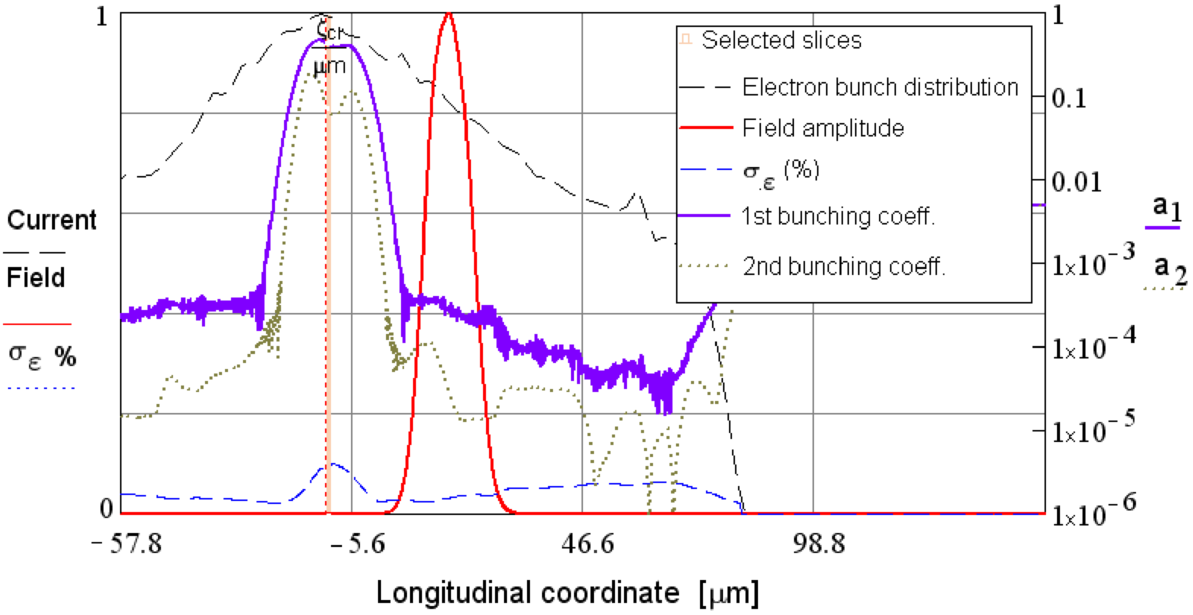

Figure 6.10: *Simulated bunching amplitude and emitted radiation using PERSEO.*

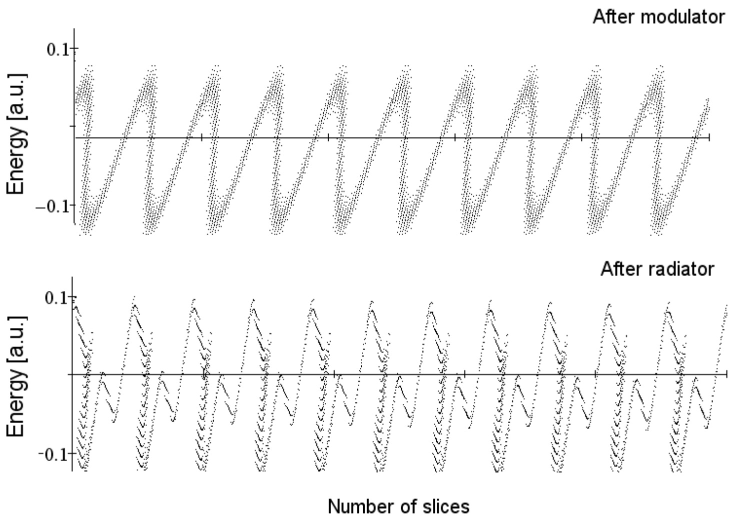

Figure 6.11: *Phase space of selected slices after modulator and radiator.*

The calculated enhanced coherent power along the radiator, for the first and second harmonics, is plotted in Fig. 6.12. The energy of the fundamental harmonic of the radiator, which is tuned at 400 nm, is 0.026 mJ. This energy is equivalent to $N_{ph} = \frac{E_{400\,nm}}{3.11\,eV} = 5.2 \times 10^{13}$ number of photons.

The analytical study and simulation results show that the enhanced coherent energy is

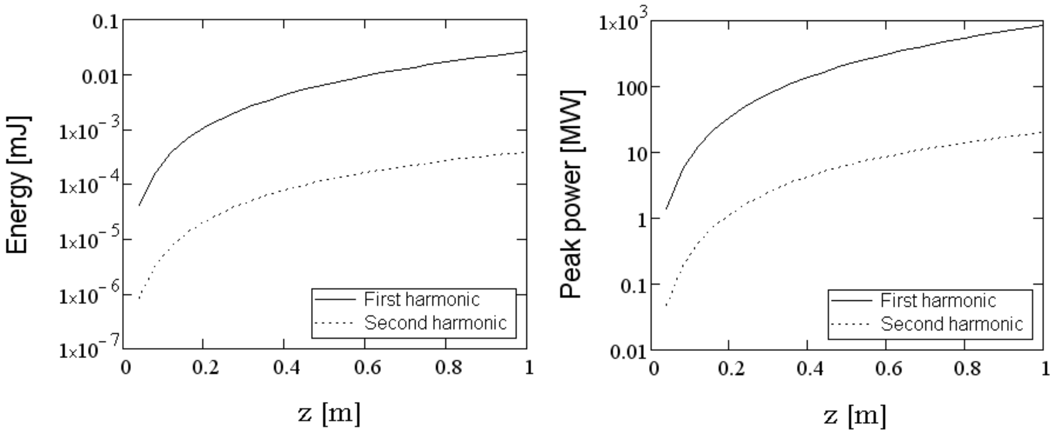

Figure 6.12: *Enhanced power along radiator, taken from PERSEO.*

of the order that can be easily detected with a normal CCD camera. In this regard, in the experiment a CCD camera together with a UV-VIS spectrometer were installed after the radiator. More details concerning the experimental setup and constructed beamline follow in the next chapters.

7 Beamline and shielding for the longitudinal overlap measurement

7.1 Description of the setup

During shutdown of 2009, the Optical Replica Synthesizer (ORS) experiment was moved upstream the seeding undulator, placed after the last accelerating module. The seeding experiment takes advantage of this setup to diagnose the electron bunch and the seed pulses longitudinal and transverse properties. As shown in Fig. 7.1 the time-coincidental drive laser and the HHG seed pulses are coupled to the electron beam using an in-coupling beamline. The coarse longitudinal overlap setup is installed directly after the modulator. The incoherent synchrotron radiation of this undulator carries information about the arrival time of the electrons.

The emitted incoherent synchrotron light can be separated from the electron bunch at the magnetic chicane in the optical stations placed after each undulator. The magnetic chicane consists of four dipoles magnets which steer the electron bunch around the screen, producing a maximum longitudinal dispersive strength of approximately $\mathrm{R}_{56} = 150\,\mu\mathrm{m}$.

The modulator radiation together with the NIR laser pulse (λ_L =800 nm) are reflected out of the beamline with a silver coated screen (150 nm coating) at the first optical station. The screen dimension is 40 mm by 22 mm, and is located 45 ° with respect to the direction of the beam. The reflected beams are sent down to the optical table using a planar mirror. The beamline from the screen to the coarse timing setup consists of 6 silver coated mirrors, with dimensions of 65 mm by 80 mm. The reflectivity of these mirrors for λ =800 nm is more than 97%. The reflection drops down for the wavelengths below 400 nm [lin11].

There is a translation stage on the optical table which sends the incoming beams to different diagnostic stations, Fig. 7.2. As it is shown, the mirror mounted in the right side of the translation stage sends the light beams to a power meter for energy measurement. The mirror in the middle sends the beams to an optical transition radiation station (OTR)

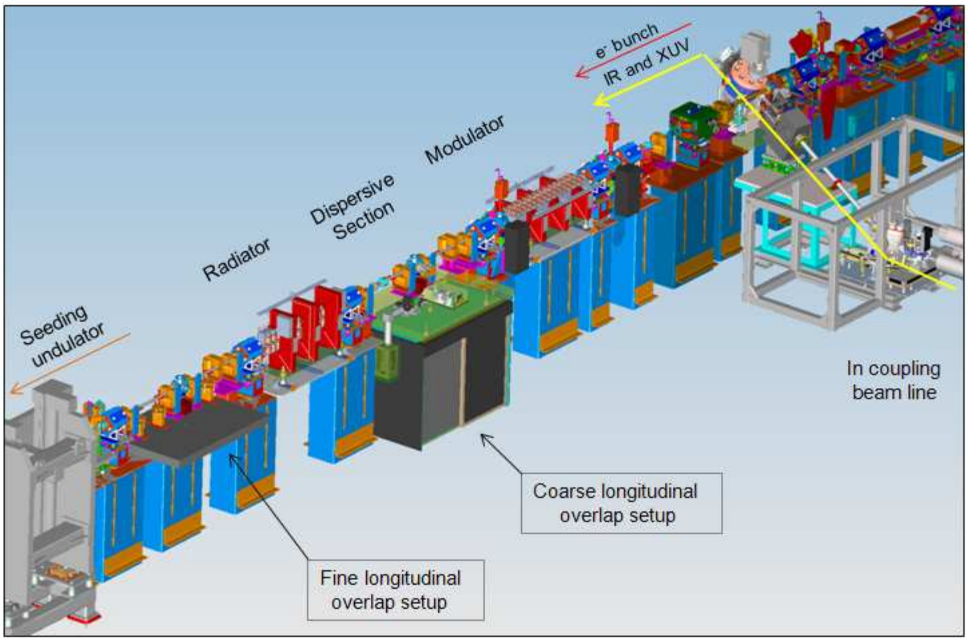

Figure 7.1: *Layout of the coarse and fine longitudinal overlap setup. The synchrotron radiation of the first undulator carries information about the electron bunch arrival time. This radiation together with the laser which co-propagates with the UV seed pulse are sent to the streak camera container for the longitudinal overlap with picosecond resolution. Following that the coherent radiation of MOR setup is used as a tool for the overlap with sub picosecond resolution.*

with a CCD camera which is initially used to find the transverse position of the beams on the screen. The third mirror sends the seed drive laser, together with the synchrotron radiation, through the same beamline to a container which is located underneath the optical table. This container, explained in the next section, is designed and constructed to protect the photo detectors against the ionizing radiation existing in the FLASH tunnel.

To bring the light beams to the slit of the ST-camera (width $\approx 30\,\mu$m), two of the mirrors are mounted on the translation stages to scan the position of the beams within ± 4 cm in horizontal and vertical directions. To control the angle of incident light one of the mirrors in the beamline is equipped with a motorized micrometer. A filter-wheel installed on the table uses different neutral density filters together with the spectral filter BG39 [Sch11a] to attenuate the light by a factor of up to 10^5. Afterwards the light beams are sent down to the container, see Fig. 7.3.

The laser beam and synchrotron radiation, after passing through spectral filters mounted in a second filter-wheel, are focused to the slit of the camera using a biconvex lens with focal length of ($f = 500$ mm). The lens is mounted on the translation stage for better focusing. A beam splitter (50%) sends the beam to the ST-camera and simultaneously to the CCD camera which is placed in the same distance from the beam splitter at 90° angle. Firstly the positions of the two incident light beams are found in the CCD camera. Secondly using motorized mirrors the beams are steered to permit observation in the focusing mode of the ST-camera, which shows the spatial profile of the incoming light.

The beams can be also sent to the photomultiplier (with $t_{rise} \approx 700\,\mathrm{ps}$) located in the same translation stage for finding the timing of the pulses relative to the internal trigger of the ST-camera.

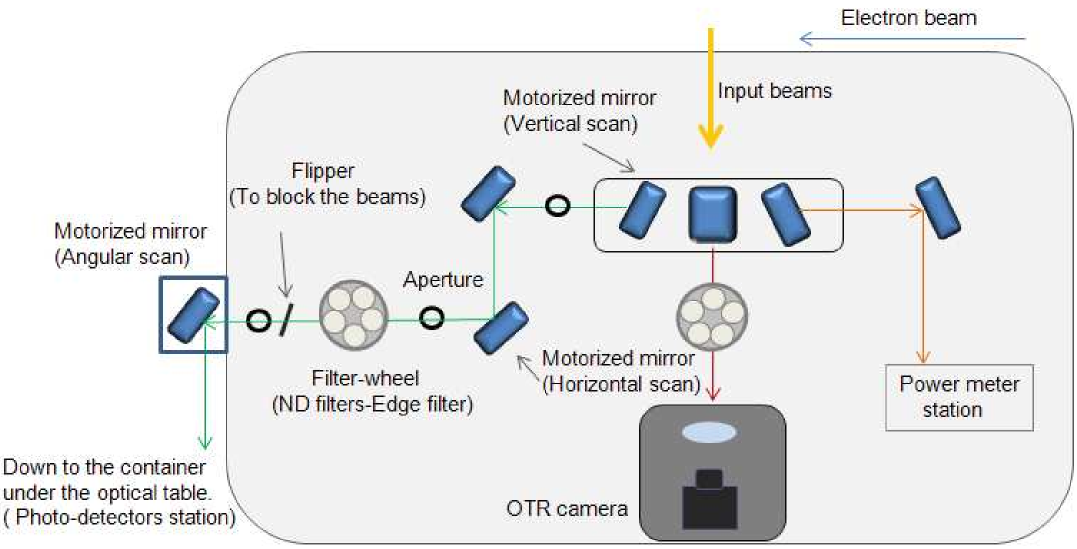

Figure 7.2: *The remotely accessible optical beamline to the coarse timing setup installed on the first optical table after modulator. The first translation stage on the table sends the incoming beams in three different diagnostics stations including power meter, OTR camera and to the ST-camera container which is located underneath this table. To bring the synchrotron light of undulator and laser beam on the slit of the camera, two of the mirrors are mounted on the translation stages to scan the position of the beam in horizontal and vertical directions. To adjust the angle of incoming beams one of the mirror is equipped with motorized angular knobs. The filter-wheel contains 3 neutral density filters and one spectral filter (BG39) to attenuate the high power laser pulses and modulator radiation appropriately. Using 2$''$ apertures the central part of the beam is sent to the slit of the camera which is set at a width of 30$\,\mu$m.*

A fiber spectrometer is also installed on this translation stage to record the spectrum of the modulator. The spectral range of this spectrometer is 350 nm to 1000 nm, [oce11]. The core diameter of the fiber-coupler of the spectrometer is 200 μm, which makes the remote focusing of the synchrotron light into the fiber quite difficult. To ease the coupling a compound parabolic concentrator, [edm11a] with an input diameter=10 mm and acceptance angle=45° has been chosen. The spectrum of the modulator can be recorded after using different spectral filters which are available in the beamline. This helps for the estimation of the amount of dispersion of the light in the beamline.

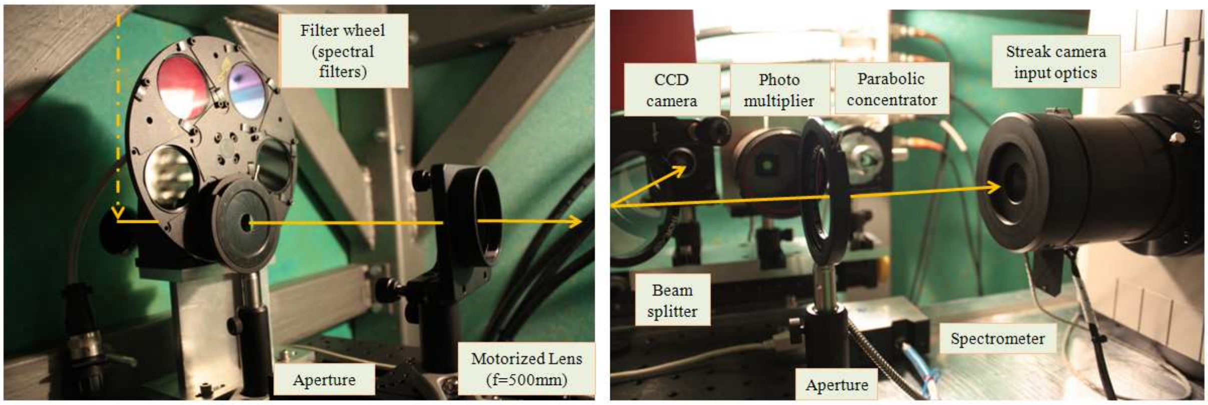

(a) *The remotely accessible optical beamline inside the container. Using two plane mirrors the beams are sent down to the container, where the ST-camera, photo multiplier and other photo detector are installed.* ***(Left)****: The second filter-wheel mounted in the container contains different spectral filters to attenuate the energy of the incoming beams with appropriate ratio. To focus the beam in the slit of the camera a biconvex lens is placed on a translation stage which can change the focusing point by 100 mm.* ***(Right)****: A beam splitter sends parts of the incoming lights firstly to a CCD camera for alignment purposes. Afterwards the beam is sent to a photo multiplier for finding the temporal overlap with nanosecond resolution. Beams can be sent also to a VIS-IR spectrometer to spectrally resolve the radiation of the modulator.*

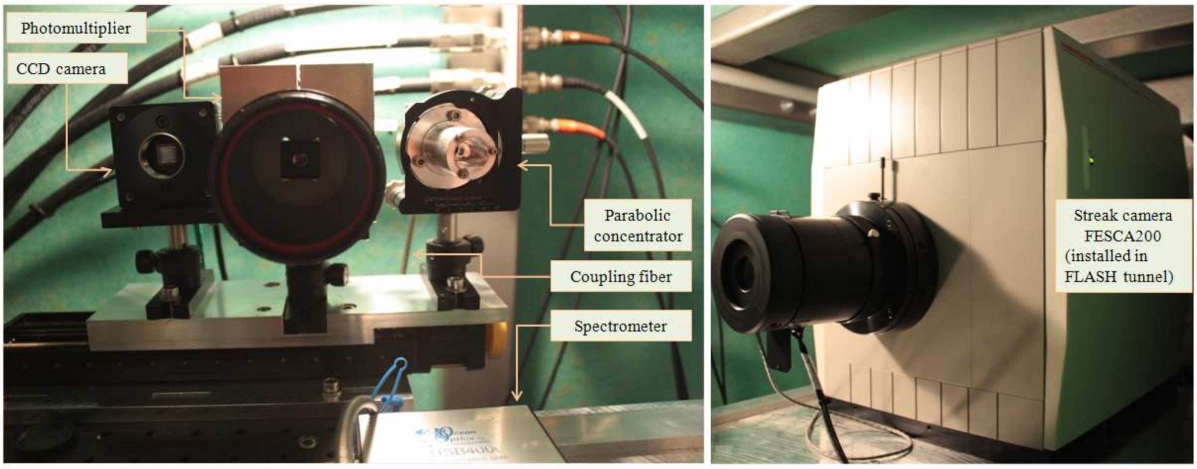

(b) ***(Left)****: The translation stage in the same distance as the slit of the camera from the focusing lens. On the right side a parabolic concentrator is mounted to collect the radiation and send it via fiber optics to the IR-VIS spectrometer. A photomultiplier is mounted in the middle in a cylindrical tube which is used for shielding against background light. The CCD camera in the left, is used as a virtual camera to monitor the position of the laser pulse and synchrotron radiation relative to the position of the slit.* ***(Right)****: The remotely operational streak camera FESCA-200 installed in the tunnel.*

Figure 7.3: *The coarse longitudinal overlap setup installed in the container.*

7.2 Shielding for the electronic components

As was introduced in Chapter 3, relativistic electron bunches with energy of up to 1.2 GeV are produced in superconducting cavities in the FLASH tunnel. The ionizing gamma radiation is produced due to deceleration of those electrons by the surrounding atomic nuclei, a mechanism termed Bremsstrahlung. Single Event Upsets (SEU) initiated by gamma radiation can cause permanent damage to the electronics. Photo-neutrons are produced due to interaction with material by gamma radiation with energy above the threshold energy (E_{th}).

The fact that the interaction properties of the neutron are a function of its velocity has led to a terminology which is summarized as following:

- Thermal neutrons, which are in thermal equilibrium with surrounding have a most probable energy of 0.025 eV, and causing soft errors in the microelectronics.
- Slow neutrons, with energy less than 1 eV.
- Intermediate energy neutrons, with an energy from few hundred electron volts to about 0.5 MeV.
- Fast neutrons, with energies greater than 1 MeV

To protect the photo-detectors and other electronics used in the accelerator an appropriate combination of different materials should be used to attenuate the gamma rays and photo neutrons. For the gamma rays the most effective shielding barriers are those made of dense material containing atoms of high atomic number, including lead and concrete.

One should keep in mind that with the neutron shielding only slow neutrons can be easily captured. Thus the energy of fast neutrons should be first moderated. That can be accomplished by using sufficient thickness of material rich in hydrogen. In this way the fast neutrons will lose energy due to scattering collisions and approach thermal equilibrium. The shielding must also contain materials with high cross section for capturing the thermal neutrons after they are slowed down. Since the capture of thermal neutrons capture is a source of gamma radiation, one should use a high density material to attenuate the subsequent gamma radiation. Although not all of the radiation will be absorbed by the shielding, some leakage is unavoidable. The goal is to make this leakage as small as possible.

Due to space limitations in the FLASH tunnel a compact shielding scheme was required to attenuate the ionizing radiation below the damage threshold of the nearby electronic devices. The various modes of operation in the FLASH tunnel makes the shielding calculations based on Monte Carlo simulations inaccurate. The optimum photon shielding for selected materials was analytically calculated based on previous measurements for the linac area [MS08]. The station of the longitudinal overlap setup is installed 10 m after the energy collimator section. Several measurements were conducted from 2009 to 2011 to find the optimum thicknesses of selected materials for gamma and neutron attenuation.

7.2.1 Radiation measurement in the FLASH tunnel

For the measurement of the gamma and neutron radiation, thermo-luminescent detectors (TLD) were placed in the FLASH tunnel for a period of 2 weeks. The measurement was repeated for different shielding materials. TLD-600 (^{6}LiF, neutrons and gamma sensitive) and TLD-700 (^{7}LiF, gamma sensitive) were used in combination to estimate the amount of neutrons present.

Gamma attenuation factor for the lead and concrete breaks

In the measurement period of (02-16. Jun. 2009) the gamma transmission for concrete (thickness ∼ 10 cm) and lead shielding (thickness∼ 5 cm) was measured, Table. 7.1. Moderator cylinders were used around the TLDs to thermalize the fast neutrons for measuring the flux. The test setup placed in the tunnel is shown in Fig. 7.4.

	γ dose [mGy]	n_{fast} dose [mGy]
Without shielding	46.7±0.05	0.8±0.05
Lead-shielding (5 cm)	1.5±0.05	0.3±0.05
Concrete-shielding (10 cm)	14.8±0.05	0.3±0.05

Table 7.1: *Measured gamma dose after lead and concrete shielding.*

The measurement result shows more than 95% attenuation of gamma radiation for the 5 cm lead shielding and 70% attenuation for the 10 cm thick concrete shielding. The neutron attenuation of the lead and concrete layers is insignificant. Because of the space limitation and also to prevent neutron production in thick shielding material, lead was chosen as an appropriate gamma shielding material.

Measured thermal neutron transmission

In the measurement period (09-26. Jun. 2009) the transmission of Borated-Rubber

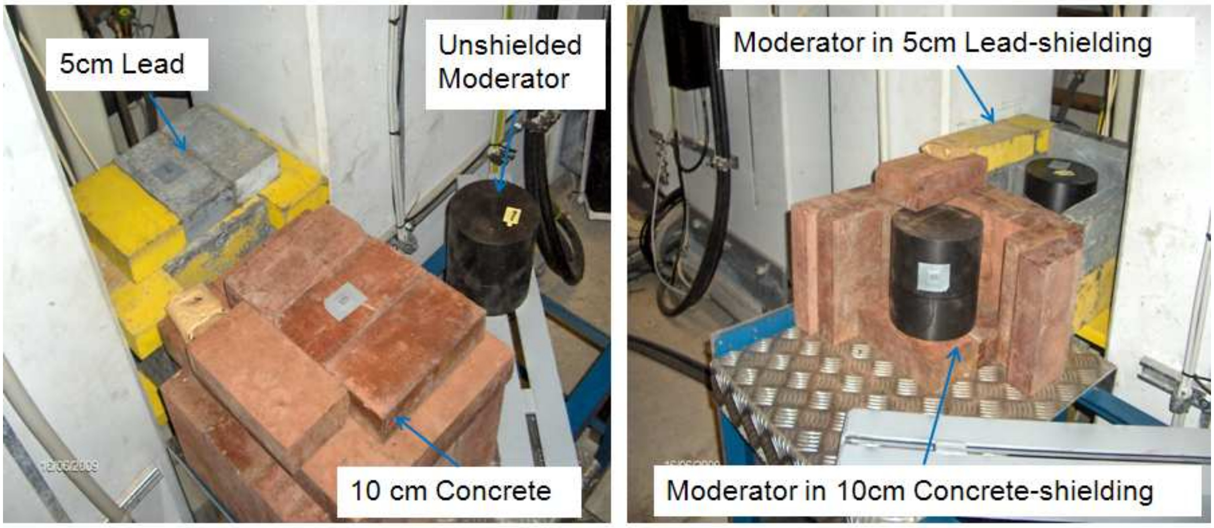

Figure 7.4: *The shielding test setup installed in the longitudinal overlap station, coordinate point 164 m in the FLASH tunnel.*

plates (6 mm thickness) for the thermal neutrons was measured. Two pairs of TLD cards (600 and 700) were used with and without shielding to estimate the amount of thermal neutrons generated at the longitudinal-overlap setup at 164 m in the FLASH tunnel. The moderator was not used in the measurement, therefore the contribution of the fast neutrons was minimized. The results of the measurement, summarized in Table. 7.2, shows that the thermal neutrons are blocked at more than a 99% level by Borated-Rubber. In contrast more than half of the gamma radiation would pass through the shielding thus showing the need for an appropriate gamma shielding material.

	γ Transmission[%]	n_{th} Transmission[%]
Without shielding	100	100
6 mm Borated-Rubber	55	0.8

Table 7.2: *Neutron transmission measured after 6 mm Borated-Rubber shielding. The gamma transmission for the 10 cm concrete breaks are also measured using TLD cards.*

Evaluated gamma and fast neutron doses for 10 years FLASH operation

The estimated gamma and neutron radiation at 164 m in the FLASH tunnel, for 500 working weeks, is summarized in Table. 7.3. According to the damage threshold determined for silicon based materials, [Muk11], one can see the estimated neutron kerma (kinetic energy released in matter) is insignificant. But contrary to the fast neutrons case, the Total Ionizing Dose (TID)-induced damage caused by gamma rays is detrimental to CCD cameras and other microelectronic devices. In this regard an appropriate attenuation for the gamma radiation and thermal neutrons which cause SEU errors is required.

	Measured dose [Gy]	Threshold in Silicon [Gy]
Fast neutrons	0.2±0.05	1
Thermal neutrons	0.12±0.05	-
Gamma radiation	11.7±0.05	10

Table 7.3: *The evaluated neutron and gamma dose for 500 working weeks of FLASH.*

Proposed shielding configuration

The optimum thickness for the lead material was chosen based on the photon transmission probability curves (with build up) shown in Fig. 7.5. A 20 mm thick lead plate would transmit 5% of the gamma radiation, which in our case means the estimated gamma radiation of 11.7 Gy would be attenuated down to about 0.6 Gy, which is approximately 16 times below the damage threshold of Silicon devices. To suppress the thermal neutron flux in the longitudinal overlap station, 15 mm Borated Polyethylene plates [Bp-11] were used in the inner layer of the shielding box. The 10% Boron content was chosen because of excellent attenuation of thermal neutrons and the reduction of the levels of capture-gamma radiation. Its hydrogen content makes it an effective shield for the fast neutrons. Depending on the initial energy of gamma radiation, in the hard lead plates ($Pb_{98}Sb_2$) additional neutrons may be generated which can be captured by the inner Polyethylene plates. The constructed container is shown in Fig. 7.6. The 20 mm lead plates [Roe11] are shown in gray and the 15 mm Borated Polyethylene plate are shown in green.

Measured radiation transmission through shielding-container in the FLASH tunnel

After the shut down of 2009, the longitudinal overlap set up was installed in a shielded container at 164 m of the FLASH tunnel. The proposed shielding-configuration should protect the expensive photo-detectors installed in the longitudinal overlap station against ionizing radiation. To check the functionality of the shielding plates, the gamma radiation and thermal neutrons inside and outside of the container were measured using the TLD-600 and TLD-700 dosimeters.

The result of two series of measurements, each for the period of about 2 weeks, is summarized in Table 7.4 and Table 7.5. During the above-mentioned periods the FLASH machine and its sub-components such as the sFLASH experiment, were commissioned.

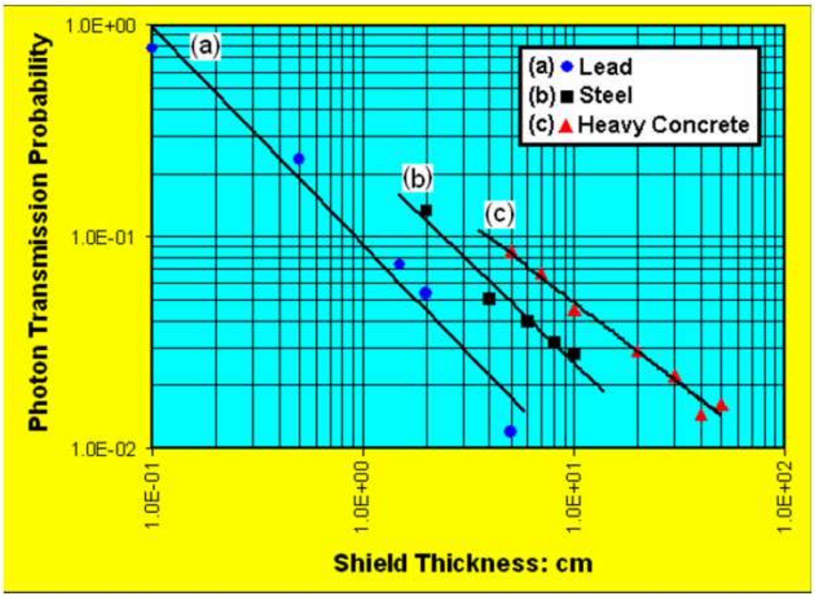

Figure 7.5: *Experimentally beam photon transmission probability curves for Lead, Carbon Steel and heavy concrete, adapted from Ref. [MS08].*

On average, the shielding transmits 5% to 20% of gamma radiation. Approximately 10% of the neutron flux is transmitted through the shielding. The measured dose inside the container is far below the damage threshold of the Silicon based material.

11-30.May.2010	γ dose [mGy]	n_{th} dose [μGy]	γ Transmission	n_{th} Transmission
Unshielded	24.8±0.05	73.3±0.05	100 %	100 %
Shielded (Nr.1)	5.3±0.05	6.39±0.05	21.4 %	8.7 %
Shielded (Nr.2)	4.2±0.05	6.98±0.05	16.9 %	9.5 %

Table 7.4: *Measured gamma radiation and neutron flux transmission, May-2010.*

1-15.Jun.2010	γ dose [mGy]	n_{th} dose [μGy]	γ Transmission	n_{th} Transmission
Unshielded	32.1±0.05	20.24±0.05	100 %	100 %
Shielded (Nr.1)	1.9±0.05	1.79±0.05	6.0 %	7.7 %
Shielded (Nr.2)	1.4±0.05	2.04±0.05	4.3 %	10.8 %

Table 7.5: *Measured gamma radiation and neutron flux transmission, Jun-2010.*

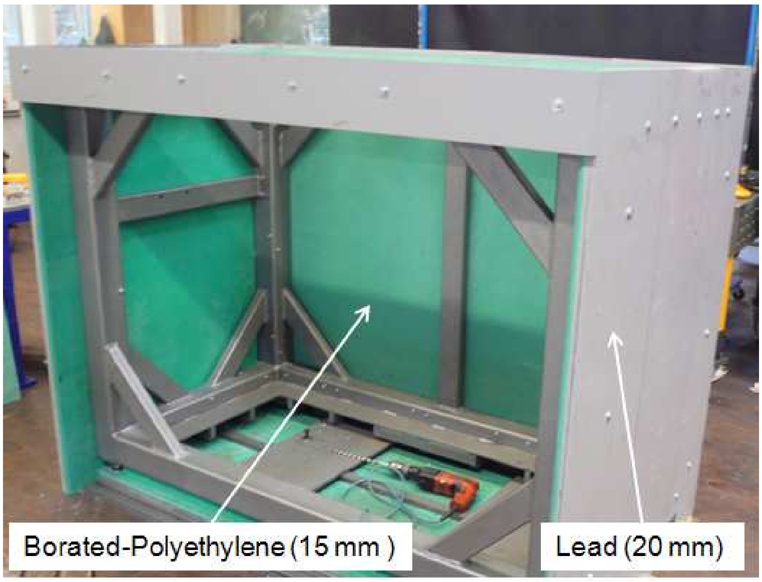

Figure 7.6: *The constructed shielding box to protect the electronics and photo detectors against neutron and gamma radiation. The gamma radiation would be attenuated with the 20 mm lead plates (in gray). The 15 mm Borated-Polyethylene plates (in green) in the inner side thermalize the fast neutrons and block the thermal neutrons.*

Comparative measurement of ionizing radiations around the shield-container

The amount of neutron and gamma radiation were measured using TLD-600 and TLD-700 on each side of the container, top (T), left(L), which is facing the electron beam direction and right(R), see Fig. 7.7. The evaluated data from each TLDs are shown in App E.

The measured gamma radiation and neutron flux transmission on each side of the container are summarized in Table. 7.6. The attenuation factor (μ) of lead plates (thickness of x=2 cm) is also calculated using the flux relation $\phi/\phi_0 = e^{-\mu x}$.

Location	n_{th} Transmission [%]	$\mu_{n_{th}}$ [cm^{-1}]	γ Transmission [%]	μ_γ [cm^{-1}]
Upstream	46.8	0.38	5.3	1.47
Top	6.1	1.4	14.1	0.98
Downstream	20.5	0.8	15	0.95

Table 7.6: *The result of gamma and neutron dosimetry around the shielding box which is located downstream of energy collimators in the FLASH tunnel. Gamma radiation detected outside of the container on the upstream side is 6 times more than the radiation in the downstream side of the container, $6\gamma_L \sim 3\gamma_T \sim \gamma_R$. The shielding shows more attenuation for the gamma radiation at the upstream side of the container, which is facing the electron beam direction.*

The neutron flux outside of the container, on the top and right side, is almost the same while it is 4 times more than what is detected with the TLDs installed at the left side, ($n_R \sim n_T \sim 4n_L$). But inside the container on the right side which is facing the electron beam direction more neutrons are detected in comparison with the top of the container. This shows that due to higher outer gamma radiation on the right side, additional neutrons are generated within the shielding. Gamma radiation detected outside of the container on right side is 6 times more than the radiation in the left side of the container, $6\gamma_L \sim 3\gamma_T \sim \gamma_R$. The shielding shows more attenuation for the gamma radiation at upstream side of the container, which faces the electron beam direction.

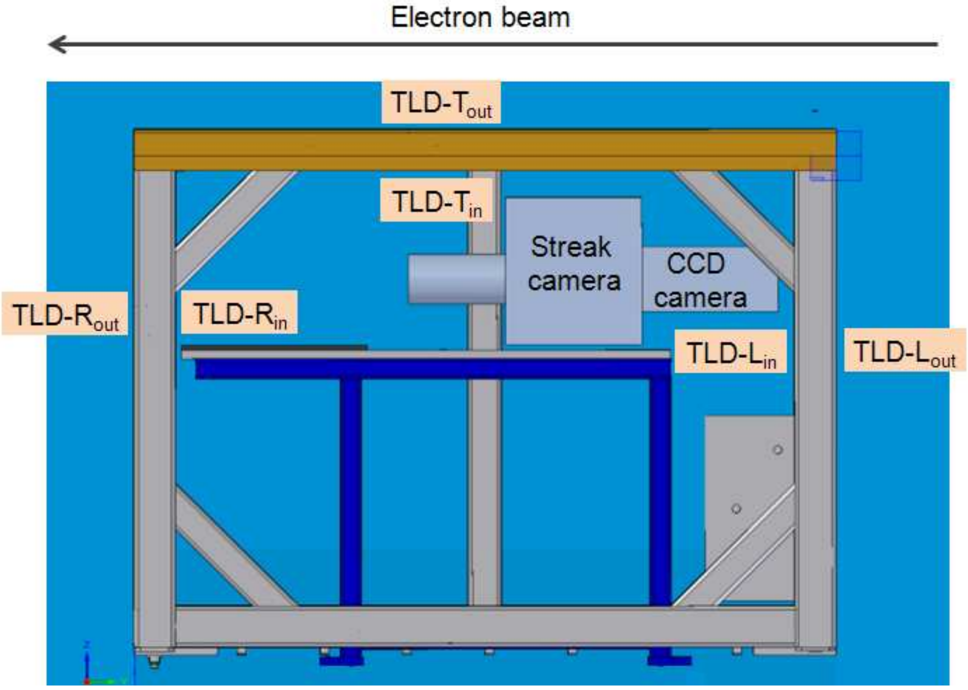

Figure 7.7: *Container side view and location of TLD pairs (600-700) in each side.*

8 Optimization of the beamline

Characterization of the types of radiation used for determining the longitudinal overlap between the XUV pulse and the electron bunch was discussed in section 4.5.3. In this section the energy of each of the pulses at the position of longitudinal overlap setup is estimated. In addition the minimum energy of the pulses which is needed for a correct measurement with the ST-camera is given. The appropriate attenuation of both radiation pulses by means of combination of different spectral filters is explained. Finally, the temporal dispersion of the beam line is analytically estimated and experimentally measured.

8.1 Intensity threshold for the streak camera

There are some lower and upper limits for the intensity of the incident light to the slit of the streak camera in order to obtain a valid measurement. Fig. 8.1 shows the general dynamic range behavior of a streak camera. The curve shows that at a very short pulse with a duration of a similar order of magnitude as the time resolution of the streak camera (i.e. a few hundred femtoseconds up to a few picoseconds in FESCA 200), if one slowly increases the input pulse energy the measured pulse width will stay constant within a certain range. but then suddenly starts to increase rapidly above a threshold energy. The latter phenomenon is caused by the (transverse and longitudinal) broadening of the packet of photo-electrons inside the streak tube due to space charge effects. Therefore in order to make a valid measurement, it is important to stay below this broadening limit [Ham10].

Upper limit The rough estimate for the upper limit in a usable light signal is 60000 photons per pulse ($\approx 15\,\mathrm{fJ}$) which corresponds to a time resolution of 600 fs for the wavelength of $\lambda = 800\,\mathrm{nm}$, see Fig. 8.1(b). This number depends on how the pulse is dispersed horizontally, since the space-charge effect depends on the volume-density of the electrons. If the beam is focused on a horizontally smaller area, the total number of electrons in the pulse before the occurrence of broadening will be smaller. Therefore in order to exploit the dynamic range of the streak camera at its best, it is always good to arrange the optics in front of the streak camera in such a way that the entire cathode will be most evenly illuminated along the horizontal axis. The cathode size of the FESCA-200 is 3 mm.

Lower Limit The streak system can be operated in such a way that almost every electron that is amplified in the MCP will be seen as a bright spot on the CCD image (i.e. the spot is much brighter than the noise level of the CCD camera). For that the MCP should be tuned to a medium or high level. Thus it is sufficient to consider only system elements before the MCP to determine that the following items will have impact on the intensity of the incident beam [Den09]:

- The optical setup in front of the streak optics
- The streak camera optics, which are three things to consider:
  1. Input slit: The slit should be narrower than the beam size
  2. Aperture: the F-number of the input optics is roughly 5.0 (The F number is defined as the ratio of the focal length to the lens diameter.), so the input optic should be chosen in a way that the input angle does not exceed the inverse of the F number.
  3. Absorption: In the spectral range between 250 nm and 400 nm the efficiency within the optics is 50-70% .
- Quantum efficiency (Q.E): The Q.E. of the cathode (S20) is approximately 10% at its spectral maximum, which is near 500 nm. The Q.E of the photocathode for 800 nm is about 0.5%.
- Electron losses inside the tube: is about 40%.
- After MCP: All effects after the MCP (i.e. the combined behavior of phosphor screen, output optics, MCP, CCD, etc.) are not important, as stated above, and so this overall efficiency can be assumed to be 100%.

Assuming no losses at the slit or by aperture, an efficiency of 50% inside the streak tube and a photon wavelength of 800 nm, one needs (in the statistical average) approximately 4×10^5 photons ($\approx 0.1\,\mathrm{pJ}$) in order to have a measurement with 200 fs resolution.

To check the sensitivity of the FESCA-200, the 800 nm laser with initial energy of 30 mJ was used. According to the measurement the damage threshold of the incident light is $\geq$ 5 nJ. An energy more than this threshold can cause some damage to the photocathode.

Operation at high energies will, even before damaging the photocathode also broaden the pulse due to the space charge, thus reducing the accuracy of the measurement. For this reason, in the experiment the NIR laser pulse was observed firstly using a virtual camera.

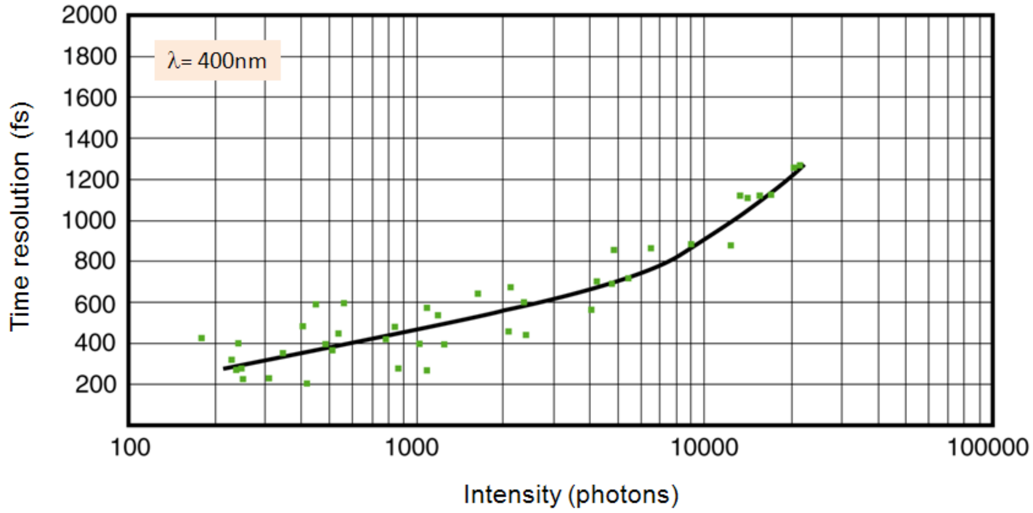

(a) *Dynamic range of FESCA200 for the incident light with 400 nm wavelength.*

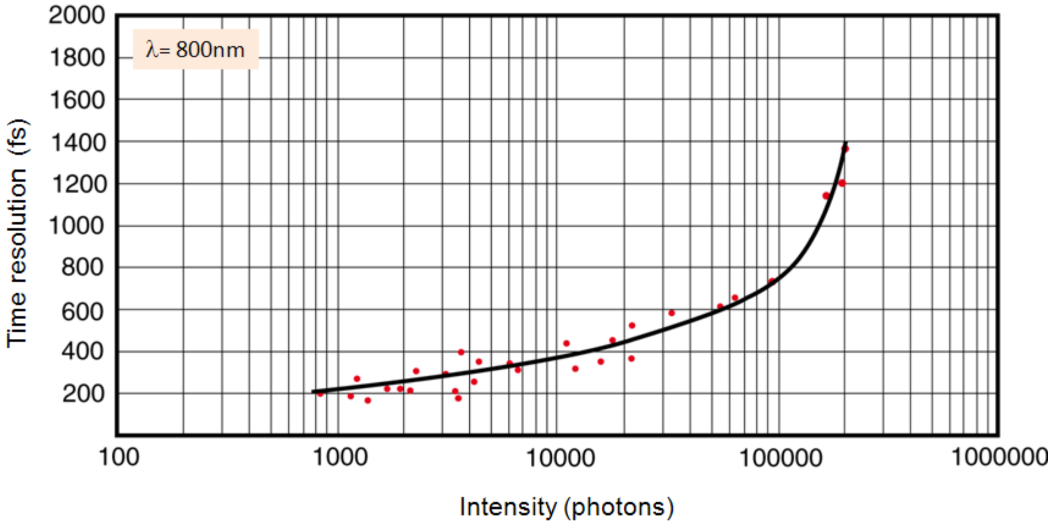

(b) *Dynamic range of FESCA200 for the incident light with 800 nm wavelength. Minimum 1000 photons is needed to observe the image on the CCD with the resolution about 200 fs.*

Figure 8.1: *The dynamic range of a typical streak camera. For a short pulse with a duration in the similar order of the resolution of the streak camera, by increasing the energy of the input pulse the pulse width will remain the same for a certain range but then starts to increase rapidly. The photoelectrons spread spatially along the streak tube as the wavelength becomes shorter, adapted from [Ham10].*

8.2 Transmission of the transport beamline

Seed drive laser As explained in section 4.3, the seed pulse and the drive laser are coupled together to the electron beamline using a single grazing incidence mirror (at 13.9 °) and a mirror triplet (at 14.1 °). The grazing mirrors substrates are coated with TiB_4C for 38 nm wavelength and B_4C+Mo for 13 nm wavelength. To provide an estimate of the energy of the laser in longitudinal overlap setup the reflectivity of these mirrors for the drive laser (λ=800 nm with 30 mJ energy at HHG source) is measured. The 1$''$ mirror used in this measurement has a B_4C coating on one half and a B_4C+Mo on the other half. To measure the energy for different polarizations of the laser, a half wavelength-plate and a polarizer were used together. First the upper part of the mirror with the B_4C coating was exposed with the laser pulses and later the other half was illuminated. The result of the measurement is shown in Fig. 8.2.

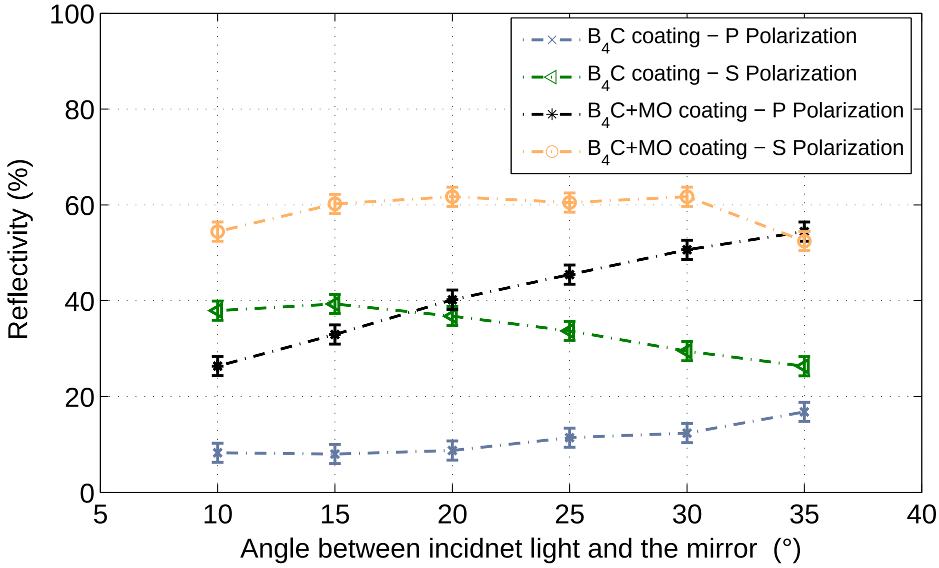

Figure 8.2: *Reflectivity of the grazing incidence mirror with different coatings for the seed drive laser (λ =800 nm). Here the s and p polarizations are defined as the field components parallel and perpendicular to the optical table.*

For the the fully S-polarized incident light with an incident angle of 14 ° the $(B_4C + Mo)$ coating is the most reflective (≈58%) for the 800 nm laser. Therefore this coating can be used to transport more power to the (MOR) setup thus increasing the modulating amplitude of the electron beam. Of course due to the three-dimensional geometry of the transport beam line, the light is not fully S-polarized.

The B_4C coating is used in our commissioning shifts for the seeding at 38 nm wavelength. The reflectivity of this coating for the NIR laser light with an incident angle of 14 ° varies between 8% to 39% depending on the polarization of the laser, see Fig. 8.2. For a fully S-polarized laser beam, the initial energy of the laser after 4 grazing incidence mirrors will attenuate by a factor of 2.4×10^{-2}. It means the energy of the laser (22 mJ), after reflection from four grazing incidence mirrors drops down to $\approx 530\,\mu J$. For a fully P-polarized light the attenuation factor is 4.1×10^{-5}, and in this scenario the initial energy drops down to $0.9\,\mu J$. To attenuate the energy of the beam to below the damage threshold of the streak camera ($\approx 1\,nJ$), the energy of the beam should be attenuated roughly by about 10^3 for the fully P-polarized case and by a factor of 10^6 for fully S-polarized light. According to the results of the NIR laser beam-propagation through the seeding beamline, using ZEMAX software, transmission of the beam line for the NIR laser beam is estimated to be 2.85×10^{-3}, see App D. That means the initial energy of the NIR laser (22 mJ) drops down to 188 μJ which is closer to the measured transmitted energy for the fully s-polarized light. In Table. 8.1 the effect of other parameters on the final transported energy of the seed drive laser from the source to the longitudinal overlap setup is summarized.

Effect	Value
Reflectivity of Si/Sc mirror at 88° incidence angle ($R_s = R_p$)	28%
Reflectivity of Mo/Sc mirror ($R_s = R_p$)	39%
Transport efficiency due to $1''$ mirror	50%
Clipping of the laser due to screen size (38 mm)	–
Coupling efficiency to the streak camera slit (30 μm × 15 mm)	8%

Table 8.1: *Efficiency of the transport beam line for the seed drive laser from the source to the longitudinal overlap setup.*

Taking into account the 28% reflectivity for the Si/Sc mirror and 50% transmission due to the mirror size, the energy of the NIR pulse drops to $\sim 74\,\mu$J and to $\sim 0.1\,\mu$J for the fully S-polarized and fully P-polarized pulse, respectively. The energy of the laser is measured to be $\sim$ ($50 \pm 5\,\mu$J) on the first optical table after the screen.

Synchrotron radiation of the modulator As was explained previously, the synchrotron radiation due to the modulator undulator upstream of the seeding undulators is used as a reference for the arrival time of the electron beam. In the experiment the modulator was tuned to 800 nm wavelength for on-axis screen operation and at 1300 nm wavelength for the off-axis scenario. In the latter case second harmonics of the fundamental wavelength will be reflected by an off-axis screen to the streak camera station. Operation with an off-axis screen is required for parasitic measurement of the temporal overlap during the seeding experiment, otherwise the XUV pulses will be blocked by the screen.

An analytical simulation has been performed using the SRW code [CE98] to estimate the energy of the modulator-undulator (1 m, 5 periods, λ_u =200 mm), with more detailed information given in Table. 3.1. The electron beam energy is assumed to be 700 MeV. The resonance wavelength of the undulator is 1300 nm. The radiation is measured on a screen (22 mm × 28 mm) which is located 2.58 m from the middle of the undulator. The energy integrated over the entire spectrum is estimated to be 0.29 nJ. The spectrum of the modulator taken from the simulation is plotted in Fig. 8.3(a). To compare the simulation result with the measurement, the spectrum of the modulator is recorded with the VIS-NIR spectrometer, as shown in Fig. 8.3(b). In the experiment the energy of the electron beam was tuned to 663 MeV. For the protection of the spectrometer a neutral density filter (OD=0.2) was used. As shown, the result of the measurement is not identical with the simulation result. Because of that the amount of energy of the radiation can not be well estimated with the simulation.

The energy of synchrotron radiation of the radiator undulator in the MOR setup was measured using a Joule-meter which includes a silicon detector (diameter ≈ 11 mm), [J3S11]. The principle of operation of this Joule-meter is that photons of incoming light interact with the molecules of the silicon detector and generate a signal current. This signal is electrically integrated by the capacitance of the amplifier and yields a pulsed voltage which is directly proportional to the actual pulse energy [J3S11].

In another measurement the electron beam with energy of 982 MeV was steered around a 30 mm screen. The energy per pulse of the synchrotron radiation at different resonance wavelengths of the undulator was recorded using the Joule-meter. The relative spectral response of the Joule-meter together with the actual energies are summarized in Table. 8.2.

Resonance undulator wavelength	Mean energy (measurement)	Spectral response (relative to 1)	Actual energy (min threshold)
800 nm	12.8 nJ ± 1.6 nJ	0.95	13.5 nJ ± 1.6 nJ
700 nm	16.4 nJ ± 1.3 nJ	0.85	19.3 nJ ± 1.3 nJ
600 nm	19.4 nJ ± 0.9 nJ	0.7	27.7 nJ ± 0.9 nJ
500 nm	22.0 nJ ± 0.6 nJ	0.4	55.0 nJ± 0.6 nJ

Table 8.2: *Measured energies of the synchrotron radiation of the radiator.*

A homogeneous energy distribution is assumed over the visible spectral range, which gives the minimum detection threshold for the energy of the synchrotron radiation. For example the difference between the seed-drive laser energy (≈100 μJ) and synchrotron radiation at the same wavelength (≈13 nJ) is in the order of 10^4.

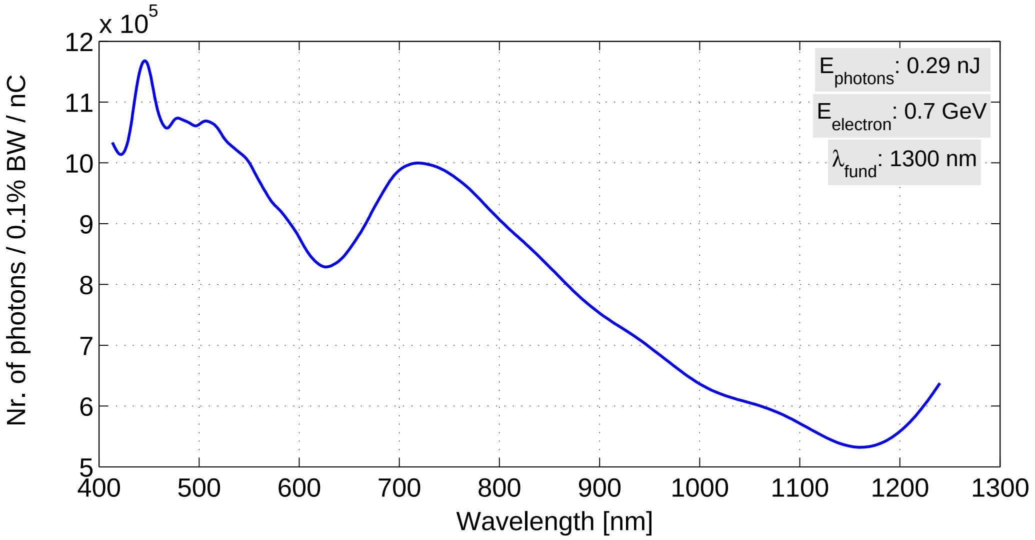

(a) *Taken from simulation using SRW code.*

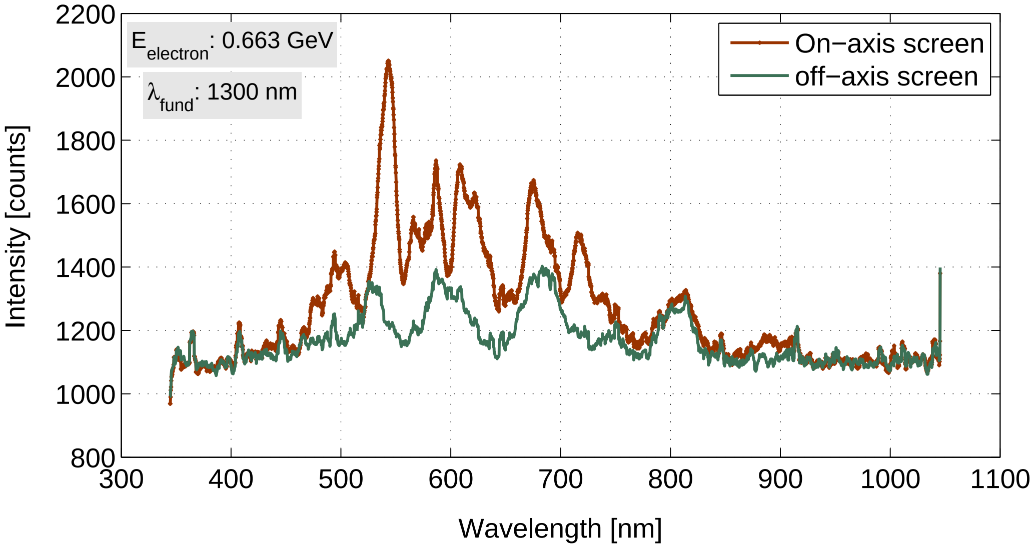

(b) *Measurement using a NIR-VIS spectrometer.*

Figure 8.3: *The spectrum of the modulator/radiator undulator, with the period of* λ_u=*200 mm over 1 m.*

8.3 Beam intensity control using combinations of spectral filters

Measurement in the lab Due to different initial energies of the laser and synchrotron light, different attenuation factors are needed for each of those pulses within the same beam line. The transmission of some spectral filters with different bandwidth was measured in the lab using the laser oscillator pulses (63 mJ), which was attenuated to 0.3 mJ using a wedge with 4% transmission. A neutral density (ND) filter with optical density (OD)=4.4 was used to further attenuate the energy of the beam below the damage threshold of the Joule-meter. Another ND filter (OD)=3 was used to increase the signal to noise ratio, with the noise arising from the stray light existing in the lab. The OD gives the amount of light which is blocked by the filter (OD=-$\log_{10}$(T), where T the transmission) [ND-11]. After the ND filters the laser beam, with energy of (5.0 nJ± 0.1 nJ), passed through the selected bandpass (BP)-filter and was focused to the head of the Joule-meter using a lens with focal length of 50 mm. The transmitted energies of the laser through different spectral filters are listed in Table. 8.3.

Filter type	Measured Energy
700 nm ± $(80\,\mathrm{nm})_{fwhm}$	70.0 pJ ± 2.0 pJ
550 nm ± $(80\,\mathrm{nm})_{fwhm}$	16.0 pJ ± 4.0 pJ
600 nm ± $(10\,\mathrm{nm})_{fwhm}$	12.0 pJ ± 0.2 pJ
500 nm ± $(40\,\mathrm{nm})_{fwhm}$	4.5 pJ ± 0.1 pJ
670 nm ± $(3\,\mathrm{nm})_{fwhm}$	1.4 pJ ± 0.1 pJ

Table 8.3: *Measured attenuation of the seed-drive laser oscillator for different spectral filters with different bandwidth.*

The BP-filter with 700 nm central wavelength attenuates energy of the laser pulse by a factor of 71. The BP-filters with shorter central wavelength attenuate the energy more, but this is achieved at the cost of increasing dispersion in the beam line. The spectrum of synchrotron radiation of the short undulator used for the measurement includes enhanced energies in higher harmonics which can be sent to the streak camera together with the fundamental wavelength ($\lambda = 800\,nm$). The dispersion due to the input optics of the camera causes a delay in the arrival time of the electron bunch relative to the laser pulse ($\lambda_L = 800\,nm$), which should be excluded from the real temporal offset between pulses. To avoid this effect and keeping the dispersion effect below the typical resolution of the streak camera (300 fs) the BP-filters with wavelength shorter than 650 nm are not used for the attenuation.

The measured attenuation of the laser-oscillator beam for different ND filters are listed in Table. 8.4. These filters can be used to further attenuate or block the laser light. The disadvantage of these filters is that, due to large attenuation, the synchrotron radiation which is about 4 orders of magnitude lower in energy than the laser pulse, can be barely detected.

Optical density (OD)	Measured Energy
0.5	2.0 nJ± 0.1 nJ
2.0	200 pJ± 10 pJ
4.0	8.5 pJ± 0.2 pJ

Table 8.4: *Measured attenuation of the seed-drive laser oscillator for different neutral density filters. Energy of the laser pulse before the filters is (5.0 nJ± 0.1 nJ).*

Analytical consideration To estimate the transmitted energy of the laser pulses through different B-filters, two normal Gaussian distributions are defined, which one of them defines the seed-drive laser (y_L) and the other one (y_F) the transmission curve of the selected BP-filters:

$$y_L = A\frac{1}{\sqrt{2\pi\sigma_L^2}}e^{\frac{-(\lambda_L-\lambda_{L0})^2}{2\sigma_L^2}}, (A = 1, \lambda_{L0} = 800\,nm, \sigma_L = (30\,nm)_{\text{fwhm}})$$

$$y_F = B\frac{1}{\sqrt{2\pi\sigma_F^2}}e^{\frac{-(\lambda_F-\lambda_{F0})^2}{2\sigma_F^2}}, (B = 0.65, \sigma_F = (80\,nm)_{\text{fwhm}})$$

The integration over the product of these two functions defines the transmitted energy through the filter. The initial energy of the laser is assumed to be 5 nJ, identical to the energy used for the measurement in the lab. In Table. 8.5 the transmission factors and output energies for three BP-filters with different central wavelengths, λ_{F0}, are listed.

The attenuation factors for the estimated energies of the laser pulse and synchrotron radiation in the longitudinal overlap setup are listed in Table. 8.6.

The energy of the laser after filtering is still above the damage threshold of the streak camera. For further attenuation of the laser pulses short-pass filters can be used together with the above-mentioned bandpass filters. The short-pass filter has more than 90% transmission for the wavelengths shorter than its cut-off wavelength. As an example the short-pass

BP-filter	Transmission [%]	Transmitted energy [pJ]
$650\,\mathrm{nm} \pm (80\,\mathrm{nm})_{fwhm}$	0.01	0.6
$700\,\mathrm{nm} \pm (80\,\mathrm{nm})_{fwhm}$	1.4	68.2
$750\,\mathrm{nm} \pm (80\,\mathrm{nm})_{fwhm}$	23.5	1200
$800\,\mathrm{nm} \pm (80\,\mathrm{nm})_{fwhm}$	61	3000

Table 8.5: *Analytical estimation on the transmitted energy of the laser after different filters. The initial energy of the laser pulse before the filters is assumed to be 5.0 nJ.*

Filters used (BW=80 nm_{fwhm})	λ_0 =650 nm	λ_0 =700 nm	λ_0 =800 nm
Initial Energy		Minimum transmitted energy	
$E_{SR} \geq 13\,\mathrm{nJ}(@800\,\mathrm{nm})$	1.5 pJ	177 pJ	8 nJ
$E_{SR} \geq 27\,\mathrm{nJ}(@600\,\mathrm{nm})$	3.2 pJ	368 pJ	16.4 nJ
$E_L \approx 100\,\mu\mathrm{J}$	12 nJ	$1.4\,\mu$J	$61\,\mu$J

Table 8.6: *The estimated energies of the seed-drive laser and synchrotron radiation after different bandpass filters.*

filter with the cut-off wavelength at 700 nm is more than 85% transmissive for the wavelength range between 400 nm to 680 nm, and 1% transmissive for the wavelength range of 720 nm-800 nm [edm11b]. Another useful example is the Schott BG39-filter [Sch11a], which attenuates the wavelength range between 770 nm-1000 nm by 5 orders of magnitude. The transmission of this filter at 700 nm is about 1% and at 650 nm is 13%. This is the motivation to tune the modulator-undulator at different resonance wavelength rather than the seed drive laser. In this way the laser pulse can be attenuated by higher orders of magnitude. In this process the use of spectral filters in the beam line is mandatory. As discussed, the spectrum of the short modulator contains higher harmonics which can be transported to the streak camera. To minimize the dispersion one needs to limit the bandwidth of incoming light.

Measurement in the tunnel During the commissioning shifts various combination of spectral and edge filters were used to find the optimized energy for the laser pulse and synchrotron radiation. Depending on the resonance wavelength of the modulator-undulator the best attenuation for the seed-drive laser (λ_L=800 nm) and synchrotron radiation (λ_{SR}=800 nm or 1300 nm) was achieved using one of the following combinations:

- BP-filter (λ_0 =800 nm ± 80 nm) + Schott BG39, $E_L^{est.} \approx 0.6\,pJ$

- BP-filter (λ_0 =700 nm ± 80 nm) + SP-filter (λ_{cutoff}) =700 nm, $E_L^{est.} \approx 100\,pJ$
- BP-filter (λ_0 =650 nm ± 80 nm) + SP-filter (λ_{cutoff}) =725 nm, $E_L^{est.} \approx 1\,pJ$

Here $E_L^{est.}$ is the estimated energy of the NIR drive laser after the attenuation. The energy of the NIR laser is assumed to be 50 μJ before the above-mentioned filters.

8.4 Dispersion of the longitudinal overlap beam line.

The reflected beams from the in-vacuum screen pass through a glass window and traverse the beam line over 4 m on air to reach to the photo-detectors station. The beams also pass through two filters which have 1-5 mm thickness. The lenses which are used in the input optic of the streak-camera itself are made of CaF_2 and SiO_2 material with the thickness of 24.4 mm and 3.6 mm respectively. In addition the beams pass through another lens which is installed in the beam line to focus the light into the slit of the camera. The dispersion of the wavelengths in range of 200 nm to 800 nm through different materials is shown in Fig. 8.4. In case the undulator is not tuned to the same wavelength as the seed drive laser, the passage time of two beams (dispersion) through the beam line will differ due to difference in their group velocity, see App F. The dispersion effects due to spectral filters, focusing lens to the slit of the camera and air (the beam line is not in-vacuum) are presented in Fig. 8.5.

In one case that the undulator was tuned to 800 nm and the out-coupling screen was place off axis, and higher harmonics were sent to the streak camera together with the IR laser (800 nm), the temporal dispersion of about 3.5 ps was observed, which is consistent with the analytical estimate.

8.5 Effect of the path difference in arrival time

According to Table. 4.2 and Table. 4.3, different divergences ($\theta = M^2 \frac{\lambda}{\pi w_0}$) of NIR laser and HHG pulse can be translated to different arrival times for the points away from the focal position. In our case the radiation for $\theta \geq 1$ mrad can not be transported in the beamline due to the size of the mirrors. Using the ZEMAX simulation code [zem11], the difference in arrival time between the central part of the radiation and the outer part (with $\theta \sim$1 mrad at the longitudinal overlap station) is estimated to be about 5.3×10^{-18} second for the 800 nm and 7.4×10^{-18} seconds for the 38 nm radiation. In both cases, the temporal difference is far below the resolution of our longitudinal profile measurement tools.

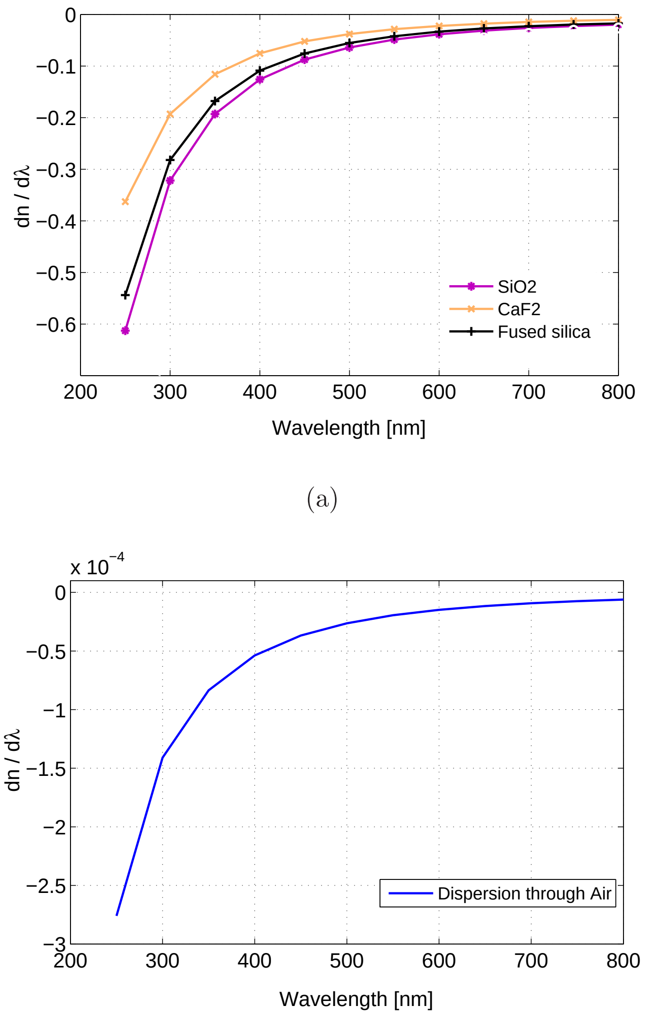

(a)

(b)

Figure 8.4: *Dispersion curve through different materials used in the optical beam line.*

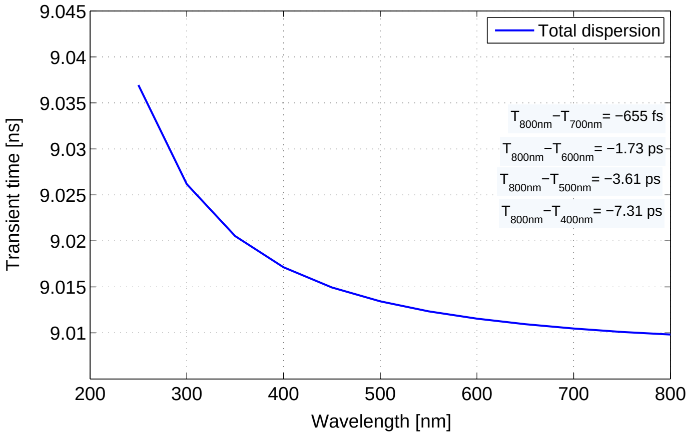

Figure 8.5: *Total Dispersion of the beam line.*

9 Measurement results

During the shifts which were dedicated for the seeding experiment at FLASH, all relevant diagnostic systems were commissioned. To enable the seeding experiment, a stepwise procedure for achieving the six-dimensional phase space overlap between electron bunch and seed pulse (x, x',y ,y' ,t ,Energy), was performed as follows:

- Standard machine operation to achieve SASE in the FLASH main undulator
- Setting the gap of the seeding undulators for the seeding wavelength of ($\lambda = 38.5\,\mathrm{nm}$) according to the calibration curve
- Measuring the HHG spectrum in the extraction beam line spectrometer
- Spectral overlap of seed pulse and sFLASH SASE radiation
- Transverse and angular overlap of the XUV pulse and electron bunch before and after each undulator section [Böd11]
- Coarse and fine temporal overlap between NIR laser pulse and electron bunch
- Scan procedures for the temporal overlap between XUV pulse and electron bunch
- Post processing of seeding stored data

The results and tolerances of spectral and transverse overlap were presented in Chapter 4. In this chapter the results of coarse and fine longitudinal overlap measurements, and the applied on-line methods to find the seeded signal are discussed. The post processing of stored data to demonstrate seeding at 38.5 nm is also presented.

9.1 Coarse longitudinal overlap measurement

To perform the coarse temporal overlap measurement the incoherent synchrotron radiation of the modulator, together with the NIR laser pulse is sent to the photo-detectors by using an off-axis screen. This screen is located after the modulator of the ORS experiment, as was explained in previous chapters. The off-axis screen makes the temporal overlap measurement and the seeding experiment to proceed in parallel. In this scheme the electron beam and XUV pulse propagate in the nominal axis to the extraction beam line. After proper attenuation an optical element splits the pulses of interest and sends them to the photomultiplier tube and slit of the streak camera, which are both located at the same distance from the beam splitter. It has been previously explained that the slit size impacts also the resolution of the measurement. The optimum slit size for this experiment was about 30 μm. The spatial positions of the electron bunch and NIR pulse were observed in the ′focus′ mode of operation of the streak camera, which permits observation of the optical signals input to the camera without streaking. Afterwards the following procedures were performed remotely to find the coarse temporal overlap in the ′operation′ (streaking) mode:

- To setup the relative timing of the electron bunch relative to the streak trigger:
  Typically the electron bunch should be about 30 ns after the edge of the trigger. This includes delays due the length of cables that transport the signals as well as the response times of the electronics.

- To find the electron bunch within the largest streak camera time range, which is 500 ps:
  The precise delay for the trigger signal relative to the electron bunch arrival time was set using the delay generator.

- To optimize the temporal overlap within 500 ps time range of the streak camera:
  The NIR laser pulse was shifted towards the electron bunch using a vector modulator by steps of less than 500 ps.

- The last step for the other streak camera time ranges (200 ps, 100 ps, 50 ps, 20 ps).
  Due to internal pulse-to-pulse jitter of the streak camera, which is in the order of 20 ps, the on-line temporal overlap utilizing the shortest time range was not possible.

The results of a typical longitudinal overlap measurement between pulses of interest is shown in Fig. 9.1. The red-dashed line in Fig. 9.1(c) shows a two-Gaussian fit model on the measured data. The peak-to-peak temporal difference is measured about 1.17 ps. Afterwards the NIR laser pulse was shifted towards the electron bunch using a 100 fs step size until the full overlap was achieved.

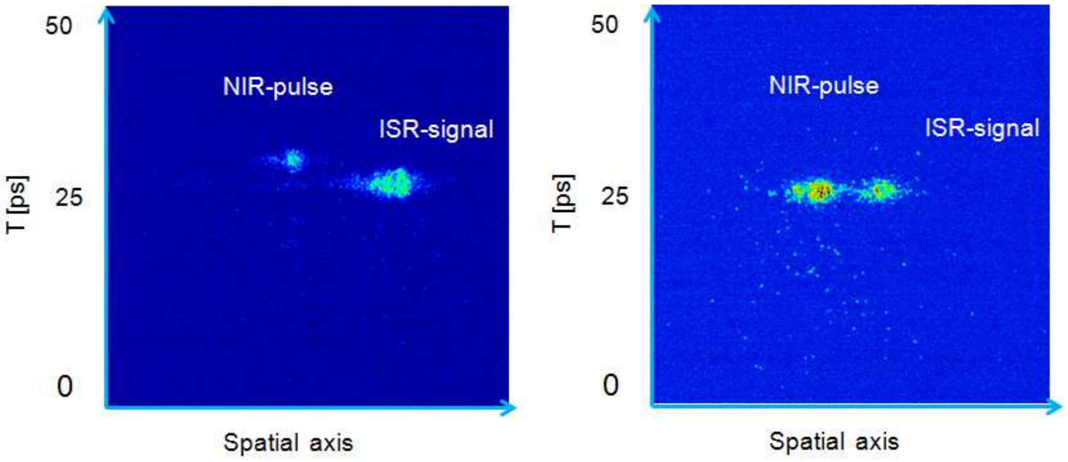

(a) *Streak camera image, different arrival times.* (b) *Streak camera image, full overlap achieved.*

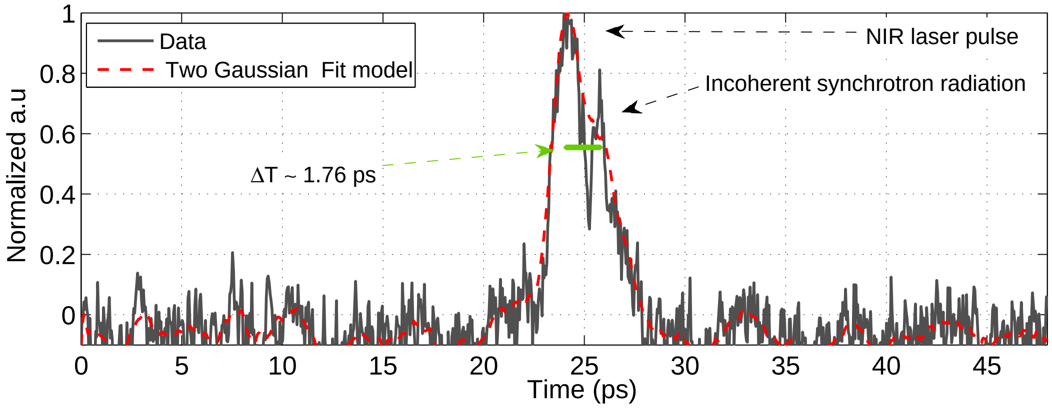

(c) *Temporal difference between the NIR laser pulse (in left) and incoherent synchrotron radiation of the undulator (right). The red-dashed line shows a two-Gaussian fit model to the measured data. The peak-to-peak temporal difference is measured to be* $\Delta T \sim 1.17\,ps$.

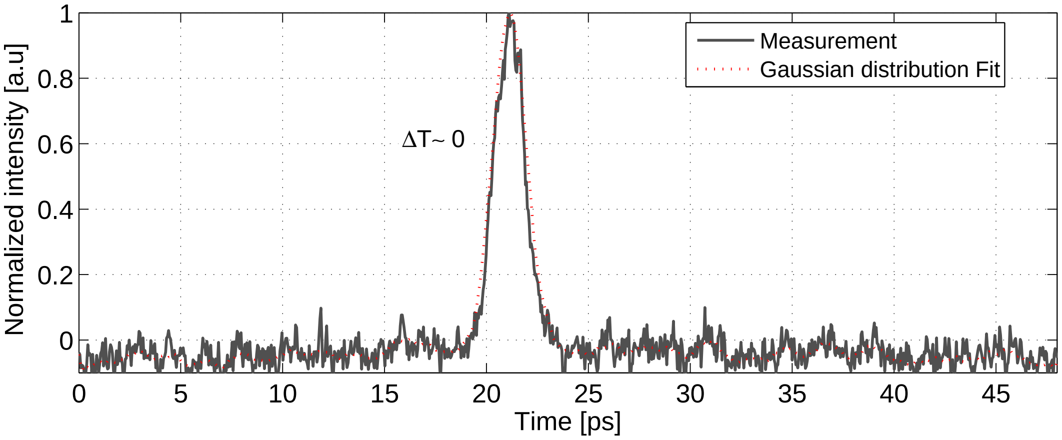

(d) *Temporal overlap between two pulses was achieved better than 1 ps resolution,* $\Delta T \leq 1\,ps$

Figure 9.1: *Measured longitudinal overlap between seed drive laser and electron bunch using the streak camera. The time range of the streak camera was set to 50 ps. The red-dashed line shows the Gaussian fit model on the measured data.*

To estimate the resolution of the measurement the following approach was adopted. First, the two signal pulses were separated by about 12 ps. Then, using the vector modulator, the NIR laser pulse was moved towards the electron bunch with a 2 ps time steps, see Fig. 9.2. Again the measured data was fit to a two-Gaussian model. The peak-to-peak temporal difference of some of the measurements are shown in the same figure.

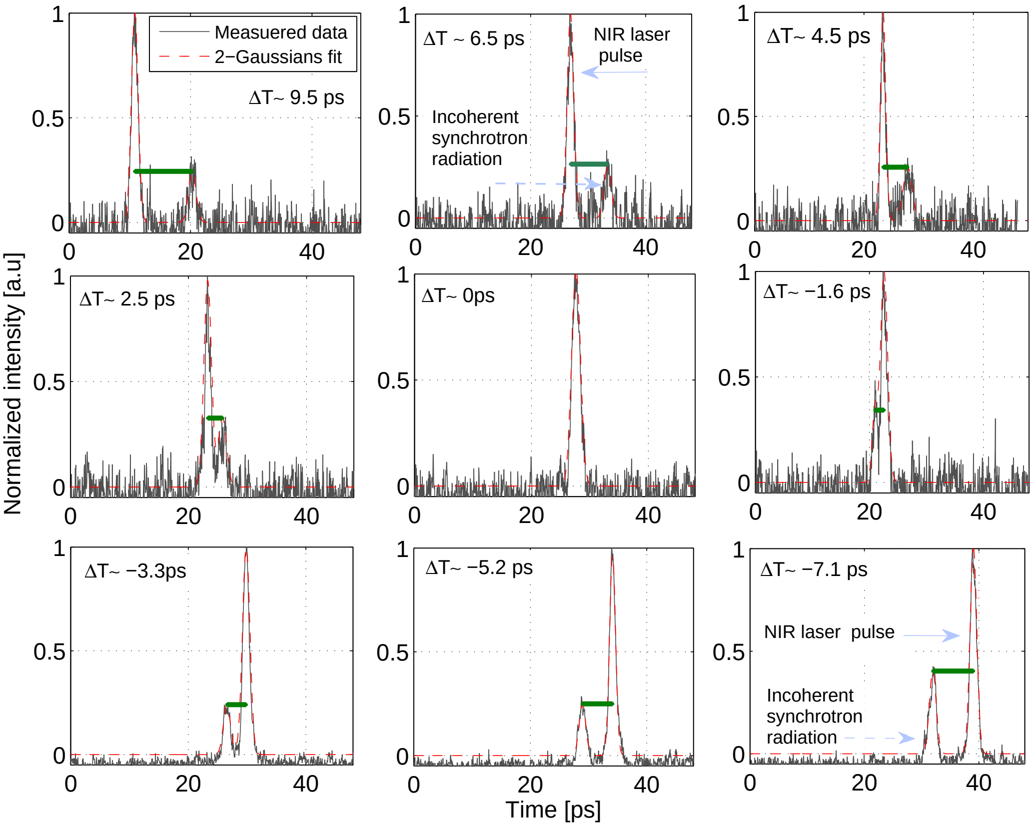

Figure 9.2: *Temporal scan. Two pulses were separated initially by more than 10 ps. Using the vector modulator the NIR laser pulse was shifted towards the electron bunch with about 2 ps time step. In each step 20 measurements were recorded. The red dashed line shows the two-Gaussian fit model. The peak to peak temporal difference is shown with a green line.*

The measured temporal differences (ΔT) versus the phases of the vector modulator are plotted in Fig. 9.3.

Using a linear regression approach [P^{+}88], the relationship between the resolution of the measurement and measured data (ΔT) can be derived. Here the model is a linear polynomial ($\Delta T = c + m\Delta\phi$). The derived values are approximately c =-21.9 ps and m =-127 rad. Using error propagation, the variances in estimation of those parameters σ_c =0.11 and σ_m =3.3 yields:

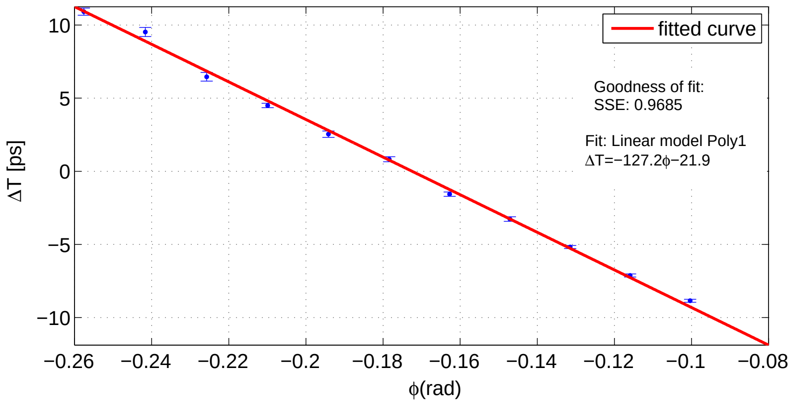

Figure 9.3: *The phase scan of the vector modulator (Φ) and the relative temporal offset ($\Delta\,T$) between seed pulse and electron bunch.*

$$\begin{aligned}\Delta\phi &= \phi_0\sqrt{(\frac{\sigma_c}{c})^2 + (\frac{\sigma_m}{m})^2 + 2\frac{\sigma_m}{m}\frac{\sigma_c}{c} * \rho_c} && (9.1)\\ &= -54\cdot 10^{-4}\,\mathrm{rad} && (9.2)\end{aligned}$$

where ρ_c is the correlation term [P$^+$88], and $\phi_0 = -a/b = -0.17\,\mathrm{rad}$ is the phase where two pulses are fully overlapped (ΔT =0). The resolution of the measurement for the phase of the RF at 1.3 GHz can be estimated of:

$$\begin{aligned}Resolution &= \frac{\Delta\phi}{1.3\cdot 10^9\cdot 2\pi} && (9.3)\\ &\sim 656\,\mathrm{fs} && (9.4)\end{aligned}$$

An on-line measurement with this resolution can not be obtained due to the internal jitter of the streak camera.

Relative pulse jitter measurement

The relative jitter of the electron bunch and seed pulse were measured during the commissioning shift on 15.11.2010. For this measurement 161 pulses were recorded, see Fig. 9.4. The measurement shows a standard deviation of about σ =300 fs. The reason of this big jitter can be either the NIR seed drive laser fluctuation or the energy jitter in the first accelerating module. Unfortunately the energy fluctuation during the time of the scanning was not recorded. The jitter can also be related to the systematic measurement jitter mentioned above, where, due to inherent noisiness of the streak, the relative timing between two signals are not recorded accurately. The beam arrival time has been established meanwhile to about 70 fs.

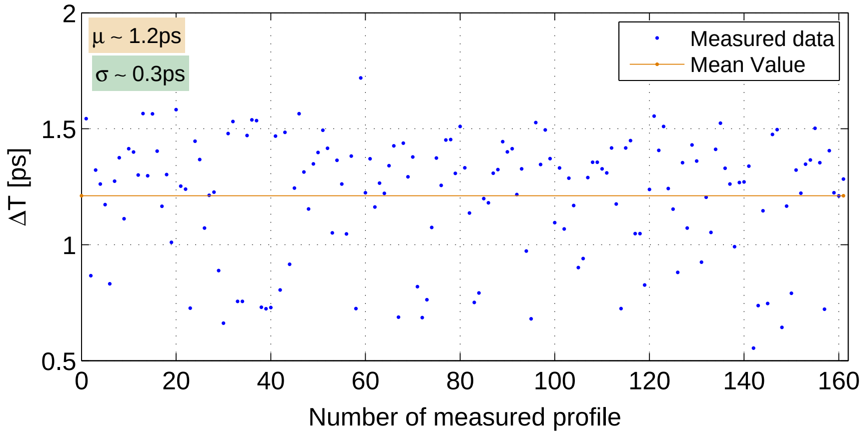

Figure 9.4: *Relative jitter between seed drive laser and the electron bunch.*

9.2 Femtosecond resolved temporal overlap using coherent radiation

After finding the temporal overlap to better than 1 ps resolution by use of the streak camera, the transverse overlap of the NIR laser pulse and electron bunch was performed. The longitudinal electron bunch distribution was, at this point, precisely determined using the TDS experiment, see Fig. 9.5. Applying the two-Gaussian fit model to the measured data, the FWHM duration of the peak is approximated at about 59 fs.

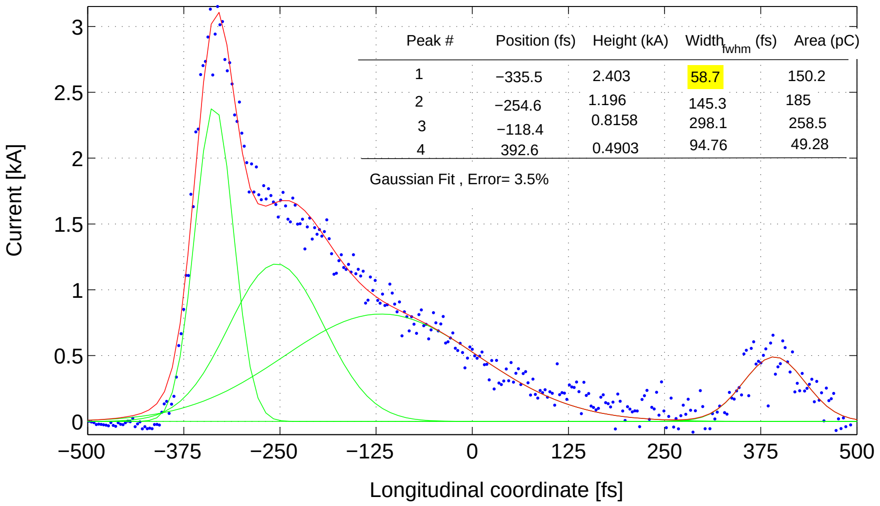

Figure 9.5: *The electron bunch distribution measured with the TDS during the commissioning shift on Oct. 2010.*

At the same time that the temporal overlap is measured with the streak camera after the modulator, an optical transition radiation screen directs out of the beamline the signal of the radiator, which is tuned ito the second harmonic of the modulator. This coherent enhanced undulator emission, which is produced upon temporal overlap of pulses of interest, is sent to a standard CCD camera and a UV-VIS spectrometer at a measurement station located after the radiator. The NIR laser pulse is moved temporally with respect to the electron bunch by using a vector modulator as explained in Chapter 4. The minimum step size of the scan is limited to 45 fs due to the resolution of the 14bit digital-to-analog converter (DAC). The DAC controller drives a voltage to tune the vector modulator, which set the relative phase between the external RF and the NIR laser oscillator RF. The phase-lock-loop drives the oscillator length such, that this phase difference is compensated again and lets the pulse be shifted in time.

After finding the overlap at better than 1 ps resolution, the vector modulator shifts the laser in 50 fs steps with respect to the electron bunch, until the coherent enhancement of the undulator radiation in the CCD camera signal is observable, see Fig. 9.6(b).

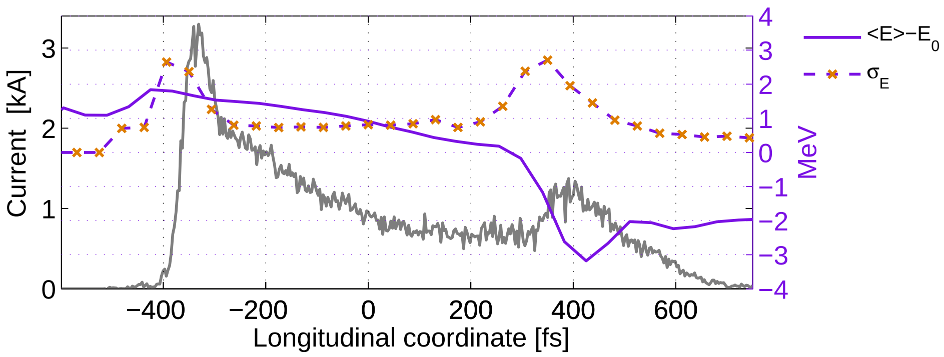

(a) *Measured electron bunch distribution, sliced energy spread and mean energy deviation using TDS setup.*

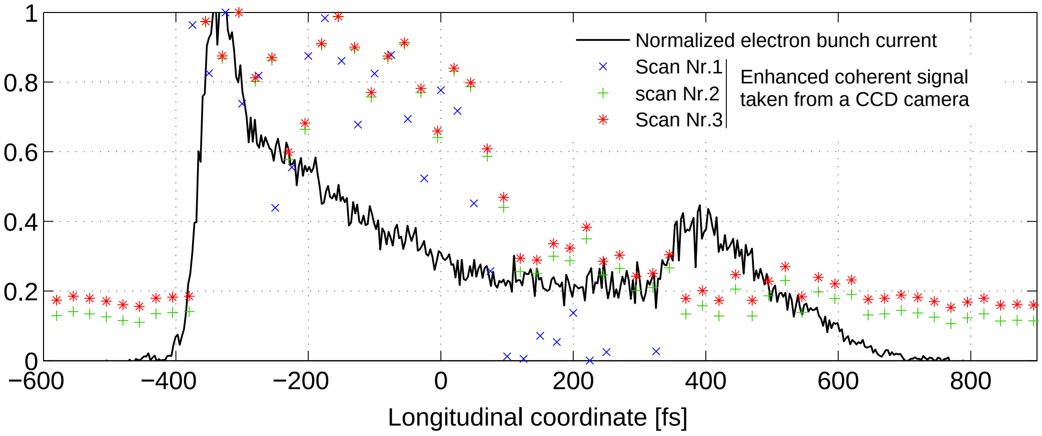

(b) *Enhancement of coherent light measured with a CCD camera after radiator.*

Figure 9.6: *The electron bunch properties and enhanced coherent signal seen by a CCD camera.*

At the position of the peak current, the measured sliced energy spread was $\sigma_E \sim 750\,\mathrm{keV}$ and the mean energy deviation was less than 0.5 MeV, see Fig. 9.6(a). The results of a series of three scans is shown in Fig. 9.6(b). The enhanced signal was sustained over a 200 fs interval along the electron bunch distribution. A two-Gaussian fit model was applied to one series of the measurement to characterize the , see Fig. 9.7.

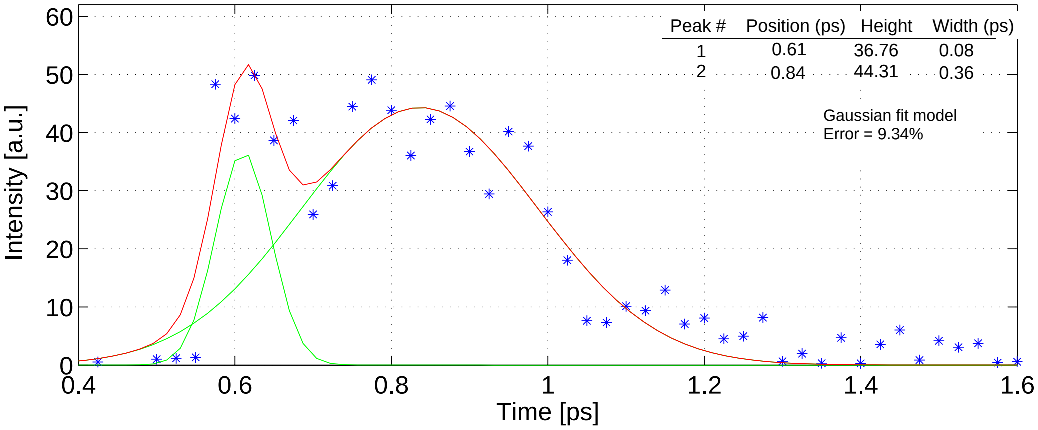

Figure 9.7: *Two Gaussian fit applied on the scan data of the radiator radiation.*

The width of the first peak is about $(80\,\mathrm{fs})_{\mathrm{FWHM}}$. This can be compared with the width of peak of the electron bunch distribution, which is approximately $(60\,\mathrm{fs})_{\mathrm{FWHM}}$. The fact that the measured widths of the electron bunch and the coherent radiation are comparable is not surprising, nor is the fact that they are not identical. The peak in the current naturally favors larger coherent radiation production. The current peaks also may have larger slice emittance energy spreads associated with CSR and space-charge effects, which tend to degrade the coherent emission.

The measurement was reproducible and was used as a standard tool during most of the commissioning shifts. CSR effects are destructive for this measurement. Because of this, for the fine temporal overlap the electron bunch was initially set on-crest. After the measurement of the SASE, and before proceeding with the seeding experiment the electron bunch was set off-crest. The difference in electron bunch arrival-time between on and off crest operation was measured to be approximately 3 ps, which needs to be taken into account, when setting the temporal overlap in the seeding experiment itself.

9.3 Attempts for seeding at 38 nm

Due to a relatively low coupled-energy of the seed pulse with the electron bunch, gain due to seeding in the FEL would not be easily observable. For this reason, numbers of tests were performed to distinguish between the seeded and SASE spectra. Typically 2000 shots were recorded to characterize the SASE signal distribution. The Kolmogorov - Smirnov test was applied to compare the distributions of the two spectra of the interest. In the case of seeding, a change in the recorded spectra in comparison with the SASE was expected. For example a second maximum might show up in a reproducible manner.

Another test was the energy measurement of the SASE radiation within the seed pulse bandwidth. If the measured energy exceeds a certain level, this shot can be counted as a candidate for displaying seeded FEL gain. For more information on this measurement and analysis, readers are addressed to [Böd11].

During the measurement some of the machine parameters (e.g. beam arrival time monitor, beam energy monitor, beam charge monitor) drift notably, causing a systematic error in the statistical measurement. To prevent this effect from corrupting the data set, a filter with range of ($\pm 2.5\sigma$) about nominal parameters was used. In principle the single shot spectra should be recorded at the same time, therefore smaller filter range is favorable but this could not be achieved without dedicating longer times within out limited operating shifts.

9.4 Offline data analysis

During the shift period on Apr. 2011 the scan over 500 fs with step of 50 fs was performed. For each step 500 shots with HHG on and 500 shots with the HHG pulse off were recorded. The result of the first scan is shown in Fig. 9.8. Enhancement due to seeding was not observed.

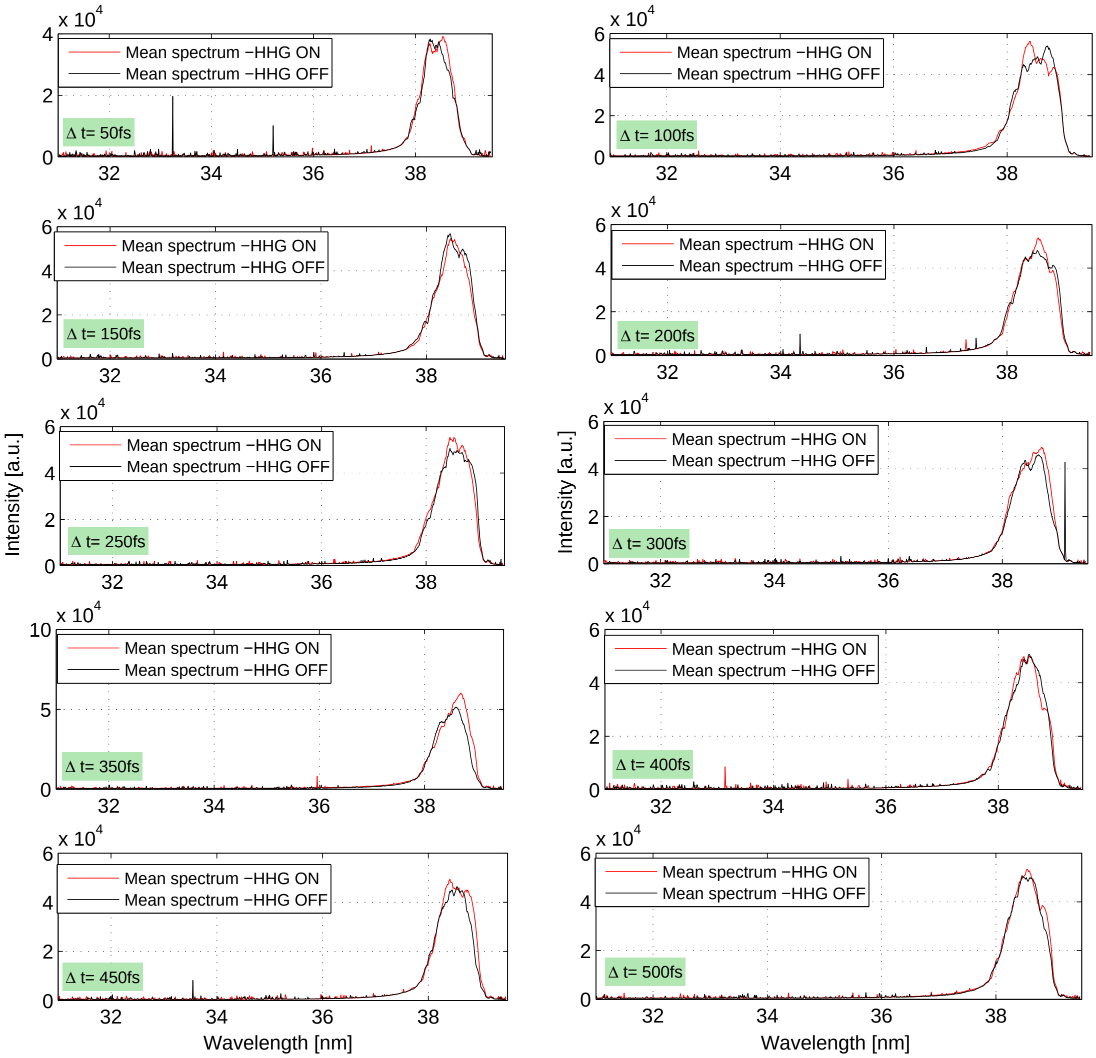

Figure 9.8: *Example of the scan results, (Apr. 2011). The maxima of 500 spectra with HHG seed pulse on and 500 spectra with HHG off were recorded. The scan was performed with step size of 50 fs. Enhancement due to seeding was not observed.*

10 Conclusion and Outlook

The free electron laser in Hamburg (FLASH) is a user facility which produces ultrashort radiation with peak brilliance $\approx 10^{29}$-10^{31} photons/(s mm^2 mrad^2 0.1%BW) and average power $P_{avg} \approx$ 300 mW. However as the undulator radiation starts from shot noise as a consequence the SASE FEL radiation shows random variations and fluctuations in the spectral domain yielding temporal pulses that are not as narrow and precise as certain classes of the experiments would require. The FEL would thus benefit from an external coherent source of radiation to suppress these fluctuations. Among different possible schemes, the use higher-harmonics generated in Ar gas was adopted to provide this source of coherent radiation for the seeding experiment at FLASH. The 21^{st} harmonic of the NIR laser pulse, $\lambda_s = 38$ nm, was used as the seeding wavelength.

During the commissioning shifts the sub-components of the seeding experiment were successfully commissioned, including HHG generation and transport from the source to the extraction beam line, the achieving of SASE from the seeding undulators, the transverse and spectral overlap between the seed pulse and the electron bunch, and the longitudinal overlap between the electron bunch and the NIR laser pulses better than 100 fs.

The electron bunch distribution, and arrival time jitter are the key parameters for the performance of the longitudinal overlap. To quantify these parameters, the longitudinal distribution of the electron bunch was measured by a TDS setup during each of our commissioning shifts. Beam based feedback was used to reduce the electron bunch jitter. During the shifts the average jitter of the electron bunch relative to the RF was measured about 70 fs.

A series of FEL simulations was performed to study the efficacy of the seeding mechanism with low coupled seed energy (10 pJ). The electron bunch distribution used for the simulation was taken from the measurement with a temporal extent $(\approx 400\,\text{fs})_{FWHM}$. The enhanced seeded signal appeared in a point along the electron bunch with the lowest mean energy deviation and relatively small energy spread; In these studies, the enhanced seeded signal was therefore not, as intuition might dictate, seen at the peak of the current distribution. For the temporal offset larger than 66 fs from the optimum overlap point the enhanced seeded signal drops drastically. The results of the simulation put a limitation in the acceptable beam arrival time jitter and electron bunch characteristics.

Statistical studies show that the probability of the optimum overlap between electron bunch ($\sigma_e = 100\,\mathrm{fs}$) and seed pulse ($\sigma_s = 10\,\mathrm{fs}$) is approximately 20% for the relative rms jitter of about $\sigma_j = 122\,\mathrm{fs}$. For a more accurate estimation one should consider also the effects of transverse jitter and electron bunch energy fluctuations. For numerical simulations approximately 50 evaluations seems to be a reasonable choice, to give a statistical analysis of the temporal jitter effects, but inclusion of two other fluctuating parameters would demand a much more time intensive analysis.

To directly address the issue of temporal synchronization in the experiment two methods have been proposed to measure the temporal overlap between the two pulses of interest. Firstly the photomultiplier was used to find the relative timing of the pulses within 1 ns. Afterwards, the streak-camera based measurement was used to measure the relative timing between two pulses with sub-picoseconds resolution ($\approx 650\,\mathrm{fs}$).

The synchrotron radiation emitted from a 1 m long undulator (upstream seeding undulator), along with the NIR laser pulse were used as references for the arrival time measurement of the electron bunch and seed pulse, respectively. The experimental setup was installed in the tunnel. To protect the streak-camera against gamma and neutron radiation 20 mm thick lead plates with 15 mm borated polyethylene were used. During almost 2 years operation of the streak-camera in the tunnel no damage or loss of functionality were observed in the photo-detectors. The beam line and streak-camera were operated remotely during all shifts.

The tolerance studies also revealed that the path difference between the NIR laser and the synchrotron radiation of the modulator from the source to the point of measurement is far below the resolution of the measurement. The path difference between seed radiation and NIR laser pulse is also orders of magnitude less than resolution of the measurement devices.

A modulator-radiator (MOR) scheme was proposed as a reliable and precise tool for the synchronization between two femtosecond pulses with resolution about 50 fs. The ORS experiment at FLASH which was initially proposed as a tool for the longitudinal bunch length measurement thus showed promising potential for the synchronization purposes.

Analytical studies and experimental results obtained from this coherent radiation-based method are in a good agreement. The enhancement of the coherent signals at the time of overlap between the NIR laser and the electron bunch was observed. The measurement results were reproducible.

With temporal (as well as transverse and spectral) overlap achieved, it was hoped measure significant amplification of a seed signal in the FEL. To observe the seeding signal at 38 nm from seeding undulator several time delay scans were performed. The on-line analysis of the sFLASH SASE spectrum did not show the any clear evidence for the seeding at 38 nm. The post analysis of the data showed the presence of the second peak at the seeding wavelength for one step of the time delay scan. The measured peak was not reproducible, a result that can be correlated to the fluctuations in the machine parameters.

Simulation results using GENESIS show that the relatively low coupled seed pulse energy is on the same order of the shot noise level. In Fig. 10.1 the expected spectral and power contrasts for different seed pulse energies are shown.

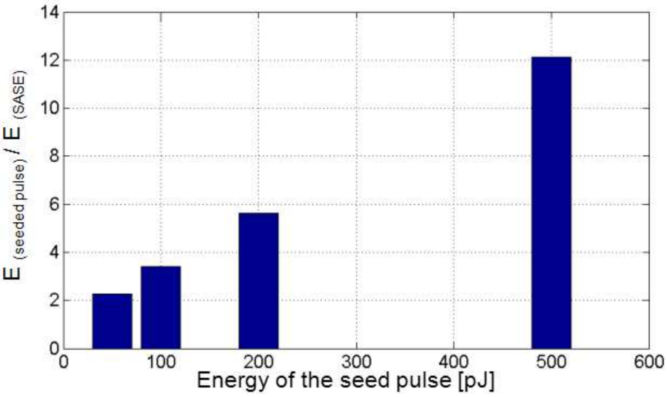

(a)

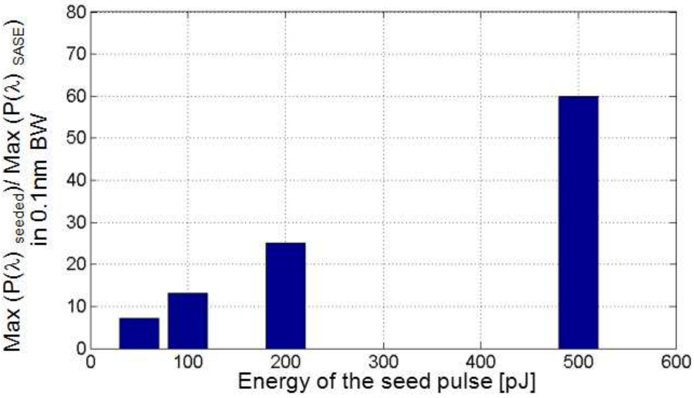

(b)

Figure 10.1: *The contrasts between seeded signal and the SASE background for different seed pulse energies. a) The energy contrast. b) The spectral contrast in 0.1nm bandwidth.*

Several improvements are foreseen for the seeding experiment in the future. To measure the actual seed pulse energy an XUV photo diode is installed in the undulator section. To control the focus position of the seed pulse within undulator, a focusing mirror with variable focal length will be installed at the injection beam line.

Another approach to improve the synchronization of the NIR laser pulse to the electron bunch is to apply an optical synchronization scheme instead of the RF-based timing distribution through coaxial cables. The latter case suffers from both thermal and mechanical noise-induced jitters. In contrast, the optical fiber-based system can be active path-length stabilized.

Due to delay inherent in the feedback system a couple of bunches in the train is required to reduce the jitter. According to the arrival time jitter measurement, shown in Fig. 3.4, the latency of the feedback system is about $10\,\mu$s, therefore to have the lowest possible jitter one would need to use the bunch number $\geq$ 10.

We also note that the minimum step size was limited to 47 fs due to the resolution of the vector modulator and 14bit digital-to-analog converter (DAC). This system could be easily improved to give higher tuning resolution of the synchronization system. Currently 1.3 GHz is used as a reference feedback frequency from the master oscillator. However, there is the possibility of using 9.1 GHz harmonic giving a field slope which is 7 times larger than for 1.3 GHz. Thus the feedback loop may measure and correct for the seven times smaller temporal errors. In order to scan in finer steps, an optical delay line with sub 3 fs resolution can be used in addition.

Further upcoming upgrades are foreseen for the FLASH facility. Among them are the installation of new undulator beam line (FLASH-II) after the existing accelerating modules [FBA^{+}11]. A seeding scheme based on a quasi-phase matching approach is foreseen for the new FEL beamline. The same strategies as we have introduced in this thesis work that were employed for finding the temporal overlap between seed pulse and the electron bunch are also foreseen for the FLASH-II. For more information reader is addressed to Ref. [WYD^{+}11].

Appendices

A Convolution of two Gaussian distributions

As the simplest model, a Gaussian distribution is assumed for the longitudinal profiles of the electron bunch $f_e(t)$ and seed pulse $f_s(t)$, see Fig. A.1. The seed profile given by green-dashed lines. The convolution (overlap) function of seed pulse and electron bunch is plotted in orange-circles in the same figure.

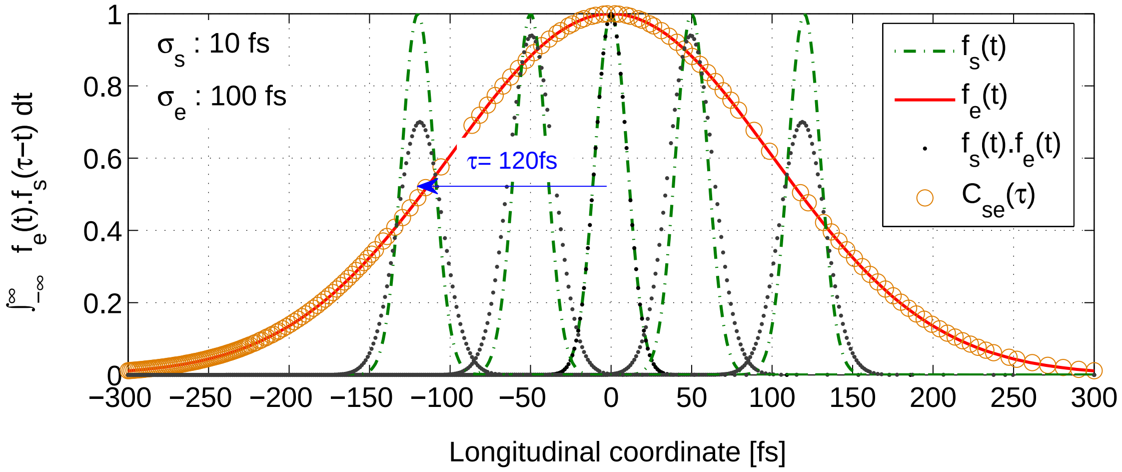

Figure A.1: *The convolution of electron bunch and seed pulse distribution. A Gaussian distribution is assumed for the longitudinal profile of the seed pulse $f_s(t)$ and electron bunch $f_e(t)$. The rms electron bunch and seed pulse duration are assumed to be σ_e =100fs and σ_s =10fs, respectively. The convolution (overlap) function is defined as the area under the product of two functions at time t, ($\int_{-\infty}^{\infty} f_e(t)\times f_s(\tau - t)\,dt$). As an example, the seed pulse is plotted in different longitudinal position relative to the electron bunch. For $\tau \geq$120fs the overlap drops down to less than 0.5 of a perfect overlap.*

As an example, some different relative positions between the seed pulse and the electron bunch are plotted. For the case with zero temporal offset between seed pulse and electron bunch ($\tau = 0$) the convolution function is equal to one and that shows the case with perfect overlap. Here the optimum overlap can be defined as the $C_{s,e}(\tau) \geq 0.9$, where two pulses are separated less than 50 fs from each other. The convolution function for different electron bunch duration is plotted in Fig. A.2. The probability of having an optimum overlap would increase for the longer electron bunch duration. One of the most challenging steps in the experiment is tuning the electron bunch with low energy spread and high peak current with long enough duration.

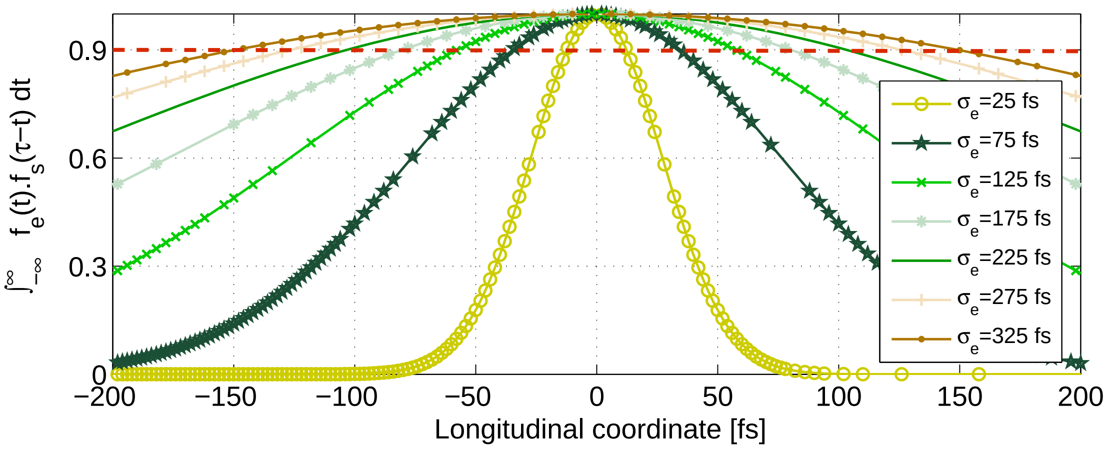

Figure A.2: *The convolution of electron bunch and seed pulse distribution for different electron bunch duration. The rms seed pulse duration is $\sigma_s = 10$ fs. The optimum overlap is defined for the convolution functions ≥ 0.9.*

B Optimization of the dispersion strength

There is a possibility to control the dispersion strength of the vertical chicane, which is downstream of the modulator section, by varying the dipole magnet current up to 2.5 kA, thus providing a tuning method and therefore the micro-bunching amplitude. Eq. B.1 shows the formula for the R_{56} of the chicane which consists of 4 magnets:

$$R_{56} = 2 \cdot a \cdot \theta^2 \tag{B.1}$$

Here a=850 mm is the distance between first two magnets in the chicane and θ is the deviation angle of the beam from the nominal axis which can be derived from Eq. B.2:

$$\theta = 0.586 \cdot \frac{5L \cdot B}{\gamma} \tag{B.2}$$

The field integral through the chicane for different magnet's current can be found in Ref. [TCA02]. The angle for the magnet current of 2.5 kA at distance of 1 m for the beam energy of E_e =700 MeV is approximately 9.5 mrad. The maximum dispersion strength related to this angle is about R_{56} =153 μm.

C Possibility of even harmonic coupling in the existing setup

The resonant condition can be also fulfilled when the laser frequency is a multiple of the undulator frequency. Due to a big K value the spectrum of the modulator in the ORS setup has peaks in many higher harmonics of the fundamental frequency. In the quantum approach due to these higher harmonics, absorption of radiation (IFEL) is also possible. As it was described in the literature, [MPR05], the coupling coefficient, Eq. C.1, for the n^{th} harmonic can be derived from the electron equation of motion in the combined field of laser and undulators magnetic field. The coupling coefficients for the n^{th} harmonic are given by:

$$JJ_n = \sum_{m=-\infty}^{+\infty} J_m(G)[J_{2m+n+1}(\xi) + J_{2m+n-1}(\xi)] \tag{C.1}$$

where $G = \frac{\lambda_u K^2}{8\lambda\gamma^2}$ and $\xi = \frac{\lambda_u K\theta}{\gamma\lambda}$. Here K is the undulator parameter, λ_u is the undulator period length, λ is the wavelength of the radiation and θ is the horizontal angle between the electron beam and the laser propagation direction. The resonant energies are a function of this crossing angle, as it is shown in Eq. C.2:

$$\theta = \sqrt{\frac{2n\lambda}{\lambda_u} - \frac{(1+K^2/2)}{\gamma^2}} \tag{C.2}$$

For the second harmonic interaction (n=2) this crossing angle is $\theta = 3.6mrad$. For the ORS setup, the electron bunch with energy of $700\,MeV$, interacts with the laser field inside an undulator with undulator parameter $K = 6.84$ and period $\lambda_u = 200\,mm$. In this case the resonant wavelength of the undulator is equal to $\lambda = 1300\,nm$, $G = 0.47$, $\xi = 2.8$. Using Eq. C.1 for the second harmonic, we will have:

$$JJ_2 = \sum_{m=-\infty}^{+\infty} J_m(G)[J_{2m+3}(\xi) + J_{2m+1}(\xi)] \tag{C.3}$$

that gives the coupling coefficient $JJ_2 = 0.68$, which is comparable with the bunching coefficient at fundamental harmonic $JJ_1 = 0.94$.

The advantage of considering this method is to have different color for the synchrotron light of the undulator and laser beam, which should be used for the synchronization. As it will be discussed in the next chapters, due to the power threshold of the photo-detectors, both beams should be attenuated with combination of some spectral filters in the same beam line. Due to the large K value of the ORS undulator significant energy exchange can happen via high harmonic IFEL interaction.

D Transmission of the seeding beamline for the NIR laser beam

The transmission of the seeding beamline for different initial polarization of the NIR laser beam is shown in Fig. D.1.

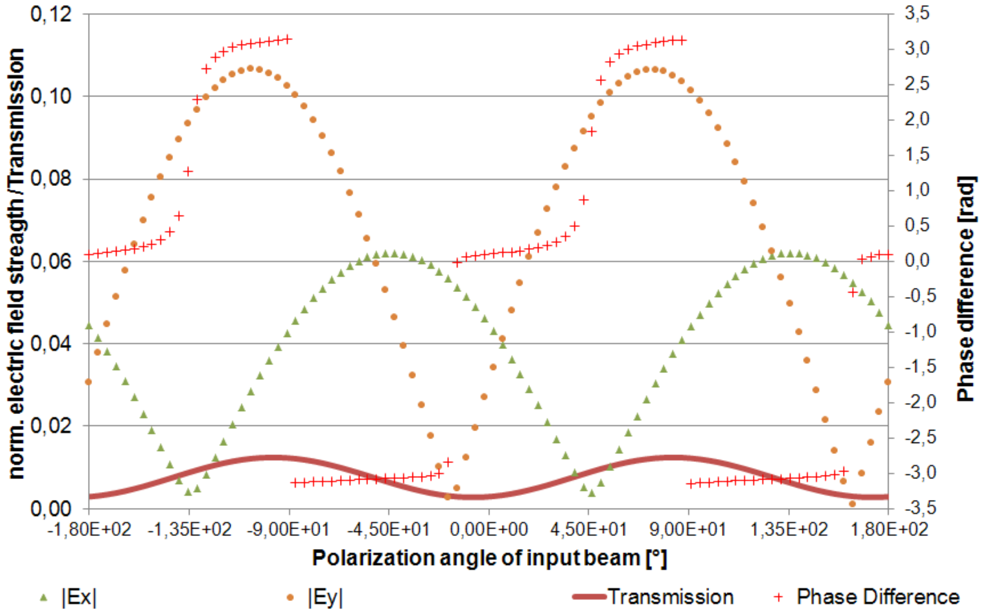

Figure D.1: *Transmission of the seeding injection beamline for the NIR laser beam. Here*E_x *and* E_y *are the electric field components parallel and perpendicular to the deflection plane of the seeding undulator relative to the field at the beginning of the beam line [Böd12].*

The electric field components parallel and perpendicular to the deflection plane of the seeding undulator relative to the field at the beginning of the beam line are shown with E_x and E_y, respectively. For a beam with nearly zero polarization angle at the source the transmission of the beam line is approximately $((\frac{E_T}{E_0})^2 = 2.85 \times 10^{-3})$. E_0 is the electric field at the source and E_T is the transmitted total electric field at the point of interest. According to the same figure, at zero polarization angle the vertical component of the field is $\frac{E_y}{E_0} = 0.027$. This together with the total estimated transmission $(\frac{E_0}{E_T} = 20)$

show that 54% of the total NIR laser field is perpendicular to the plane of the undulator $E_y = 0.54\,E_T$. The polarization angle between the total field and the horizontal plane in this case is approximately $\theta = 33\,^\circ$.

E Neutron and gamma dosimetry

To estimate the amount of ionizing radiation pairs of TLD600 and TLD700 were used in different part of the streak-camera container for two weeks FLASH operation. The TLD600 chip is made of 6-Lithium Floride (6Lif) and is sensitive to gamma, betas and neutrons. TLD700 chip is made of another Lithium isotope (7Lif) which is sensitive just to beta and gamma radiation. The crystal of mentioned TLDs give off light when they are heated. The emitted light being proportional to the degree of exposure by the TLDs. The curves obtained from the heating process are plotted in Fig. E.1. The area under the TLD700 first peak represents the gamma radiation energy and the area under second peak of the TLD600 gives the neutron flux stored on the TLDs.

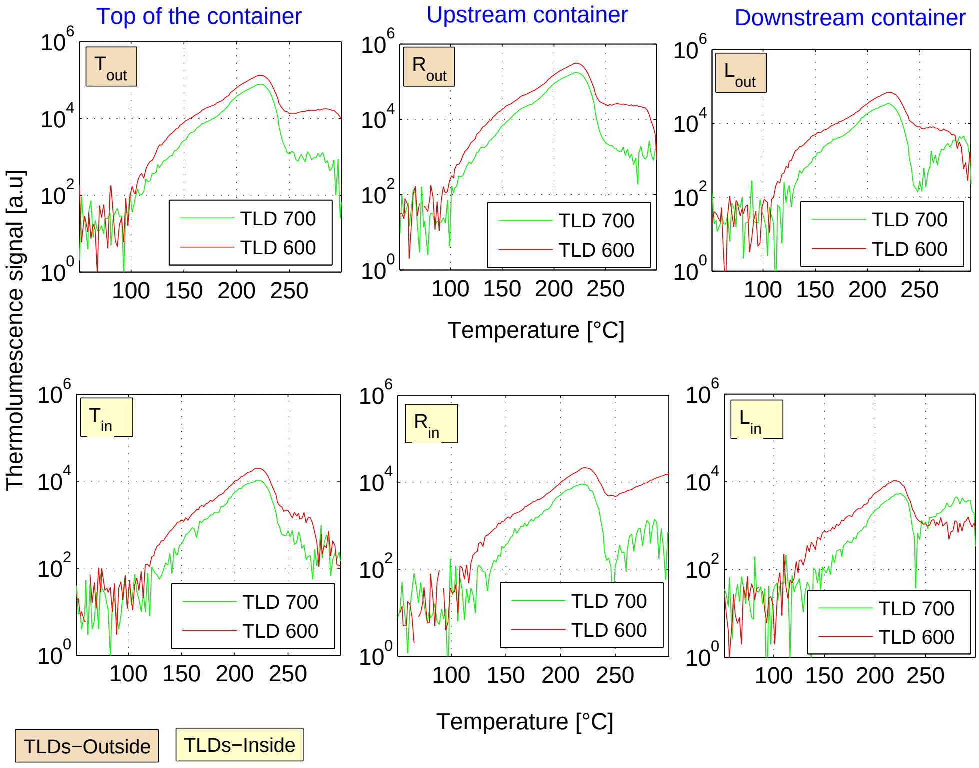

Figure E.1: *Thermoluminescence signal of TLD-600 and TLD-700 in different location around the shielding container*

F Transient time of the optical wavelengths through different materials

The transient times of various wavelength from 200 nm to 800 nm are calculated for different thickness of the optical elements used in the longitudinal-overlap beamline. The dispersion due to the glass window (between vacuum and air), air and the spectral filters which are made of fused silica is plotted in Fig. F.1.

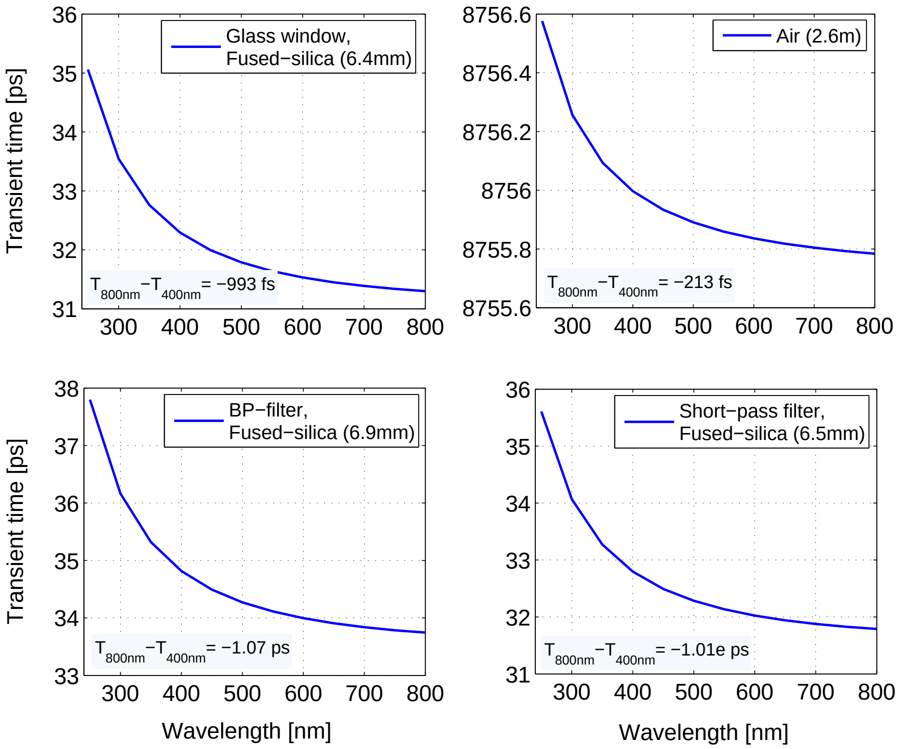

Figure F.1: *Transient time of visible wavelengths through different material used in the beamline.*

The dispersion due to input optic of the streak camera (CaF_2 and SiO_2 materials) and the external lens of the beamline is plotted in Fig. F.2. An an example the total dispersion through all materials in the beamline between 400 nm and 800 nm wavelengths is about 7.3 ps. The biggest effect is due to the input optic of the streak camera, which is 24 mm thick and is made of CaF_2 material.

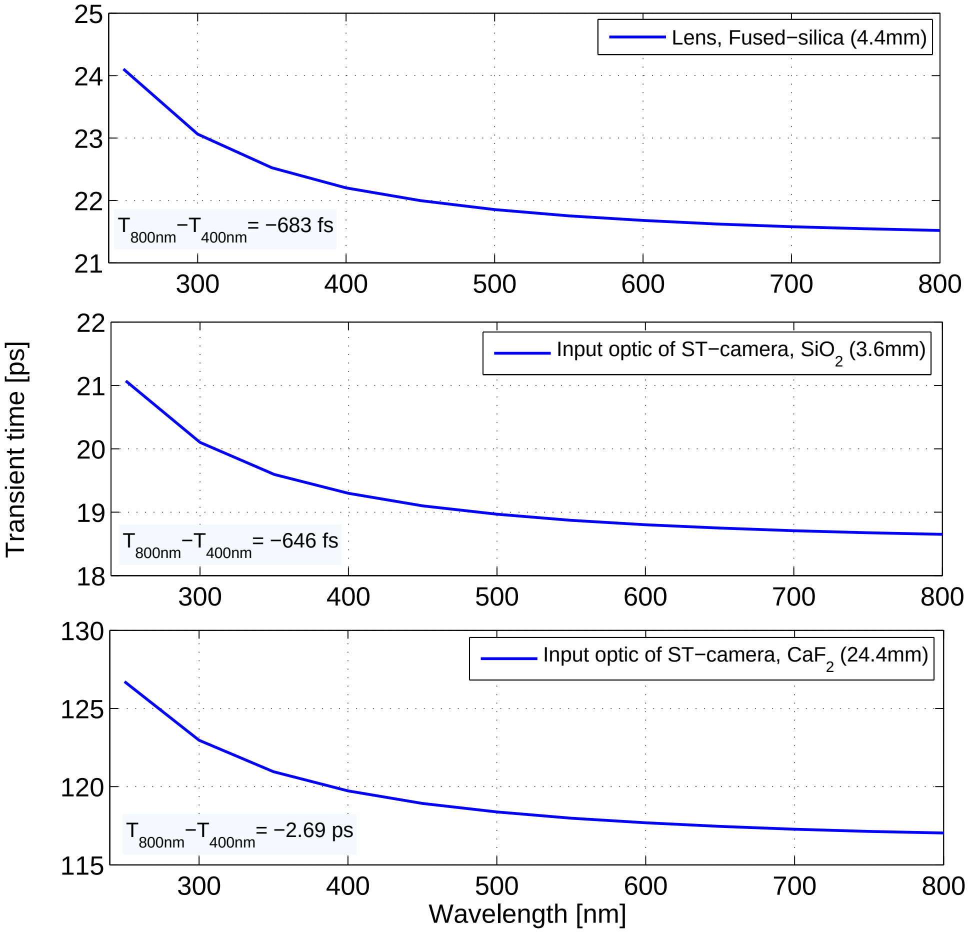

Figure F.2: *Transient time of visible wavelengths through lenses.*

Bibliography

[AAB+11] S. Ackermann, A. Azima, J. Bödewadt, et al. sflash- present status and commissioning results. In *Proceedings of IPAC2011*, 2011.

[All04] T. Allison. High harmonic generation. Technical report, UC Berkeley, 2004.

[ANF10] E. Allaria, GD. Ninno, and WM. Fawley. The second stage of fermi@elettra: A seeded fel in the soft x-ray range. Technical report, Lawrence Berkeley National Laboratory, Paper LBNL-2536E, 2010. Retrieved from: http://escholarship.org/uc/item/3mv3w94v.

[AZM+08] G. Angelova, V. Ziemann, A. Meseck, P. Salén, P. van der Meulen, M. Hamberg, M. Larsson, J. Bödewadt, S. Khan, A. Winter, H. Schlarb, F. Löhl, E. Saldin, E. Schneidmiller, and M. Yurkov. Observation of two-dimensional longitudinal-transverse correlations in an electron beam by laser-electron interactions. *Phys. Rev. ST Accel. Beams*, 11:070702, Jul 2008.

[B+10] J. Bödewadt et al. sflash - first results of direct seeding at flash. In *FEL 2010*, 2010.

[Bas11] Basler camera, a311f. Website, 2011. Available online at `http://www.baslerweb.com`; visited on 10-Nov-2011.

[Böd11] J. Bödewadt. *Transverse beam diagnostics for the XUV seeding experiment at FLASH.* PhD thesis, Hamburg University, 2011.

[Böd12] J. Bödewadt. Unpublished, private communication. 2012.

[BFG+10] M. K. Bock, M. Felber, P. Gessler, K. E. Hacker, F. Ludwig, H. Schlarb, B. Schmidt, J. Zemella, S. Schulz, and L.-G. Wissmann. Recent development of the bunch arrival time monitor with femtosecond resolution at flash. In *Proceeding of IPAC 10*, 2010.

[Bg11] C. Behrens and C. gerth. Measurement of the slice energy spread induced by a transverse deflecting rf structure at flash. 2011.

[BLT+98] M. Bellini, C. Lynga, A. Tozzi, M. B. Gaarde, T. W. Hänsch, A. L'Huillier, and C.-G. Wahlström. Temporal coherence of ultrashort high-order harmonic pulses. *Phys. Rev. Lett.*, 81:297–300, Jul 1998.

[Boa83] M.L. Boas. *Mathematical Methods in the Physical Sciences.* John Wiley and Sons Ltd., 1983.

[Bp-11] Borated polyethylene plates, san diego plastics, inc. website, 2011. Available online at `http://www.sdplastics.com/`; visited on 1-Nov-2011.

[BPN84] R. Bonifacio, C. Pellegrini, and L. Narducci. Collective fel parameter. *Opt. Commun*, 50:373, 1984.

[BT66] V. I. Bespalov and V. I. Talanov. The filamentary structure of light beams in nonlinear liquids. *Pis'ma Zh. Eksp. Teor. Fiz.*, 3:471, 1966.

[BZDMK+91] I. Ben-Zvi, L.F. Di Mauro, S. Krinsky, M.G. White, and L.H. Yu. Proposed uv-fel user facility at bnl. *Nuclear Instruments and Methods in Physics Research Section A*, 304:181–186, 1991.

[CAB+09] F. Curbis, A. Azima, J. Bödewadt, H. Delsim-Hashemi, M. Drescher, et al. Photon diagnostic for the seeding experiment at FLASH. In *Proceedings FEL Conference*, Liverpool, 2009.

[CD82] R. Coisson and F. DeMartini. Physics of quantum electronics. *Addison-Wesley, Reading, MA*, 9:939, 1982.

[CE98] O. Chubar and P. Elleaume. Accurate and efficient computation of synchrotron radiation in the near field region. In *Proceeding of the EPAC98 Conference*, 1998.

[Cla04] J.A. Clarke. *The Science and Technology of Undulators and Wigglers.* Oxford science publications, 2004.

[Cor93] P. B. Corkum. Plasma perspective on strong field multiphoton ionization. *Phys. Rev. Lett.*, 71(13):1994–1997, Sep 1993.

[CSS+05] S. Casalbuoni, H. Schlarb, B. Schmidt, B. Steffen, P. Schmüser, and A. Winter. Numerical studies on the electro-optic sampling of relativistic. electron bunches. In *Particle Accelerator Conference, Knoxville, Tennessee*, 2005.

[Cur11] F. Curbis. Private communication, 2011. 2011.

[DEM$^+$77] D. A. G. Deacon, L. R. Elias, J. M. J. Madey, G. J. Ramian, H. A. Schwettman, and T. I. Smith. First operation of a free-electron laser. *Phys. Rev. Lett.*, 38:892–894, Apr 1977.

[Den09] U. Denzer. Unpublished, private communication, 2009.

[DG511] Delay generator dg535. website, 2011. Available online at `http://www.thinksrs.com/products/DG535.htm`; visited on 1-Sep-2011.

[DHMR$^+$09] H. Delsim-Hashemi, V. Miltchev, R. Roßbach, M. Tischer, et al. Status of the sFLASH undulator system. In *Proceedings FEL Conference*, Liverpool, 2009.

[DRB$^+$99] Charles G. Durfee, Andy R. Rundquist, Sterling Backus, Catherine Herne, Margaret M. Murnane, and Henry C. Kapteyn. Phase matching of high-order harmonics in hollow waveguides. *Phys. Rev. Lett.*, 83:2187–2190, Sep 1999.

[edm11a] Compound parabolic concentrator (cpc). website, 2011. Available online at `http://www.edmundoptics.com/`; visited on 1-Aug-2011.

[edm11b] Short-pass filters, 2011. Available online at `http://www.edmundoptics.com/`; visited on 1-Aug-2011.

[FBA$^+$11] B Faatz, N. Baboi, V. Ayvazyan, et al. Flash-ii: perspectives and challenges. *Nuclear instruments and methods in physics research section A*, 635, 2011.

[FLA07] Flash catalogue. Technical report, Deutsches Elektronen-Synchrotron DESY, 2007.

[FLA11] *TTFLogbuch.* http://ttfinfo.desy.de/TTFelog/index.jsp, 2011.

[FLL$^+$88] M. Ferray, A. L'Huillier, XF. Li, LA. Lompre, G. Mainfray, and C. Manus. Multiple-harmonic conversion of 1064 nm radiation in rare gases. *J. Phys. B: At. Mol. Opt. Phys.*, 21:L31, 1988.

[FSS$^+$97] J. Feldhaus, EL. Saldin, JR. Schneidera, EA. Schneidmillerb, and MV. Yurkovc. Possible application of x-ray optical elements for reducing the spectral bandwidth of an x-ray sase fel. *Optics Communications*, 140:341, 1997.

[ftEt10] S. Weathersby for the ECHO-7 team. Commissioning the echo-seeding experiment echo-7 at nlcta. SLAC reports, 2010.

[GBRS08] O. Grimm, C. Behrens, J. Rossbach, and B. Schmidt. Longitudinal beam diagnostics application of synchrotron radiation at flash. In *Christopher Behrens, J¨org Rossbach (University of Hamburg) Bernhard Schmidt (DESY, Hamburg)*, 2008.

[Gia] L. Giannessi. Suite of mathcad functions for the numerical solution of problems related to free electron laser physics. Reference avialable at www.perseo.enea.it.

[GPDC10] L. Giannessi, A. Petralia, G. Dattoli, and F. Ciocci. Sparc operation in seeded and chirped mode. In *Proceedings of FEL2010*, 2010.

[GSM05] L. Giannessi, S. Spampinati, and P. Musumeci. Non linear pulse evolution in seeded and cascaded fels. *J. Appl. Phys.*, 98:04310, 2005.

[Ham10] Hamamatsu. *Streak camera, FESCA200, Hamamatsu*, 2010.

[Ham11a] Dealy unit, c6878, hamamatsu, 2011.

[Ham11b] Photomultiplier tube, h6780-20 pmt, hamamatsu, 2011.

[HMI] *Delay generator*. Courtesy by Janata, E., HMI Berlin (Now HZB), Schreiber, S., DESY.

[HMS$^+$09] Xinkui He, M. Miranda, J. Schwenke, O. Guilbaud, T. Ruchon, C. Heyl, E. Georgadiou, R. Rakowski, A. Persson, M. B. Gaarde, and A. L'Huillier. Spatial and spectral properties of the high-order harmonic emission in argon for seeding applications. *Phys. Rev. A*, 79:063829, Jun 2009.

[HSL07] KE. Hacker, H. Schlarb, and F. Löhl. Large horizontal aperture bpm for use in dispersive sections of magnetic chicanes. In *Proc. of EPAC*, 2007.

[J3S11] J3/j4/j3s series pyroelectric/silicon joule meter. website, 2011.

[Jac99] J.D. Jackson. *Classical Electrodynamics*. John Wiley and Sons (WIE), 1999.

[Kim86] Kwang-Je Kim. Three-dimensional analysis of coherent amplification and self-amplified spontaneous emission in free-electron lasers. *Phys. Rev. Lett.*, 57:1871–1874, Oct 1986.

[LAF+08] F. Löhl, V. Arsov, K. Felber, K. Hacker, B. Lorbeer, F. Ludwig, K. Matthiesen, H. Schlarb, B. Schmidt, A. Winter, S. Schulz, J. Zemella, J. Szewinski, and W. Jalmuzna. Measurement and stabilization of the bunch arrival time at flash. In *Proceedings of EPAC08*, 2008.

[lin11] Mirro linos. website, 2011. Available online at `http://www.optoscience.com/`; visited on 1-Aug-2011.

[Lyt08] A.L. Lyte. *Harmonic generation in hollow waveguides.* PhD thesis, Universitz of Colorado, 2008.

[MAB+08] V. Miltchev, A. Azima, J. Bödewadt, M. Drescher, H. Delsim-Hashemi, S. Khan, T. Maltezopoulos, M. Mittenzwey, et al. Tolerance studies on the high harmonic laser seeding at FLASH. In *Proceedings FEL Conference*, Gyeongju, 2008.

[MGJ+87] A. McPherson, G. Gibson, H. Jara, U. Johann, T.S. Luk, I. A. McIntyre, K. Boyer, and C. K. Rhodes. Studies of multiphoton production of vacuum-ultraviolet radiation in the rare gases. *J. Opt. Soc. Am. B*, 4:595–601, 1987.

[Mit11] M. Mittenzwey. *High Harmonic Generation for the XUV seeding experiment at FLASH.* PhD thesis, Universität Hamburg, 2011.

[MP90] J.B. Murphy and C. .Pellegrini. *Laser Handbook: Free-Electron Lasers, Vol. 6.* North Holland, 1990.

[MPR05] P. Musumeci, C. Pellegrini, and J. B. Rosenzweig. Higher harmonic inverse free-electron laser interaction. *Phys. Rev. E*, 72:016501, Jul 2005.

[MS08] B. Mukherjee and S. Simrock. Accelerator dosimetry at free electron lasers in hamburg. *Radiation measurement*, 43:1154–1159, 2008.

[Muk11] B. Mukherjee. Unpublished, private communication, 2011. 2011.

[ND-11] Neutral density filter. Website, 2011. Available online at `http://www.cvimellesgriot.com/`; visited on 1-Nov-2011.

[oce11] Usb 4000-vis-nir miniature fiber optic spectrometer, ocean optics,. website, 2011. Available online at `http://www.oceanoptics.com/products/usb4000visnir.asp`; visited on 1-Sep-2011.

[P+88] W.H Press et al. *Numerical recipes in C (The art of scientific computing).* Cambridge university press, 1988.

[Pel02] C. Pellegrini. X-raz free-electron lasers: Principles, properties and applications. Technical report, UCLA and Joachim Stoehr, SSRl 2002, 2002.

[Rei99] S. Reiche. GENESIS 1.3: a fully 3d time-dependent FEL simulation code. *Nuclear Instruments and Methods in Physics Research Section A: Accelerators, Spectrometers, Detectors and Associated Equipment*, 429(1-3):243 – 248, 1999.

[Roe11] Lead paltes, roehr-stolberg gmbh. website, 2011. Available online at `http://www.roehr-stolberg.de/`; visited on 1-Nov-2011.

[Rul05] C. Rulliere, editor. *Femtosecond laser pulses: principles and experiments.* Springer, 2005.

[Sal05] E. A.; Yurkov M. V. Saldin, E. L.; Schneidmiller. A simple method for the determination of the structure of ultrashort relativistic electron bunches. *Nuclear Instruments and Methods in Physics Research Section A*, 539:499–526, 2005.

[SBP$^+$11] C. Schmidt, M. K. Bock, S. Pfeiffer, H. Schlarb, et al. Feedback strategies for bunch arrival time stabilization at flash towards 10 fs. In *Proceedings of FEL11*, 2011.

[SC$^+$05] B. Steffen, S. Casalbuoni, et al. Electron optic bunch length measurement at the vuv-fel at desy. In *Proceedings of PAC05*, 2005.

[Sch10a] S. Schreiber. Lessons from flash. FLS workshop, 2010.

[Sch10b] S. Schreiber. Soft and hard x-ray sase free electron lasers. *Reviews of Accelerator Science and Technology (RAST)*, 3:93–120, 2010.

[Sch11a] Schott bg39 glass data, 2011. Available online at `http://www.optical-filters.com`; visited on 1-Nov-2011.

[Sch11b] S. Schreiber. First lasing in the water window with 4.1 nm at flash,. In *Proceeding of FEL 2011, Shanghai, China*, 2011.

[SDR08] P. Schmüser, M. Dohlus, and J. Rossbach. *Ultraviolet and Soft X-Ray Free-Electron Lasers: Introduction to Physical Principles, Experimental Results, Technological Challenges (Springer Tracts in Modern Physics).* Springer, 2008.

[sFE11] Realizing the potential of seeded fels in the soft x-ray regime, lawrence berkeley national laboratory, 2011, 23011.

[SgK$^+$07] H. Schlarb, C. gerth, W. Koprek, F. Loehl, and E. Vogel. Beam based measurements of rf phase and amplitude stability at flash. In *Proceedings of DIPAC07*, 2007.

[SJ$^+$04] B. Steeg, J. Juha, et al. Total reflection amorphous carbon mirrors for vacuum ultraviolet free electron lasers. *Appl. Phys. Lett.*, 84:657, 2004.

[SM85] D. Strickland and G. Mourou. Compression of amplified chirped optical pulses. *Opt. Commun.*, 56:219, 1985.

[SSS07] E. Saldin, H. Schlarb, and B. Schmidt. Status of the optical replica synthesizer at flash. In *Proceedings of PAC07,*, 2007.

[SSY00] E.L. Saldin, E.A. Schneidmillera, and M.V. Yurkovb. *The physics of free electron lasers.* 2000.

[SSY03] E.L. Saldin, E.A. Schneidmillera, and M.V. Yurkovb. Statistical properties of radiation from sase fel driven by short electron bunches. *Nuclear Instruments and Methods in Physics Research Section A*, 507:101–105, 2003.

[Stu10a] S. Stupakov. Echo-enabled harmonic generation for seeded fels. In *SLAC-PUB-14460*, 2010.

[Stu10b] S. Stupakov. Echo-seeding options for lcls-ii. In *Proceedings of FEL10*, 2010.

[TCA02] Dipole magnet tca-001 certificate, 2b.605499-01 cer,. Technical report, Efremov Institute SAINT-PETERSBURG, 2002, 2002.

[TF$^+$10] T. Togashi, K. Fukami, et al. First observation of the 61.5 nm seeded fel at the scss test accelerator. In *Proceedings of FEL2010*, 2010.

[Tre00] R. Trebino. *Frequency-resolved optical gating.* Kluwer academic publisher, 2000.

[VAB$^+$10] E. Vogel, C. Albrecht, N. Baboi, et al. Test and commissioning of the third harmonic rf system for flash. In *Proceedings of IPAC10*, 2010.

[VM10] Vector modulator, g.t. microwave inc., 2010. Available online at `http:/www.gtmicrowave.com`; visited on 1-Sep-2010.

[WMG$^+$02] I. Wilke, A. M. MacLeod, W. A. Gillespie, G. Berden, G. M. H. Knippels, and A. F. G. van der Meer. Single-shot electron-beam bunch length measurements. *Phys. Rev. Lett.*, 88:124801, Mar 2002.

[WYD+11] A. Willner, M. Yeung, T. Dzelzainis, C. Kamperidis, M. Bakarezos, D. Adams, V. Yakovlev, F. Tavella, and et al. Complete control of high-harmonic generation for high average power applications. In *Quantum Electronics and Laser Science Conference*. Optical Society of America, 2011.

[XFE] Available online at `http:/www.xfel.eu`; visited on 1-Sep-2010.

[YB+00] L.-H. Yu, M. Babzien, et al. First lasing of a high-gain harmonic generation free- electron laser experiment. *Nuclear Instruments and Methods in Physics Research A*, 445:301–306, 2000.

[YMG+00] X. Yan, A. M. MacLeod, W. A. Gillespie, et al. Subpicosecond electro-optic measurement of relativistic electron pulses. *Physical Review Letters,*, 85:3404–3407, 2000.

[Zag09] I. Zagorodonov. Satrt-to-end simulations at flash. Technical report, DESY, 2009. Available online at `http://www.desy.de/xfel-beam/`.

[zem11] *ZEMAX: Software for Optical System Design.* http://www.zemax.com, version feb. 14, 2011 edition, 2011.

[ZL+08] X. Zhang, A. Lytle, et al. Quantum-path control in high-order harmonic generation at high photon energies. *New Journal of Physics*, 10:025021, 2008.

Acknowledgements

I would like to express my sincere gratitude and appreciation to my family, for the knowledge, love and support they have given to me so that I might pursue a successful graduate career. I would like to thank also my brother Farshad who has been my best friend my entire life. I am particularly grateful to my supervisor Joerg Rossbach for all that I have learned from him, for being so supportive, courageous and positive, for having such a deep trust in each of his students. It's not only been a pleasure knowing you through Bernhard Holzer - it's been a privilege! I am also deeply grateful to my other supervisor, Markus Drescher for all of his advice and encouragement. My special thanks also go to Siegfried Schreiber who has supported me throughout my work and my thesis with his patience and knowledge. He is someone you instantly like upon meeting him, and then appreciate him more later. I appreciate the efforts of my sFLASH colleagues for their assistance during construction work and all the commissioning shifts. The work presented in this thesis would not have been possible without the support of different groups in DESY laboratory in Hamburg including ZM1, ZM2 and FLASH operating crew. I would like to thank Otto Peters and Josef Gonschior for their efforts and their enthusiasm in work. I also appreciate the help of Sven Reiche, Igor Zagorodnov, and Velizar Miltchev and Luca Giannessi in my simulation studies presented in Chapter 5. My sincere gratitude also goes to Evgeny Saldin for so many stimulating discussions concerning chapter 6 of my thesis. I am grateful to Bhaskar Mukherjee, Masoumeh Salmani and other colleagues in the radiation safety department of DESY for their unlimited assistance within my work presented in chapter 7. I am also grateful to the following colleagues whose suggestions and encouragement were invaluable throughout my graduate career: Armin Azima, Joern Boedewadt, Hossein Delsim-Hashemi, Oliver Grimm, Katja Honkavaara, Rasmus Ischebeck (from PSI), Theophilos Maltezopoulos, Manuel Mittenzwey, Benjamin Polzin, Juliane Roensch, and Arik Willner. I would like to thank James Rosenzweig from UCLA for so many insightful discussions about my work and for correcting my thesis. I will forever be thankful to my former research advisor, Morteza Aslaninejad. He has been helpful in providing advice many times during my education. I still think fondly of my time as an undergraduate student in his classes. His enthusiasm and love for teaching is contagious. Last but not least I would like also to appreciate my generous friend Marco Argento for being available, supportive and courageous all the time. I am grateful also to my other friends (too many to list here but you know who you are!) for providing the support and friendship that I needed. I would like also to appreciate the help of Hossein and his kind family for facilitating my stay in Hamburg upon my arrival. I convey my thanks to the graduate colleague 1355 for providing the financial means and educational facilities to make this thesis work a reality. Vielen Dank!